Nanostructuring of surfaces for optical and visual security applications using lithography techniques

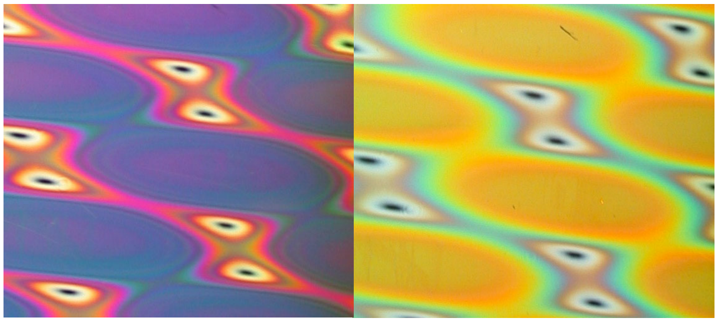

Thèse

Présentée à la faculté des sciences, institut de microtechnique,
pour obtenir le grade de docteur ès sciences par

Christophe Weiteneder

Acceptée sur proposition du jury :

Prof. Dr. HERZIG Hans-Peter, directeur de thèse
Dr. GOMBERT Andreas, rapporteur
Prof. Dr. GOBRECHT Jens, rapporteur
Dr. TOMPKIN Wayne, rapporteur
Dr. VALLAT-SAUVAIN Evelyne, rapporteur
Dr. SCHARF Toralf, rapporteur

Thèse soutenue le 3 Mai 2006

Université
de Neuchâtel

FACULTE DES SCIENCES
Secrétariat-Décanat de la faculté
- Rue Emile-Argand 11
- CP 158
- CH-2009 Neuchâtel

IMPRIMATUR POUR LA THESE

Nanostructuring of surfaces for optical and visual security applications using lithography techniques

Christophe WEITENEDER

UNIVERSITE DE NEUCHATEL

FACULTE DES SCIENCES

La Faculté des sciences de l'Université de Neuchâtel,
sur le rapport des membres du jury

Mme E. Vallat-Sauvain,
MM. H.P. Herzig (directeur de thèse), T. Scharf,
J. Gobrecht (PSI, Villigen), W. Tompkin (OVD, Zug)
et A. Gombert (Freiburg D)

autorise l'impression de la présente thèse.

Neuchâtel, le 15 mai 2006

Le doyen :
J.-P. Derendinger

UNIVERSITE DE NEUCHATEL
FACULTE DES SCIENCES
Secrétariat-décanat de la faculté
Rue Emile-Argand 11 - CP 158
CH-2009 Neuchâtel

ABSTRACT

Nowadays, the use of micro- or nano-patterned surfaces is well established in wide fields of science and in numerous applications in the industry. Periodic surface-relief profiles with dimensions in the wavelength range of the light can act as diffractive optical elements but moreover, the regular pattern can also modify physical properties of a material's surface.

In this dissertation, we focus on the patterning of surfaces by lithography techniques. The useful structured areas are several square centimeters (4-100cm^2) large and the dimensions of the Λ-periodic surface-relief structures are in the range of hundreds of nanometers to micrometers (Λ= 160nm - 10μm).

We present different lithographic methods, in particular interference lithography, to originate the structures in photoresist. We introduce novel setups for multiple beam interference, interference in dense media and sequentially exposures with controlled phaseshift.

A way to realize arbitrarily profiles is to use the Fourier Synthesis (FS). The desired profile is decomposed in a series of sinusoidal functions having a determined amplitude, phase and harmonic number, which is an integer number of the base period of the desired structure. The sum of these sinusoidal functions, aka Fourier components, gives an approximation of the desired profile. Thus, the more components are added, the better becomes the approximation.

But what happens when the harmonic number is not exactly an integer? Through the dissertation, we cover all the aspects, theoretical as well as practical, of the FS. We present a setup that allows to expose sequentially Fourier components and demonstrate the potential of the FS technology by three examples. These consist in saw-tooth profiles, micro-prisms and a fan-out function profile. The profiles were realized with ten Fourier components with structure's period between 1.8μm and 4.7μm.

We investigate also one- as well as two- dimensionally profiles for Optically Variable Devices (OVDs) for visual security against counterfeiting, which exhibit interesting color and polarization properties. Part of them was realized by using the moiré phenomenon.

TABLE OF CONTENTS

CHAPTER 1

INTRODUCTION

The purpose of nanostructured surfaces in broad domains of science has attracted more and more the interest of researchers as well as of the industry. Indeed, they can fulfill many different functions. When they are used as optical nanostructures, they can find their application, for instance, as optical anti-reflection coatings to suppress back reflection from displays, trap for light in photodetectors and solar cells [Cathro 1981, 1984] or simply to direct light into a desired direction. In non-optical applications, nanostructures can modify the physical properties of a material's surface such as wetability or friction coefficient. Furthermore, the nanostructures can facilitate self-assembly or self-alignment of nanoscale elements such as, liquid crystal molecules [Yu 2004]. The advantage of nanostructures (i.e. structures that are in relief) lays in the ease of replication by cost-effective mass-production, such as hot- and roll-embossing [Gale 1997], or injection- and reactive-molding [Isotalo 2004].

Structuring a photosensitive material can be realized through a variety of manufacturing methods. In this thesis, we used interference lithography and standard chromium mask-lithography, a technology widely used in the semi-conductor industry. The main emphasis has been put on interference lithography, because it is a very effective and flexible technology. Surfaces can be structured with high spatial resolution over extremely large field sizes of up to $1m^2$. The principle is to use the interferences of laser light to produce an interferogram which illuminates a light-sensitive polymer like resist. Subsequently, the resist undergo a development that results into a surface-relief structure.

This thesis is divided into 8 chapters which investigate the fabrication and origination of structures in resist.

Chapter 2 gives an overview of the optical lithographic technologies used in this work. In particular, we introduce the theoretical background of the Fourier Synthesis (FS). This technology is based on the sequential superposition of exposures with sinusoidal intensity distribution obtained by two beam interferences. The profile of the resulting structure is the Fourier series of the desired profile. Therefore, profile forms with arbitrarily shapes can be synthesized. We investigate also the moiré phenomenon applied to the fabrication of one- and two-dimensional nanostructures.

Chapter 3 describes the setups used to steer the light beams involved in the recording of the different interferograms. We introduce a novel setup based on a Loyd’s mirror geometry capable to control the phaseshift between two sinusoidal intensity patterns, which have different spatial periods. Indeed, the setup allows exposing sequentially the different Fourier components of a desired Fourier series. With that setup, we were able to produce arbitrarily profiles according to the principle of the FS technology, see chapter 2. We realized profiles with 10 Fourier components and therefore 10 spatially synchronized exposures. A setup based on a right-angled prism that let the interferences occur in dense media is also presented. The aim of that setup is to reduce the spatial period of the structures.

Chapter 4 gives an outline of the resist as recording material. We briefly describe the mechanisms occurring in the chemistry of the resist during the different steps of processing. One can find the different parameters that we used to process the resist. We introduce also an iterative method to adjust the illumination parameters with regard to the final structure, i.e. after the development step.

Chapter 5 presents a selection of periodic microstructures intended for optical applications like Diffractive Optical Elements (DOEs). They present an illustration of the potential of FS in the realization of DOEs. In particular, novel profiles to achieve a 1 to 5 fan-out are proposed. These fan-out elements were designed to have the highest possible efficiency and deviation angle.

Chapter 6 consists in a few applications of nanostructures for Optically Variable Devices (OVDs) for optical security against counterfeiting. Beside their spectacular visual appeal, they show very interesting polarization properties.

Chapter 7 summarizes the conclusions of the work and chapter 8 lists the references of the dissertation.

CHAPTER 2

FABRICATION OF SURFACE-RELIEF MICROSTRUCTURES

In this chapter, we present an overview of the technologies used to realize the structures that were fabricated. Most of these microstructures were designed to be integrated into OVDs (Optically Variable Devices) for visual security applications, in particular the authentification of documents such as passports, credit cards or banknotes. Therefore, the structures have to fulfill some special needs for these specific applications.

In order to obtain nice and spectacular visual effects to the eye, in particular in color and polarization, the interesting range of periods for these structures lies between a few tens of micrometers and a few hundreds of nanometers. Structures with larger or smaller period have little influence on the light diffraction in the visible wavelength range.

Furthermore, for the visual effect to be seen by the naked eye, a structured area of at least a few square millimeters is required.

For the needs of low cost mass production, such particular structures must be easily replicable. In our case, structures are transferred in a nickel shim by electroforming in a first step. The obtained master and its underlying copies serve then to produce replicas by stamping the microstructures into a foil of metal. The replicas can be further processed by the deposition of a stack of dielectric layers or metallic layer. Surface-relief structures are therefore ideally suited provided that the profile of the structures does not have any overhangs, as they cannot be replicated than. Furthermore, the height of the surface-relief structures must fit within the thickness of the foil of metal, in which the final structure is stamped. The thickness of the metal layer is typically a few tens of micrometers.

On the other hand, the profile accuracy on this kind of structures as well as the homogeneity over the structured surface area is not as critical as for industrial or purely optical applications.

These considerations have mainly determined our choice among existing fabrication processes. Two technologies, binary lithography and interference lithography, are used to originate surface-relief profiles in a sheet of photo-sensible material, in our case photoresist. They suit ideally our needs for the fabrication of structures for OVDs as well as for other fields.

2.1 Binary mask photolithography

Photolithography is a well-known and established technology in the field of the semiconductor fabrication. It is a multi-step process where light passes through openings in a chromium mask defining the location of electronic devices and wires and falls then onto a sheet of photosensitive material coated on a wafer. It is used mainly to manufacture VLSI (Very Large Scale Integration) circuits for microelectronics. Today's photolithography allows feature sizes of about 90nm.

As the sizes of those features are in the same order of magnitude as those needed in micro-optics, this mature technology has been adapted with success to the fabrication of optical microstructures as well as diffractive optics [Swanson 1989, Veldkamp 1983].

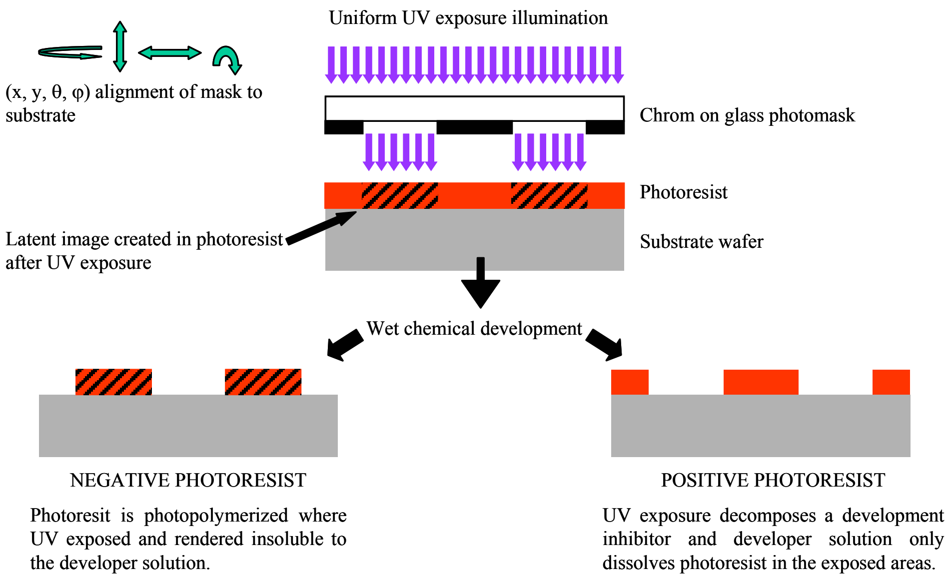

Figure 2.1. Photolithography process steps for the binary mask technology. The resist can be either of positive or negative type, where the exposed, respectively unexposed resist is then washed away during the development process. The resulting binary structure can then be transferred into glass using reactive ion etching (RIE) or be directly replicated.

The basic principle of all photolithographic techniques is to illuminate a radiation-sensitive material, a polymer like photoresist for example, with UV light through a mask. This mask defines where and how much light will expose the photosensitive material. In our case, the mask consists of a substrate and a chromium layer, whose openings let the light pass through the mask, where it exposes the resist. The light that hits the chromium is absorbed or reflected back and the underlying resist is therefore not exposed. Note that other types of masks used in gray-tone lithography [Däschner 1996, Gimkiewicz 1999] allows the light to be more or less absorbed, resulting in a continuous variation of the transmittance function and therefore the illumination intensity over the resist sheet. The photolithographic process is divided in several steps, as shown in Fig. 2.1.

First, a layer of resist must be deposited on a substrate, usually by pouring a drop of liquid resist on a spinning substrate. The substrate is initially dehydrated in an oven and coated by evaporation of a layer of HMDS (Hexa-Methyl-Dy-Benzene) to ensure better adhesion of the resist layer. The resist layer is then exposed to uniform UV light through the chromium mask. The radiation alters the chemical composition of the resist by either a cross-linking or a photochemical reaction on the chains of polymer. During the following development process, the exposed regions will remain or will be dissolved depending if the resist is of positive or negative type, respectively. The resulting surface-relief profile has a binary shape and can then be transferred into glass, using reactive ion etching (RIE), or can be directly replicated. Note that in the case of positive resist, the remaining polymer, which was not exposed to radiation, can be further exposed in a next step. Interference lithography, for example, can then be used to expose additional features, adding degrees of freedom for the design of optical effects.

2.2 Interference lithography

Diffractive optical elements (DOEs) are often fabricated by using technologies like laser-beam writing, e-beam writing, chromium and gray-tone mask lithography. All these technologies have their strength and weaknesses, but generally there is always a compromise between feature size and structured area size. When large areas, i.e., of the order of a few square centimeters and more, of fine periodic structures are needed, other technologies must be used due to the extremely long writing times such scanning techniques imply at high resolution. Among them are techniques using the interference produced by two or more laser beams consisting of plane or spherical waves. These techniques are known as holographic recording or also interference lithography. By choosing light sources at relatively large distances, it is easy to illuminate large areas, and thus obtain large structured surfaces. Moreover, these structures are spatially coherent over the whole surface of the recording plane and the periodicity of the obtained structures is highly accurate.

A further advantage of optical interference is that it occurs in the volume. Consequently, the depth-of-field does not limit these techniques by themselves. In the case of surface-relief structures, by exposing a thick layer of photoresist, for example, it is possible to realize very deep structures, i.e. aspect ratios (depth to period ratio) larger than 1.

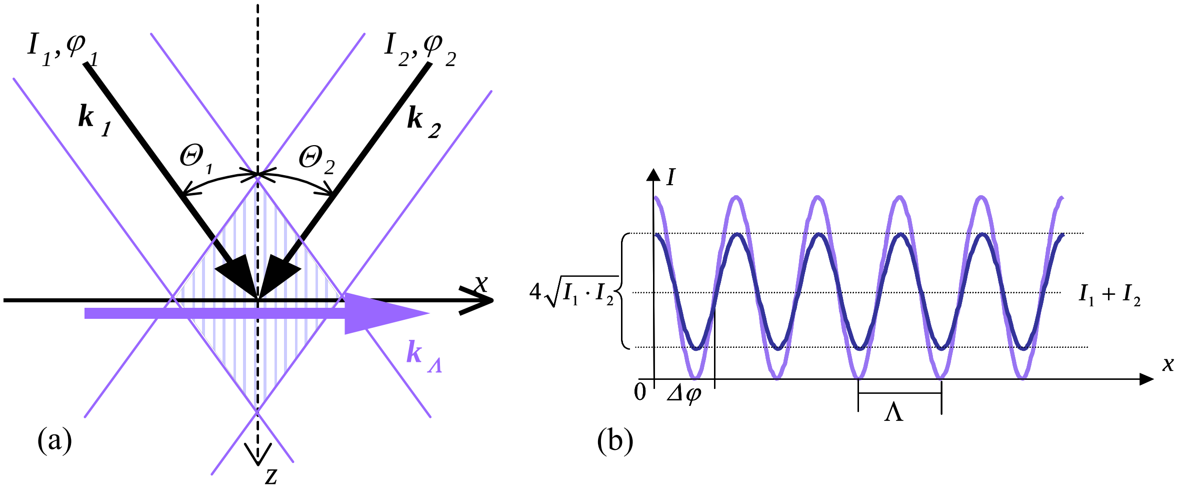

Figure 2.2. (a) Principle of two-beam interference for two plane waves. $\boldsymbol{k}_\Lambda$ is the wavevector associated with the resulting sinusoidal intensity distribution.

(b) Intensity of the resulting interference pattern. The bright curve represents the case where both beams have the same intensity. The contrast or amplitude of the interference pattern decreases if both beams do not have the same intensity as is represented by the dark curve. $\Delta\varphi = \varphi_2 - \varphi_1$ is the phase difference between both beams.

In the case of a single exposure with two interfering beams of coherent light, the illuminated pattern consists of a periodic sinusoidal intensity distribution, whose period is given by the incidence angle and the wavelength of the light of the incoming beams, as shown in Fig. 2.2. Equation (2.1) describes the intensity distribution generated by two plane waves with intensities I_1 and I_2 and phases φ_1 and φ_2, respectively, according to the situation shown in Fig. 2.2. :

$$I = I_1 + I_2 + 2 \cdot \sqrt{I_1 \cdot I_2} \cdot \cos(\boldsymbol{k} \cdot \boldsymbol{r} - \Delta\varphi) \tag{2.1}$$

Applying such an illumination pattern on a layer of resist and after development, the resulting structure becomes more or less a distorted sine, because of the nonlinear response of the recording material. Although period and depth of the periodic structure can be set with a moderate effort, as a drawback is the lack of flexibility on the shape of the profile.

Several illuminations can be sequentially exposed in the photosensitive material. Depending on the orientation and period of the exposed intensity distributions, the structures can have a one- or two- dimensional periodicity. Therefore, two cases will be investigated.

In the Fourier synthesis, we will focus on one- dimensional periodic structures produced by multiple synchronized exposures. That means that the phase and period of all exposures are in an exact relation. The method can also be applied for two- dimensional structures in the case where both direction of periodicity are independent.

In the second case, we will look at structures produced with the moiré phenomenon that consists in a large amplitude modulation of a fine period structure. The periodicity of the modulation, as well as of the fine period structure can be one- or two- dimensional, depending on the arrangement of the different exposures. The method is well suited for two- dimensional structures because the various exposures don't have to be synchronized, i.e. the pattern of the modulation and the fine period structure don't have to be in an exact relation.

2.2.1 Fourier Synthesis

To obtain better control over the shape of the grooves, on one hand, one could augment the number of interfering beams [Iemmi 1986, Chen 1988]. On the other hand, one could use a large number of sequentially exposed interference patterns [Breidne 1979]. In both cases very complex interference patterns can be obtained. In the following, we will focus on the latter case.

According to Eq. (2.1), the intensity distribution of two beam interference with planar waves is sinusoidal. Yet, the shape of any periodic surface profile can be decomposed into its Fourier components, which consist of sinusoidal functions with frequencies that are integral multiples (so-called harmonics) of the basic frequency. The inverse of the basic frequency refers to the period of the final structure. These Fourier components may also include a phase shift. The basic idea is to sum up these Fourier components, each corresponding to an independent exposure, whose duration determines the amplitude of the component and whose incidence angle determines the period of the component. This is also called Fourier Synthesis [Fleming 1997].

For real one-dimensional and periodic functions, the Fourier series can be written in the complex notation

$$f(x) = \sum_{n=-\infty}^{n=+\infty} c_n \cdot e^{i \cdot n \cdot k \cdot x} = \sum_{n=-\infty}^{n=+\infty} \left| c_n \right| \cdot e^{i \cdot (n \cdot k \cdot x + \varphi_n)} \quad , \tag{2.2}$$

with

$$c_n = \frac{1}{\Lambda}\int_0^{\Lambda} f(x)\cdot e^{-i\cdot n\cdot k\cdot x}\cdot dx \ , \tag{2.3}$$

where c_n are the complex Fourier components of *f(x)*. Λ is the period of *f(x)*, n is an integer number, $|c_n|$ and φ_n are the amplitude and phase of the complex number c_n, respectively.

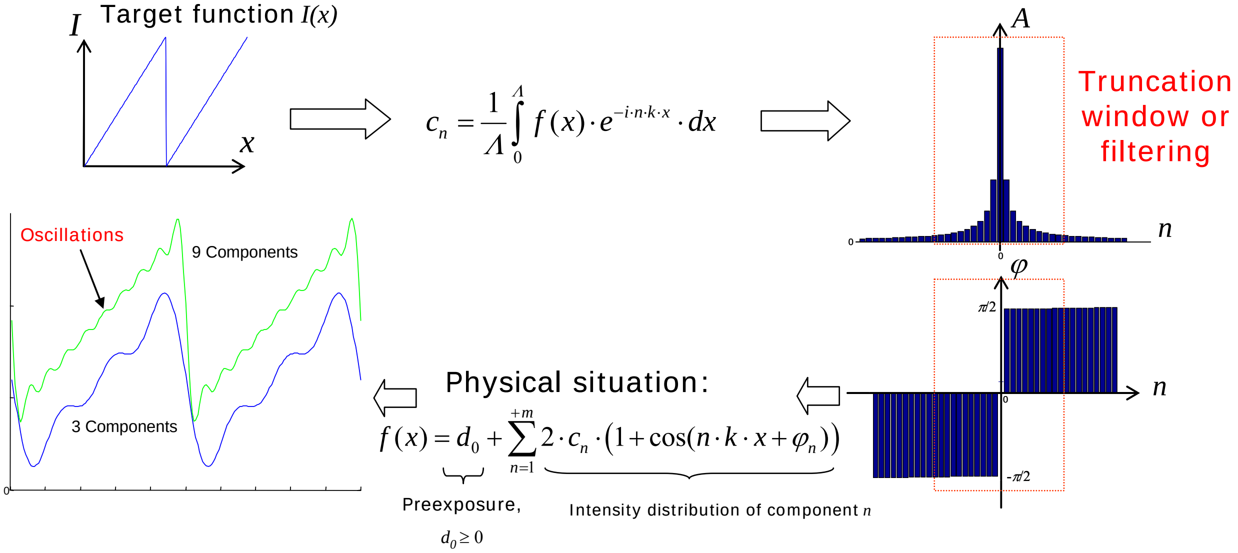

Figure 2.3. Schematic of the Fourier synthesis for a sawtooth profile as target function. Since such function shows a discontinuity, the truncation of its Fourier series causes the final profile to oscillate around the target profile, and an overshooting at the discontinuity.

Since *f(x)* is a real function, in our case it is an intensity distribution, its spectrum is symmetric and thus Eq. (2.3) can be rewritten in a form that represents real functions:

$$f(x) = c_0 + \sum_{n=1}^{+\infty} 2\cdot c_n\cdot\cos(n\cdot k\cdot x+\varphi_n) \tag{2.4}$$

To better represent the physics of our experiment, we can further rewrite Eq.(2.4), so that the sinusoidal terms behind the sum oscillates between zero and c_n similarly to relation (2.1), for beams having equal intensities. By including an offset to each n-th term, we obtain:

$$f(x) = d_0 + \sum_{n=1}^{+\infty} 2\cdot c_n\cdot\left(1+\cos(n\cdot k\cdot x+\varphi_n)\right) \ , \tag{2.5}$$

where $d_0 = c_0 - 2(c_1 + c_2 + \dots)$ is a constant. This effect is being represented for a sawtooth target function in Fig. 2.3, for 3 and 9 Fourier components. One can observe how the offset augments with increasing number of Fourier components. In this form, c_n and φ_n represent directly the amplitude and respectively the relative phaseshift of the interfering beams' intensity distribution for each *n-th* component that we record. Figure 2.4 shows the realized sawtooth profiles with various numbers of Fourier components. These profiles were illuminated in a resist layer by exposing each Fourier component sequentially. One can see how the intensity profile shifts to the up with increasing number of Fourier components. The structures have a period of 4.4µm and are made of positive resist. The effects of the resist response and the development process can be seen in particular at the erosion of the top and at the enlargement of the bottom of the realized profiles. For instance, the realized profile for 2 components should have had its stair at half maximum. Note that due to the resist effects, the profile for the first component would not be a sinus. The right side of Fig. 2.4 shows numerical simulations of each illuminated Fourier harmonic *n* (represented in bright) and the resulting profile (in dark).

In our experiment, the term d_0 represents a constant intensity distribution or preexposure. Since the intensity cannot become negative, the term d_0 in Eq. (2.5) has to be either zero or positive. In other words, depending on the Fourier spectrum of the desired intensity distribution, there will always be a minimum exposure dose coming from the added mean values of each sequential exposure. Depending on the response of the optical recording material, this minimal dose can shift the intensity distribution outside of the dynamic range of the material's response. In the worst case, this physical requirement can therefore, even hamper the realization of a desired structure, i.e., where d_0 would have to be less than zero. In other cases, the value of d_0 can be freely increased (by making a preliminary preexposure, for example) to shift up the whole intensity distribution to the desired intensity level. Figure 2.5, shows an example of an even profile, which cannot be illuminated because the mean values coming from each sinusoidal exposure add up to be more than the mean value of the desired distribution. Thus, all even distributions where the mean value lies below half of the maximum $hm = 0.5(c_0 + c_1 + c_2 + \dots)$ cannot be generated. The maximum is defined as the sum of all coefficients, which corresponds to the function's maximum for even functions. A distribution with the mean value *mv* lying above the half maximum *hm* can be obtained by adding a constant value to the distribution (by making a preliminary preexposure to the samples, for example). Note, however, that by adding a constant value, the distribution itself changes since it depends nonlinearly on the desired surface profile via the material's (photoresist in our case) response and it needs an optimization procedure to find *mv*=*hm*.

(a) 2 components

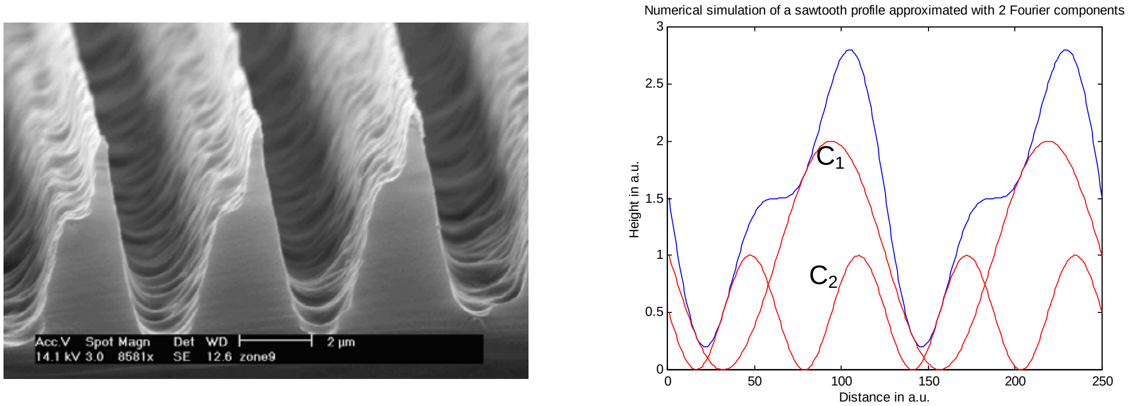

(b) 3 components

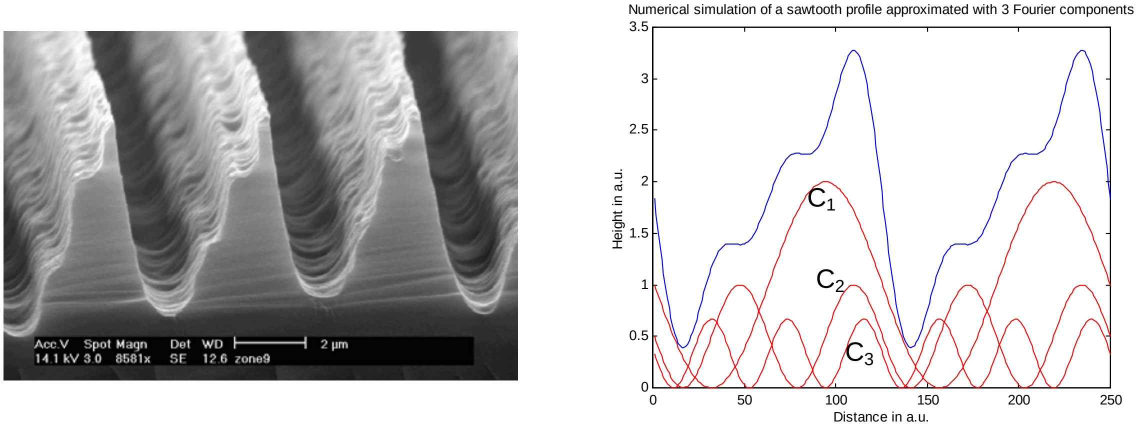

(c) 4 components

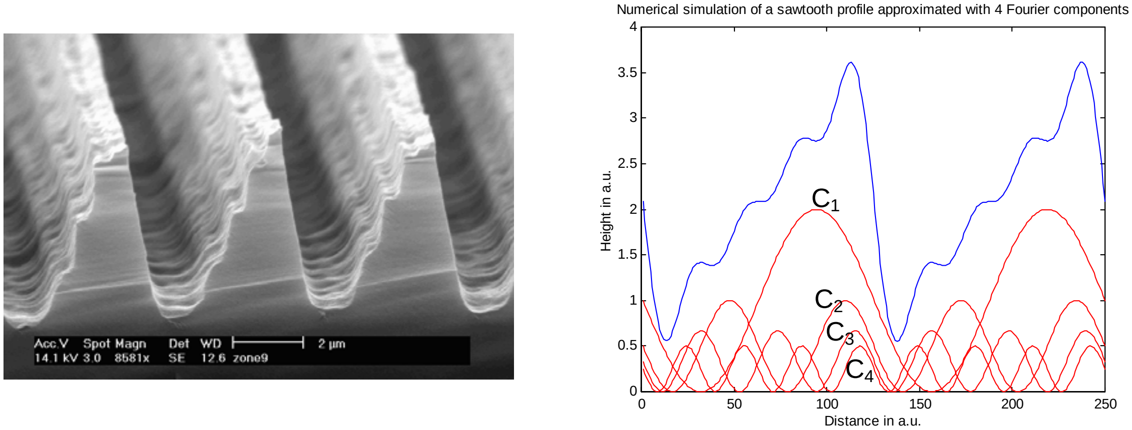

Figure 2.4. (a) Sem picture of a realized sawtooth profile with 2 components and the according numerical simulation. The Fourier coefficients are 1 and ½ for C_1 and C_2 , respectively.

(b) Sem picture of a realized sawtooth profile with 3 components and the according numerical simulation. The Fourier coefficients are 1,½, and 1/3 for C_1, to C_3, respectively.

(c) Sem picture of a realized sawtooth profile with 4 components and the according numerical simulation. The Fourier coefficients are 1, ½, 1/3, and ¼ for C_1 to C_4, respectively.

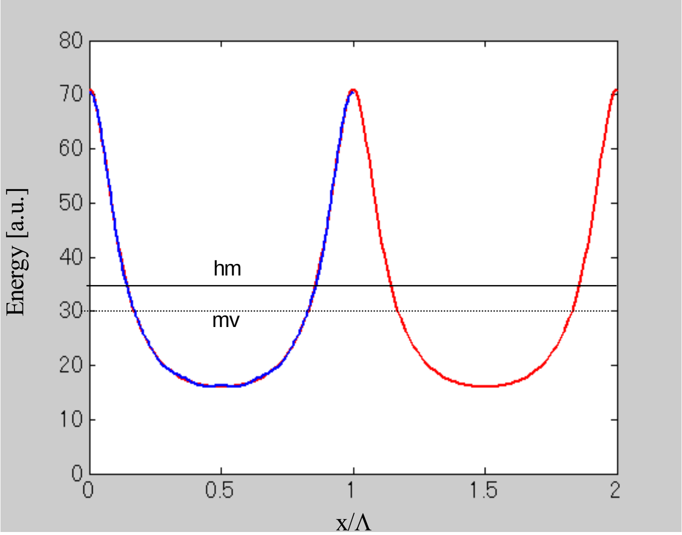

Figure 2.5. Example of a profile that cannot be realized because the condition of realization $mv \geq hm$ ($d_0 \geq 0$), for even functions, is not fulfilled.

Nevertheless, in some cases, the term d_0 is positive or can be set to zero. The phase difference between c_1 and the components c_n, for $n>1$, must involve $\pi/2$ for n even and zero for n odd. In other words, the cosinusoidal term of the mean frequency and the harmonics must have their minimums coinciding.

Although every periodic function can be decomposed into a Fourier series, which can consist of an infinite amount of cosine terms each with its proper phaseshift, only a finite amount of these harmonic components is reproducible.

Therefore, by truncating the Fourier components that lie outside of the usable frequency range, only an approximation of the desired profile can be obtained. The quality of this approximated profile depends strongly on the shape of the desired function. Generally, functions with a continuous profile can be approximated very well since the amplitude of the higher harmonics decreases quickly. Functions like prisms, or paraboloids, for example, can be well approximated with 5 components, because the amplitude of the *n*-th harmonic decreases with n^2. On the other hand, discontinuous functions, like binary or sawtooth functions, as represented in Figures 2.3 and 2.4 cannot be approximated so well. In these cases, the Fourier series additionally causes some overshooting at the discontinuities and approximates the step with a damped oscillation, as shown in Fig. 2.3, for 3 and 9 components. Unfortunately, this phenomenon is present for any number of Fourier harmonics. Only the oscillation amplitude diminishes when the number of Fourier components increases.

Nevertheless there are other series based on the Fourier expansion, such as the Fejer series [Chamberlain 1979], that damp out these spurious oscillations and thus better represent the desired function. Moreover, various kinds of frequency filters can be applied as well to attenuate this effect. This could be applied straightforward to our case.

2.2.2 Coherence length of periodic structures

One condition for successful fabrication of a specific non-sinusoidal structure is the degree of synchronization or coherence between the various harmonic components that are added up during the illumination process. If we consider the addition of two cosines in space with the same amplitude but slightly different frequencies, we can observe that the phase difference between both cosines changes with increasing distance. At a given point, the phase difference of both cosines is π, resulting in annihilation of both cosines. This phenomenon, which is also known as beating effect, occurs periodically with a so-called beating length or beating period depending on the magnitude of the frequency difference of both cosines. A similar effect occurs when the frequency difference of the two cosines is slightly off an integer and causes a periodic distortion of the grating profile, as can be seen in Fig. 2.6.

In the beginning of the fabrication process two questions need to be answered:

(a) How large do we want the structured surface to be, and
(b) how much distortion on the final structure can we tolerate?

In other words, since the frequencies of the recorded Fourier components are related to the incidence angle of our two interfering beams, how much precision do we need on that incidence angle?

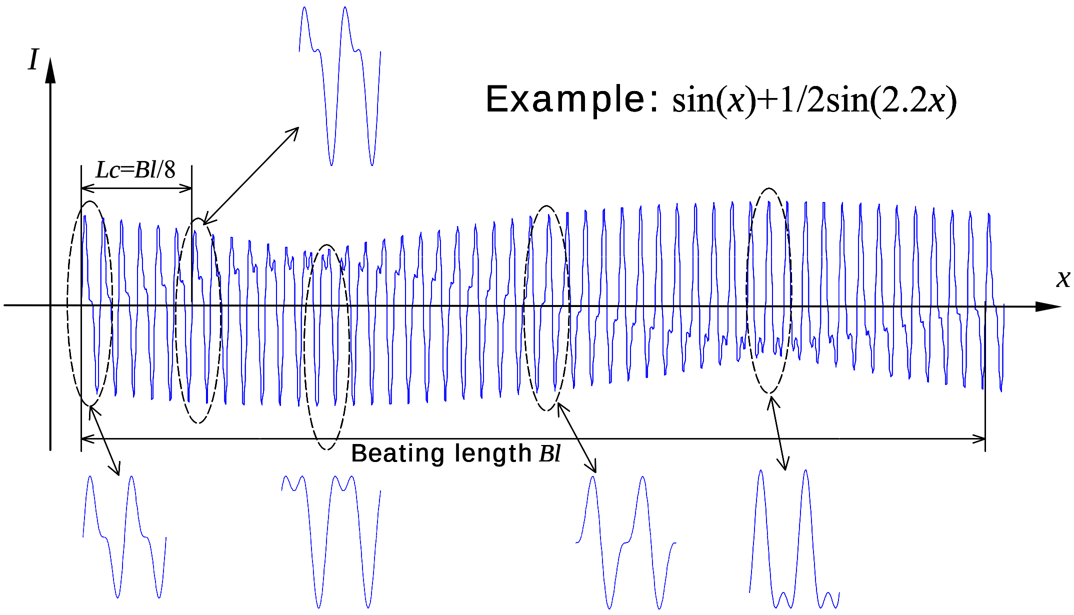

Figure 2.6. Illustration of the beating effect occurring when the second harmonic is slightly off of the first component of the Fourier series of a sawtooth profile function. Note that for the sake of representation, the second component is 20% off of the first component in this example.

Assuming a symmetrical arrangement, like in the geometry shown in Fig. 2.2 (a), the period Λ of the component is related to the incidence angle Θ by:

$$\Lambda = \frac{\lambda}{2 \cdot n \cdot \sin(\Theta)} , \tag{2.6}$$

where λ is the wavelength and n is the refractive index of the medium of incidence.
The error $\Delta\Lambda(\Theta_m) = \Lambda_m - \Lambda_{err}$ on the component period is given by the difference of the desired period $\Lambda_m = \Lambda_1/m$ of the component m and the period Λ_{err} obtained with the same angle as for Λ_m but with an absolute error $\Delta\Theta$ on the incidence angle and therefore $\Lambda_{err}=\Lambda_m(\Theta_m+\Delta\Theta)$. Note that the error $\Delta\Theta$ on the incidence angle Θ is the same over 360° for rotation tables like in our experiment. Λ_1 is the period of the first component, i.e. the period of the structure. For $\Lambda_m \approx \Lambda_{err}$,the beating length is then given by:

$$Bl_m = \frac{(\Lambda_m)^2}{\Delta\Lambda(\Theta_m)} \tag{2.7}$$

Finally, we define a coherence length for the structure

$$L_c = B l_m / 8 \tag{2.8}$$

to be an approximate size for which the structure remains almost undistorted. The factor 1/8 was chosen arbitrarily to give an approximation of the size of the useful structured region. It was shown to work well in all of our experiments.

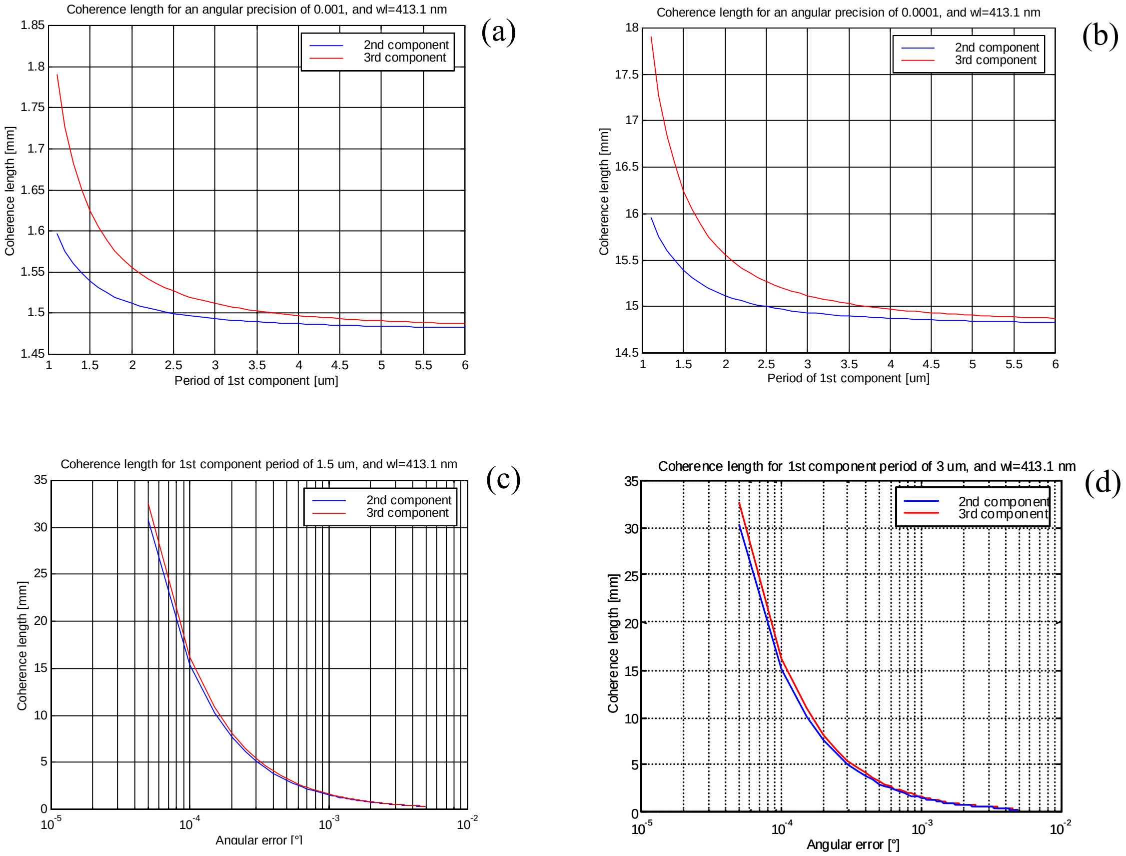

Figure 2.7. Behavior of the coherence length L_c of the structures, as defined in Eq. (2.7), with various errors $\Delta\Theta$ on the incidence angle Θ of the interfering beams and for various grating periods Λ. The wavelength is $\lambda = 413.1$ nm. One can see how the coherence length of the structure increases with better angular precision. Compare (a), where $\Delta\Theta = 0.001°$ and (b), where $\Delta\Theta = 0.0001°$. Note that for smaller structures, the coherence length increases as well, as can be seen by comparing (c), $\Lambda = 1.5\mu m$ to (d), $\Lambda = 3\mu m$.

If the incidence angle is very small, the grating period is very sensitive to a change of Θ. For larger angles of incidence, and thus smaller grating periods, Λ becomes less sensitive to Θ resulting in a higher accuracy of the component's period.

Therefore, L_c will mostly depend on the period of the first component, i.e. $m = 1$, and on the next harmonic m with a non-zero amplitude. For higher harmonics, the angular precision is less critical as can be seen on Fig.2.7. (a) and (b).

Looking at the graphs shown in Fig. 2.7. (a), we can see that for a 3 μm period structure and an angular error of 10^{-3} degree the coherence length would be approximately 1.5 mm. For larger structured areas, better angular precisions of the incidence angle are needed. For a 3 μm period structure with an angular error of $5 \cdot 10^{-5}$ degrees, the coherence length rises to about 30 mm, as can be seen in Fig. 2.7. (d). Note that due to the non-linearity of Eq. (2.6) in Θ, L_c diminishes for larger grating periods and inversely augments for shorter grating periods for a given angular precision.

Generally, the Fourier series of any function involve also an imaginary part, which results in a different phaseshift for each component. Consequently, the phaseshift or the relative position between each exposed Fourier component also affects the shape of the periodic structure and therefore the optical path difference between the two interfering beams has to be adjusted. With errors occurring during this adjustment, the coherence length diminishes as well. Thus, the absolute error Δ_{OPD} the system induces on the optical path difference OPD between both interfering beams generates an additional phaseshift of $(2\pi/\lambda)\cdot\Delta_{OPD}$. Putting it in relation with the period, we obtain the positioning error of the m-th component:

$$\varepsilon_m = \frac{\Lambda_m \cdot \Delta_{OPD}}{\lambda} \qquad (2.9)$$

Therefore, considering this additional error, the coherence length decreases to a value $L_c - \varepsilon$.

2.2.3 Moiré effects

In this subsection, we look at fine periodic structures which height is modulated by a much larger periodic pattern (at least 10 times larger then the fine structure) using the moiré phenomenon. In terms of intensity diffraction, this translates into nice looking color effects that constantly and smoothly vary while tilting the sample. As the method is applicable to the superimposition of gratings having different directions with moderate effort, it was mostly used for two-dimensional periodic structures.

The moiré phenomenon is a well known phenomenon occurring when two sets of periodic structures such as grids, gratings or arrays of dots are superimposed, where the two sets differ slightly in period, relative size or orientation. The resulting moiré effect can produce interesting and beautiful geometric patterns, which are not present in any of the original structures.

One of the more common occurrences of moiré patterns is found in computer monitors and television sets where we see an ordered wavy pattern superimposed over the screen in a series of ripples. Moiré patterns also are a common problem in scanned images due to interference between the printed dot pattern and the near equidistant resolution of the scan of the image.

Figure 2.8 shows an example where two sets of grids, which differ in period, in one case, and in orientation in the other case are superimposed. In that particular case, both sets consists of periodic structures having binary intensity levels.

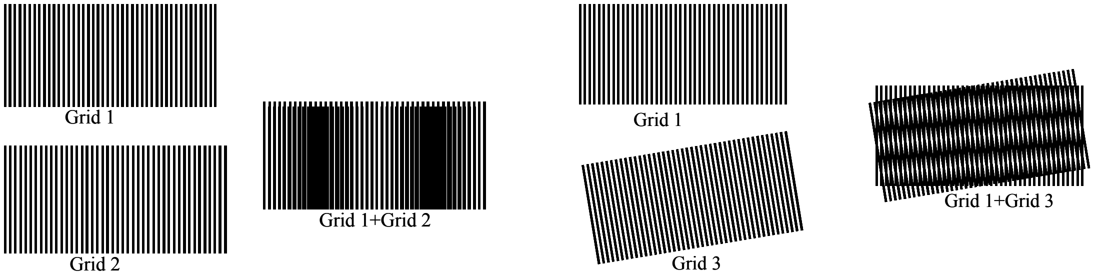

Figure 2.8. Moiré patterns occurring by superimposition of two sets of grids, where Grid 2 differs slightly from Grid 1 in period whereas Grid 3 differs from Grid 1 in angle only. One can see how the moiré fringes, stripes in this case, change in size and orientation.

Several mathematical approaches can be used to investigate the moiré phenomenon. Among them are the classical geometric approach [Nishijima 1964, Yule 1967], based on the relation between the geometrical entities, like triangles or parallelograms, produced by the moiré effect, or the indicial equation method [Oster 1964], a pure algebraic approach.

In this section, however, we will use a spectral approach, which is based on the Fourier theory, to investigate the moiré effect.

We will focus on the case where two or more sinusoidal intensity gratings of the form $A\cdot\cos(\boldsymbol{k}_i\, \boldsymbol{r} - \varphi_i)$ are superimposed, as is the case when independent exposures are done by two-beam interference lithography. Note that we consider gratings, which have all the same amplitude A. The superimposition of gratings with different amplitudes would result in a degradation of the contrast of the moiré fringes but not in its two-dimensional

arrangement. For the sake of simplicity, we will omit the phase term φ_i as it only describes the relative position of the moiré pattern around a reference point in the plane.
The resulting intensity distribution consists of the addition of intensity gratings given by

$$I(\boldsymbol{r}) = I_0 + \sum_{i=1}^{n} \cos(\boldsymbol{k}_i \cdot \boldsymbol{r}) \ , \tag{2.9}$$

where I_0 is a constant larger than zero, $\boldsymbol{r} = \boldsymbol{r}\,(x,y)$ is the displacement vector in the recording plane, and $\boldsymbol{k_i}$ ($|\boldsymbol{k_i}| = 2\pi/\Lambda_i$ and Λ_i is the period of the i-th grating) is the wave vector of each sinusoidal grating.
Let us first consider the case where two cosinusoidal gratings are superimposed. If we put the sum in a multiplicative form, we obtain:

$$I(\boldsymbol{r}) = I_0 + 2 \cdot \cos\left(\frac{\boldsymbol{k}_1 + \boldsymbol{k}_2}{2} \cdot \boldsymbol{r}\right) \cdot \cos\left(\frac{\boldsymbol{k}_1 - \boldsymbol{k}_2}{2} \cdot \boldsymbol{r}\right) \tag{2.10}$$

Now, we get a high frequency term $(\boldsymbol{k_1} + \boldsymbol{k_2})\ /2$, which is the fine period grating, modulated by a low frequency term $(\boldsymbol{k_1} - \boldsymbol{k_2})\ /2$, which is the large period grating.

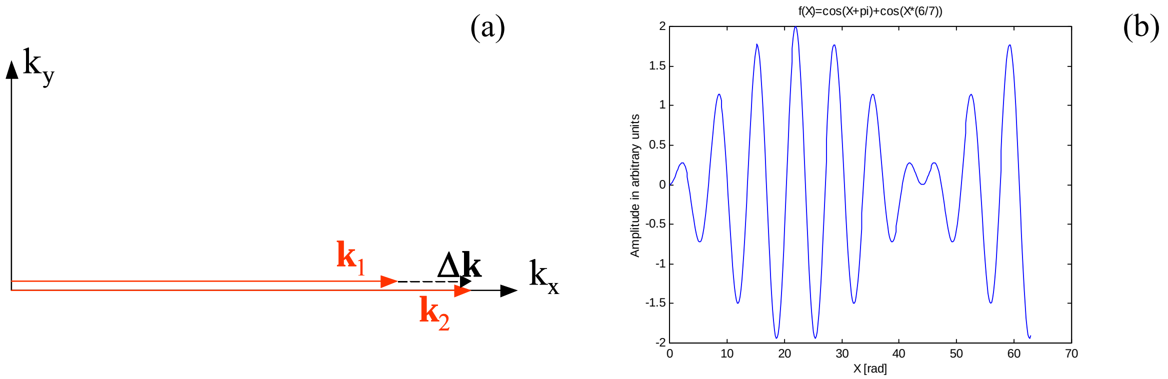

Figure 2.8. (a) Situation of the wave vectors of both cosine gratings. For the sake of clarity, only the right part of the spectrum is shown, as it is symmetric around the origin and the vector lengths are in arbitrary units. The dotted line represents the difference between both wave vectors and thus orientation and period of the modulation. In this case, the modulation is parallel to the sub-grating.
(b) Plot of the resulting function of the superposition of two cosinusoidal gratings, which amplitude is one and which relation in frequency is 6/7 corresponding to the vector situation of $\boldsymbol{k_1}$ and $\boldsymbol{k_2}$ in (a).

The multiplicative form is useful for the graphical interpretation, because the Fourier transform of a product of two functions can be understood as a convolution of the Fourier transform of each function.

Thus, the Fourier transform of Eq. (2.10), can be seen as the convolution of the Fourier transformation of each cosine, which consists in a symmetric impulse (or dirac) functions located at $(\boldsymbol{k_1}+\boldsymbol{k_2})/2$ and $-(\boldsymbol{k_1}+\boldsymbol{k_2})/2$ for the first cosine and $(\boldsymbol{k_1}-\boldsymbol{k_2})/2$ and $-(\boldsymbol{k_1}-\boldsymbol{k_2})/2$ for the second cosine. If both wave vectors $\boldsymbol{k_1}$ and $\boldsymbol{k_2}$ are relatively close to each other or, in other words, if the difference between both vectors is small, then $(\boldsymbol{k_1}+\boldsymbol{k_2})/2 \cong \boldsymbol{k}$ and the resulting moiré pattern consists of a cosinusoidal modulation, whose direction and periodicity is given by $\boldsymbol{\Delta k} = (\boldsymbol{k_1}-\boldsymbol{k_2})/2$, of the cosinusoidal grating. The period and direction of this grating is given by $\boldsymbol{k}$.

Figure 2.8 shows the superimposition of two cosinusoidal gratings with $\boldsymbol{k_1} \cong 0.86\,\boldsymbol{k_2}$ and the accordingly fabricated structure. One can observe the sinusoidal shaped envelope of the modulation. In this case, $\boldsymbol{k_1}$ and $\boldsymbol{k_2}$ are parallel.

Let us now consider the case where three or more sinusoidal intensity patterns with same amplitude are added. By pairing the cosine terms and with a few algebraic transformations, Eq. (2.9) can be rewritten as:

$$I(\boldsymbol{r}) = I_0 + \cos\left(\frac{1}{2}(\boldsymbol{k}_1+\boldsymbol{k}_2)\cdot\boldsymbol{r}\right)\cdot\cos\left(\frac{1}{2}(\boldsymbol{k}_1-\boldsymbol{k}_2)\cdot\boldsymbol{r}\right)+$$

$$\cos\left(\frac{1}{2}(\boldsymbol{k}_2+\boldsymbol{k}_3)\cdot\boldsymbol{r}\right)\cdot\cos\left(\frac{1}{2}(\boldsymbol{k}_2-\boldsymbol{k}_3)\cdot\boldsymbol{r}\right)+\ldots+\cos\left(\frac{1}{2}(\boldsymbol{k}_n+\boldsymbol{k}_1)\cdot\boldsymbol{r}\right)\cdot\cos\left(\frac{1}{2}(\boldsymbol{k}_n-\boldsymbol{k}_1)\cdot\boldsymbol{r}\right) \qquad (2.11)$$

Let us assume that $\boldsymbol{k_1} \cong \boldsymbol{k_2} \cong \ldots \cong \boldsymbol{k_n} \cong \boldsymbol{k}$, and therefore $(\boldsymbol{k_i}+\boldsymbol{k_j})/2 \cong 2\boldsymbol{k}$. Altough all grating vectors have nearly the same direction and the same length, the differences $\boldsymbol{\Delta k_{ij}} = (\boldsymbol{k_i}-\boldsymbol{k_j})/2$ between vectors are not zero. We can rewrite Eq. (2.11) further:

$$I(\boldsymbol{r}) = I_0 + \cos(\boldsymbol{k}\cdot\boldsymbol{r})\cdot\left[\cos\left(\frac{1}{2}(\boldsymbol{k}_1-\boldsymbol{k}_2)\cdot\boldsymbol{r}\right)+\cos\left(\frac{1}{2}(\boldsymbol{k}_2-\boldsymbol{k}_3)\cdot\boldsymbol{r}\right)+\ldots+\cos\left(\frac{1}{2}(\boldsymbol{k}_n-\boldsymbol{k}_1)\cdot\boldsymbol{r}\right)\right] \qquad (2.12)$$

In this form, the spectrum $\hat{I}(\boldsymbol{r})$ consists of the convolution of the small pattern, a linear grating whose period and orientation is defined by $\boldsymbol{k}$, with a large modulation (consisting in the moiré fringes), whose two-dimensional arrangement is given by the orientation and length of the vector differences $\boldsymbol{\Delta k_{ij}} = (\boldsymbol{k_i}-\boldsymbol{k_j})/2$ between the wave-vectors of each sinusoidal intensity pattern. Some examples are presented in Figures 2.9 and 2.10.

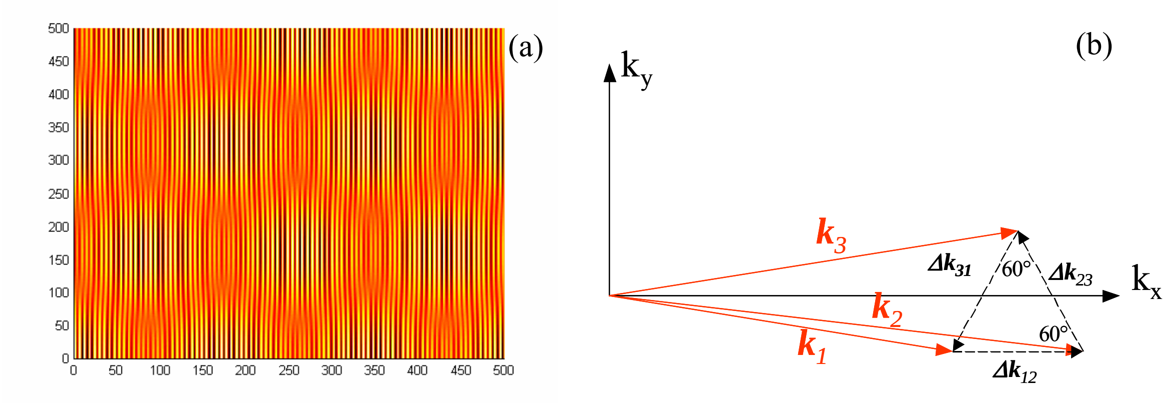

Figure 2.9. (a) Numerical simulation of a hexagonal moiré pattern with a linear grating as sub-modulation. All vectors $\boldsymbol{k}_1$ to $\boldsymbol{k}_3$ have nearly the same direction and length, and thus the fine pattern is a linear grating. The axes are in arbitrary units.
(b) According *k*-vector scheme (only the right side is represented) showing the arrangement of the three sinusoidal intensity patterns in the Fourier space. The differences $\boldsymbol{\Delta k}_{12}$, $\boldsymbol{\Delta k}_{23}$ and $\boldsymbol{\Delta k}_{31}$ determine the shape of the moiré pattern that modulates the fine grating.

By looking in the Fourier plane, one can then graphically determine how the various exposures must be arranged, in period as well as in orientation in the plane, in order to obtain the desired moiré pattern and sub-modulation. Note that for periodic moiré patterns, the possibilities are restricted to basic cells with a parallelogram shape (whose particular cases include the square, the rectangle, or the diamond) or a hexagonal shape.
Moreover, the sub-modulation is not restricted to a one-dimensional grating, but can be more complicated like crossed gratings or hexagonal structures. Equation (2.9) has then to be arranged in a form like

$$I(\boldsymbol{r}) = I_0 + \sum_{i=1}^{m} \cos(\boldsymbol{k}_i \cdot \boldsymbol{r}) \cdot \left[\cos\left(\frac{1}{2}(\boldsymbol{k}_{i1} - \boldsymbol{k}_{i2}) \cdot \boldsymbol{r}\right) + \cos\left(\frac{1}{2}(\boldsymbol{k}_{i2} - \boldsymbol{k}_{i3}) \cdot \boldsymbol{r}\right) + \ldots + \cos\left(\frac{1}{2}(\boldsymbol{k}_{in} - \boldsymbol{k}_{i1}) \cdot \boldsymbol{r}\right) \right], \qquad (2.13)$$

where the sinusoidal gratings are arranged into *m* clusters of *n* vectors. The vectors of a cluster *m* must be sufficiently near one to each other (in other words, the difference between all pairs of vectors of a cluster *m* have to be small enough) so that we can assume $(\boldsymbol{k}_{mi} + \boldsymbol{k}_{mi+1})/2 \cong \boldsymbol{k}_m$, $\forall i$. In this form, the $\boldsymbol{k}_m$ determine the arrangement of the sub-modulation, and the *n* differences $(\boldsymbol{k}_{m1} - \boldsymbol{k}_{m2})/2$, $(\boldsymbol{k}_{m1} - \boldsymbol{k}_{m2})/2$, ..., $(\boldsymbol{k}_{mn} - \boldsymbol{k}_{m1})/2$ determine the arrangement of the moiré fringes. In the Fourier space or *k*-vector space, this can be seen as a convolution of the Fourier transformation of the moiré pattern function and the Fourier transformation of the sub-modulation function. Example (c), in Fig. 2.9, illustrates this behavior.

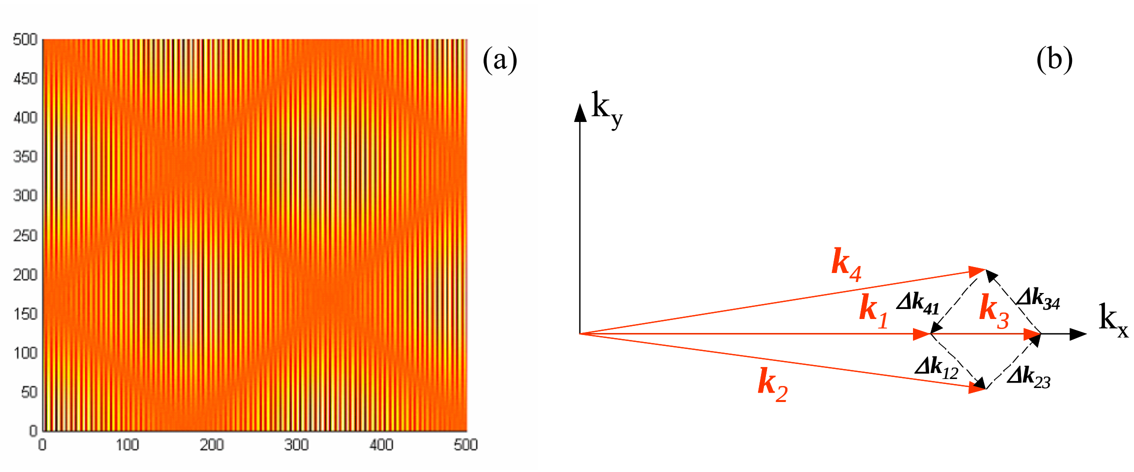

Figure 2.10. (a) Numerical simulation of a square moiré pattern with a linear grating as sub-modulation. All vectors $\boldsymbol{k}_1$ to $\boldsymbol{k}_4$ have nearly the same direction and length, and thus the fine pattern is a linear grating. The axes are in arbitrary units.

(b) According scheme in the k-vector space, showing the arrangement of the four sinusoidal intensity patterns in the Fourier space. The differences $\Delta\boldsymbol{k}_{12}$, $\Delta\boldsymbol{k}_{23}$, $\Delta\boldsymbol{k}_{34}$, and $\Delta\boldsymbol{k}_{41}$ determine the shape of the moiré pattern that modulates the fine grating.

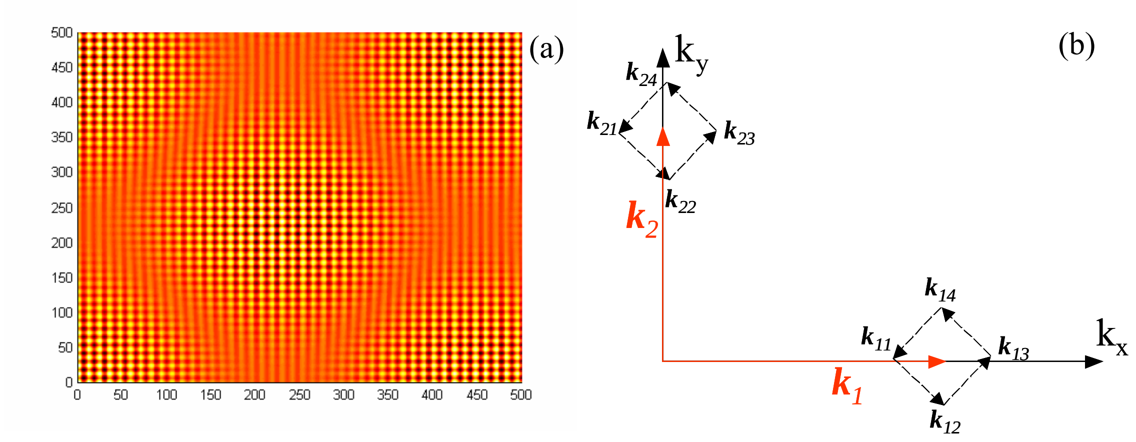

Figure 2.11. (a) Square moiré pattern as in Fig. 2.10, but with a square crossed grating for the sub-modulation.

(b) Arrangement of the eight gratings vectors. Only the tip of each grating vector $\boldsymbol{k}_{mn}$ is represented. As can be seen, the gratings are arranged in two clusters of four vectors centered on $\mathbf{k}_1$ and $\mathbf{k}_2$ (which are related to the fine crossed grating). The doted lines represent the vector differences, which are related to the large modulation or moiré fringes.

2.3. Summary

In this chapter, we presented the fabrication technologies that we have used to fabricate the microstructures. We showed that arbitrary profiles can be synthesized using two-beam interference lithography. The method is limited by the number of Fourier components that can be produced by the exposure system and the recording material properties. Fabrication errors (in particular, the accuracy on the recording angle) limit the maximum area size of the useful realized grating structure. To describe the limitation, we introduced the (spatial) coherence length for the microstructures. This value gives an approximation for the effective structured area for which the structure profile can be considered invariant. For a structure period of 3µm, and an error on the incidence angle of 10^{-3} degrees, the coherence length is 1.5mm. We have also shown that very complex structures can be produced using the moiré phenomenon. Some examples were shown using a few simple rules to determine the shape and arrangement of the final structures.

CHAPTER 3

SETUPS FOR INTERFERENCE LITHOGRAPHY

Interference lithography or holographic recording is the preferred method for fabricating periodic and quasi-periodic patterns that must be spatially coherent over large areas. It is a conceptually simple process where two or more coherent beams interfere to produce a standing wave, which can be recorded in a photoresist. The spatial-period of the grating can be as fine as half the wavelength, if the interferences occur in air. In dense media, the minimum period is reduced in proportion of the refractive index.

In this chapter, we present various kinds of arrangements of interferometers used to steer the multiple beams, which are involved to produce the various interference patterns. Depending on the nature of the light source, in particular its coherence length and output power, many configurations have been proposed and used in optical lithography [Beesely 1970, Ehbets 1995, Tsang 1974, Sheridon 1968]. A critical parameter for these setups is the mechanical stability, as the relative displacement during the exposure between interference pattern and substrate has to be much lower than the structure period, i.e. 20 nm for a 220 nm period (about 10% of the smallest period to record), in order to obtain high contrast.

Thermal stability can also be critical. For example, a temperature difference of 0.05°C causes a glass sample of 250mm to dilate by 85 nm – 100 nm, depending on the glass type.

The interferometers, which are described here, are all operated with a Krypton ion laser that has a coherence length in the meter range and an optical output power of a few watts at 413 nm. Although the laser can be operated at other spectral lines, the 413 nm line was the most adequate with regard to the spectral sensitivity of the resist we used. Moreover, at that wavelength the beam is still visible with the naked eye, which simplifies the alignment of the setup.

To obtain homogeneous microstructures, it is of great importance to avoid any parasitic interferences or optical noise produced by the unwanted scattering of the incident beams at the optical and mechanical elements of the recording setup. In our experiment, the samples consisted of standard glass plates covered with a layer of photoresist as recording material. Parasitic interferences occur at the glass-air interface at the back of the sample.

To take care of these very annoying back-reflections (as they occur very near to the resist layer), we matched whenever it was possible, a piece of absorbing glass (NG9 from Schott) to the back of the sample, which leads to very good results.

3.1 Two-point source setup

The two-point source setup described here, is one of the simplest interferometers used to realize gratings. Although, it is not very flexible, in particular when several exposures have to be done (involving different illumination angles), it is widely used throughout industry and research.

The interferometer, shown in Fig. 3.1, consists of a beam-splitter, which divides the laser beam into two equal parts, therefore of same intensity. Steering mirrors are positioned in each arm of the interferometer to set the incidence angles of the beams on the sample.

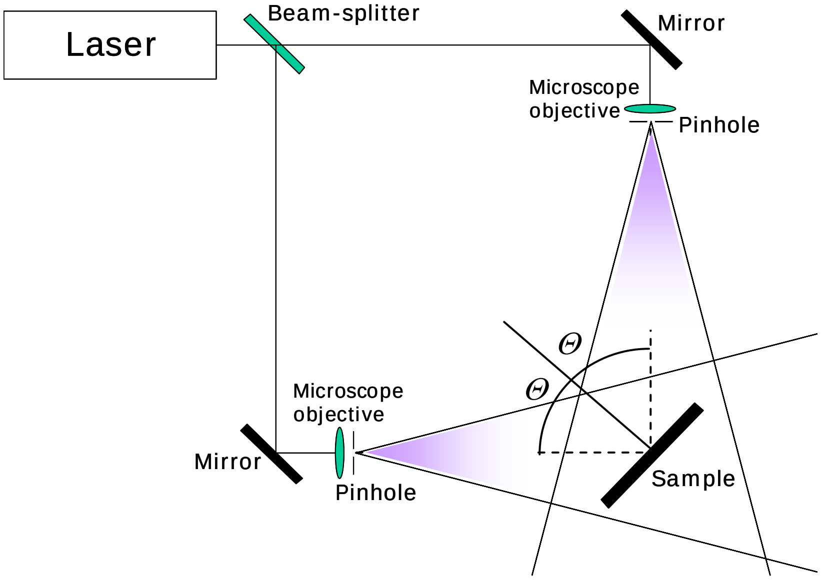

Figure 3.1. Schematic of an optical interferometer using two point sources. The incident laser beam is split into two parts, which are then expanded by microscope objectives and spatially filtered by pinholes. The interference pattern produced by the spherical waves coming from the pinholes is then recorded on the sample. The schematic is represented for an incidence angle of $\Theta = 45°$.

The beams are then expanded by microscope objectives and filtered by pinholes. The obtained waves, which will be used to produce the gratings, are therefore spherical. In order to realize a grating with constant period over the whole sample, the pinholes must be sufficiently far away from the substrate to get a good approximation of a plane wave over the area of the substrate.

The mechanical stability is very critical for this setup, because of the large distances between the point sources and the sample, in particular when the incidence angle of the beams on the sample is high. With higher incidence angles, the distances between beam-splitter and mirrors increase as well as the optical path length. For a structured area of a few square centimeters, the pinhole to sample distance should be at least 1.2m. Therefore the optical path differences can easily reach a few meters. A very rigid optical table as well as stable temperature conditions are of greatest importance to minimize optical path length differences and therefore ensure a stable interference pattern.

Note that an optical phase tracking system or fringe locking device can be used to compensate changes in the optical path lengths [Cescato 1999, Freijlich 1988]. Such systems typically measure the displacement of interference fringes that are produced by the recombination at a place near to the sample. To correct the optical path, the interferogram detection device is looped on a dynamic mirror or a pockels cell placed in one of the arms of the interferometer.

The advantages of this optical setup are, first, that the optical components are industrial standard and it is therefore relatively easy to start with relatively small effort. The obtained gratings are very homogenous and have little noise due to the far distance between sample and sources.

On the other hand, when several exposures are needed, for example to synthesize more complicated profiles, the setup is not adequate because the whole setup has to be realigned when setting different incidence angles. Moreover, angles with errors less than 0.1° are experimentally very difficult to realize.

3.2. Multiple exposures with controlled phaseshift setup

In two-beam interference lithography, the illuminated profile is limited to sinusoidal functions with a single exposure. If resist is used, the resulting surface-relief profile becomes a periodic u-shaped function determined by the resist’s response. To increase the degree of freedom on the profile, many ideas have been proposed, like the Sheridan technique [Sheridan 1968] or the Fourier synthesis, for example. In this section, we focus on the last of those two examples.

Already in the early 70’s, the high potential of the method has been recognized. In 1976, Johansson Nilson, Biedermann and Leveby [Johansson 1976] have done significant work in this field by proposing an optical setup, see Fig. 3.2 (a), which allows superposing Fourier components sequentially. Their interferometer consists of a beam-splitter, to obtain two interfering beams (which are then expanded and filtered separately), and a set of mirrors to recombine the beams on the substrate with the desired angle. In one of the arms of the interferometer, a movable mirror is implemented to change the incidence angle between both beams in order to obtain the various Fourier components. To precisely adjust the angle of incidence, a reference grating is illuminated on a ring around the area to structure in a first step. The period of the reference grating and the first harmonic are identical. The next higher Fourier component, corresponding to a separate exposure, is then adjusted by observing the interference fringes occurring by the superposition of the orders diffracted by the reference grating. Moreover, the so-obtained fringe pattern is also used for adjusting the relative phase between exposures. The phase is tuned by modifying the optical path difference between both beams thanks to another mobile mirror, which is implemented in one of the arms. Sawtooth profiles with two Fourier components could successfully be fabricated.

In 1988, Hershey, Chen, and Leith [Chen 1988] proposed another interferometer configuration using two identical diffraction gratings, shown in Fig. 3.2 (b).

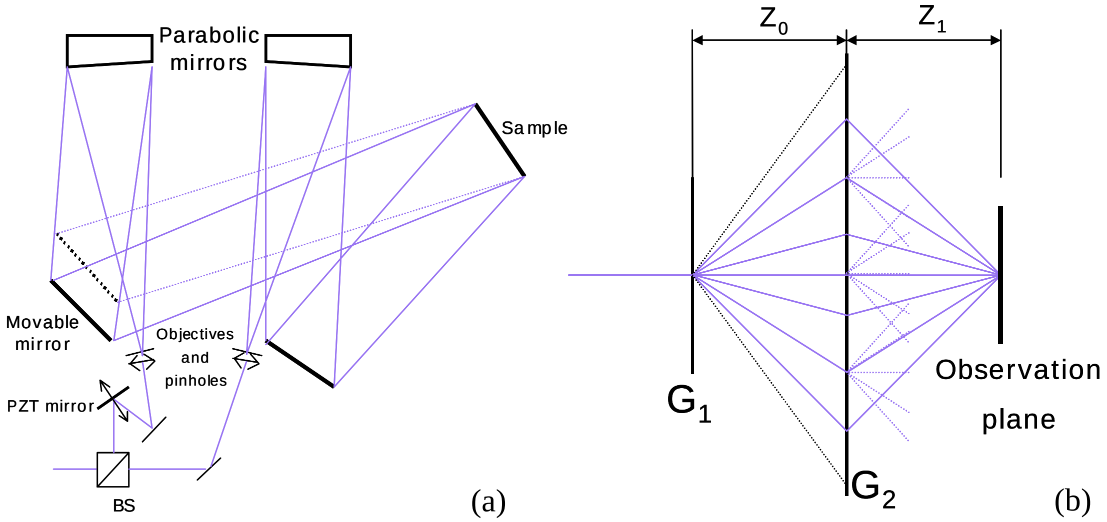

Figure 3.2. (a) Optical setup proposed by Johansson Nilson, Biedermann and Leveby. The second harmonic is produced by moving a mirror (dotted line) to the corresponding incidence angle.

(b) Interferometer configuration with two identical gratings proposed by Hershey, Chen, and Leith. The first grating G_1 splits the incident wavefront into the various orders, corresponding to the Fourier components, which are then recombined by the second grating G_2 on the substrate or observation plane.

An incoming collimated beam of light hits the first grating where it is diffracted. The resulting propagating orders illuminate then the second grating where they are diffracted again. Some of these rays then recombine on the observation plane (which is also the substrate) producing the various Fourier components. The spacings between both gratings and between the second grating and the substrate must be approximately the same. The resulting superposition is then an emulation of the Fourier series. Depending on the grating configurations, different kinds of emulations can be chosen. Various configurations for controlling phase and amplitude of the components were investigated. Again, sawtooth profiles using two Fourier components were successfully demonstrated.

More recently, in 2002, Freschi, dos Santos, Rigon and Cescato [Freschi 2002] proposed a novel approach to adjust the Fourier components relatively to each other. Using an interferometer with two arms and movable mirrors, they took advantage of the fact that the photoresist's refractive index changes during illumination. After having made a first exposure (the first Fourier component), which acts as reference grating, it is then possible to adjust phase and harmonic number of the higher Fourier components by observing the interference fringes made up by the diffracted beams coming from the exposed reference grating and the following illuminations. They achieved to produce sawtooth profiles with the first two Fourier components.

In summary, as far as we know from the literature only the first two Fourier components could be successfully produced. The novelty of the setup that we will describe in the next subsection resides in the fact that it allows to produce more then two Fourier components. For the time being, structures have been fabricated using nine Fourier components.

3.2.1. Loyd's mirror geometry

The basic idea, from which that setup was derived, came first from Humphrey Lloyd during the early part of the 19th century. Like in Young's experiment, it is a wave splitting device used to demonstrate light interference with an incoherent light source.

Lloyd's mirror interferometer consists in a flat piece of either dielectric or metal that serves as a mirror. An incident spherical wavefront coming from a slit illuminates a screen and the mirror with grazing incidence. Interference fringes occurring by the superposition of the light hitting the screen directly and its reflection by the mirror can then be observed on the screen. Humphrey Lloyd published an article about the demonstration in the Proceedings of the Royal Irish Academy of Science in 1837. In Loyd's experiment, the mirror and the observation plane are mounted statically on a table. The working principle of our setup is to rotate the mirror and the observation (or recording) plane both together as shown in Fig. 3.3. Sample holder and mirror are mounted together, forming a very compact and mechanically stable unit, which is screwed on a rotation stage. Note that compared to other interferometers, a single rotation stage is needed to change the incidence angle of the interfering beams and therefore the grating period Λ. A wide range of incidence angles can be obtained with an error given by the precision of the rotation stage (less than 0.001°).

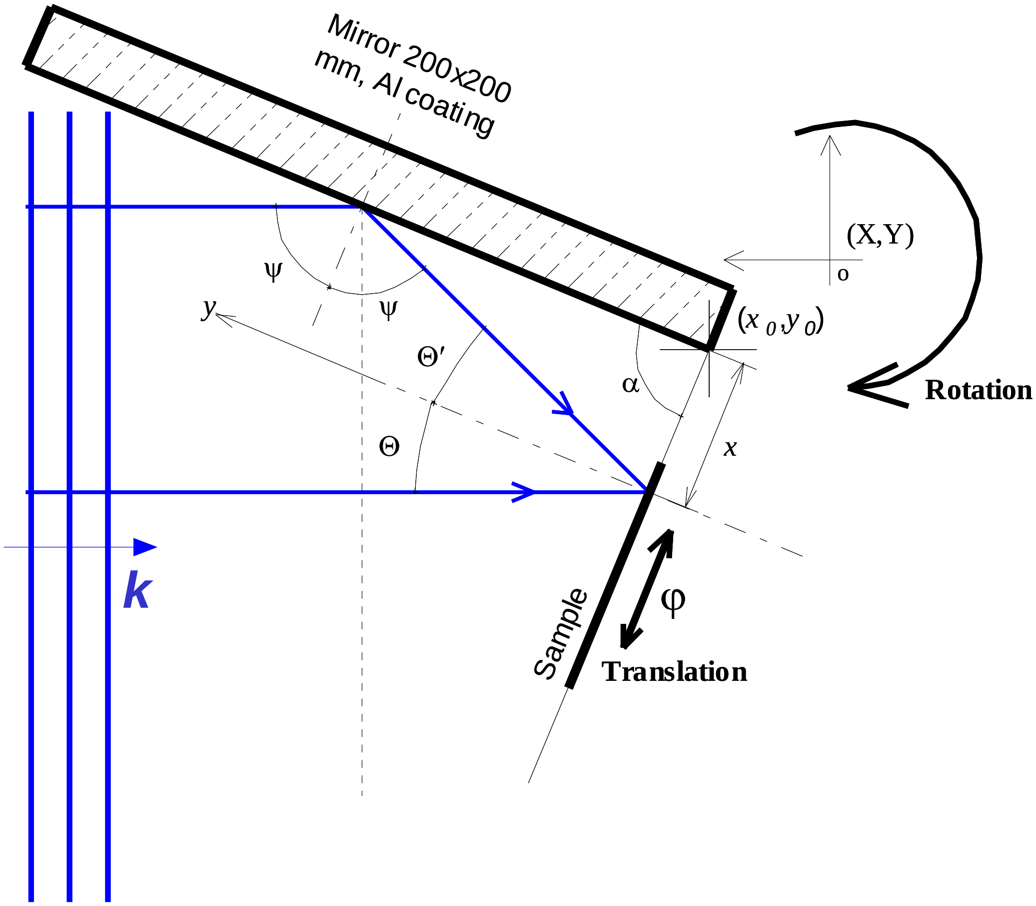

Figure 3.3. Schematic of the optical setup, which allows multiple exposures with, controlled phaseshift. The sample (and therefore recording plane) and mirror are rigidly mounted at ideally $\alpha = 90°$ and lie on a rotation table centered on (X,Y). The mirror surface and the recording plane crosses at (x_0, y_0). The sample and its holder are mounted on a linear piezo translation stage to produce the desired phaseshift φ of the Fourier component.

Since the light beam used to create the interference pattern pass mainly through the same space (and elements), the system is not sensitive to disturbances (like vibrations, or air turbulences). Compared to the setups described in Fig. 3.2 (a) and (b), our setup covers a larger range of incidence angles, and is less subject to external disturbances.

The optical path difference *OPD* = $\delta_1 - \delta_2$, see Fig. 3.4, between the directly incoming beam and the reflected beam can be written as a function of the position x along the sample, the angle between sample and mirror α, and the angular position Θ of the system which is also the angle of incidence of the direct incoming beam. The distances δ_1 and δ_2 are defined as the segments CB and DB, respectively. By considering the triangle ABC, as defined in Fig. 3.4, we can apply the sinus rule that gives the relation $x/\sin\gamma = \delta_1/\sin\alpha$, and by considering triangle BDC, write $\delta_1 = \delta_2 \cdot \cos(\Theta + \Theta')$.

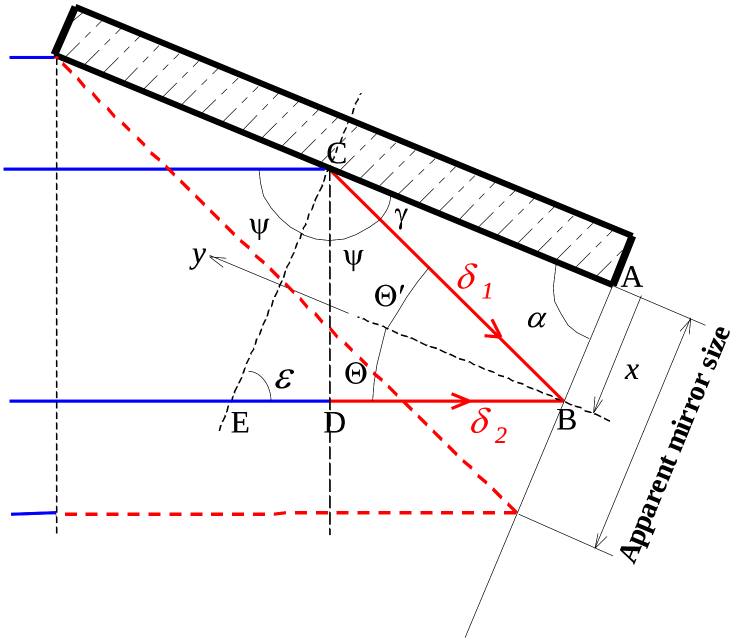

Figure 3.4. Schematic of the optical setup showing how the different points and angles are defined to obtain the *OPD* between the direct incoming and the reflected beam, function of x, α and Θ.

Moreover, considering triangle BEC and ABC, we can notice the following useful relations between angles $\varepsilon = \psi = \alpha + \Theta$, $\Theta + \Theta' = 2\varepsilon$, and $\gamma + \psi = \pi/2$.

With further simple mathematical development, we can obtain for the optical path difference (in air)

$$OPD = -2 \cdot \cos\left(\alpha + \Theta\right) \cdot \sin(\alpha) \cdot x \qquad (3.1)$$

If the angle α between the sample and the mirror is exactly 90°, the directly incoming beam and the beam reflected from the mirror hit the sample symmetrically with the same incidence angle (thus $\Theta' = \Theta$) for any angular position of the rotation stage. The optical path difference becomes than *OPD* = $2 \cdot \sin(\Theta) \cdot x$. Incidence angle and grating period are in relation by $\sin(\Theta) = \lambda / 2\Lambda$, and therefore the optical path difference can also be written as $OPD = (\lambda / \Lambda) \cdot x$, λ being the light wavelength and Λ being the grating period.

The fact that the mirror and the sample are rigidly mounted together ensures that the optical path difference is zero at the cross point (x_0, y_0) of the mirror plane and the sample plane and this for every position Θ of the rotation stage, and therefore grating period Λ. In other words, the *OPD* is linear in the *x*-axis and zero for $x = 0$ as can be seen in Eq. (3.1). Therefore we have a reference point where the phase is determined for each exposed pattern period. This is a very important property since we do not need to include any system that tracks the phase position during the rotation of the stage.

Due to mechanical errors, the intersection point (x_0, y_0) of the mirror-sample unit and rotation point of the system (X_o, Y_o), as defined in Fig.3.3, cannot be exactly aligned and therefore the intersection point slightly moves during rotation of the mirror-sample unit. But as long as the incoming wavefront can be considered as a plane wave, the relative position of each of these points is not of importance. In other words, both points don't have to coincide exactly.

To insert an arbitrary phase shift for each exposure, it is necessary to change the optical path difference between the two interfering beams. This step can be achieved by either changing the path length of the light or by changing the refractive index of the medium.

In our case, we decided to change the path length of the light beams by a translation of the sample along an axis in the recording plane. In our case, it is the *x*-axis as shown in Fig. 3.3. Note that this translation is parallel to the interference fringes vector. Note also that for $\alpha = 90°$, the *OPD* is not sensitive to displacements along the *y*-axis, as defined in Fig. 3.4. The triangle BEC is just translated and therefore the side's length remains constant and so does the *OPD*. Thus the translation of the sample can occur with an angle relatively to the *x*-axis as long as the angle α between sample surface and mirror remains constant.

To generate the phase shift for any pattern period, we need a translation stage that allows to displace the pattern by at least one period (of the largest period), with a very high accuracy of a few percent of the smallest pattern period, i.e. of the order of a few nm. To increase the sensitivity of the system, the translation stage can be mounted with an angle relative to the *x*-axis as long as α is constant, therefore the sample surface have to remain perpendicular to the mirror during translation as explained previously. In our case, the linear stage was mounted at 45°, increasing the sensitivity along the *x*-axis by a factor $1/\sqrt{2}$.

Although every periodic function can be decomposed into a Fourier series, which consists of an infinite amount of sine or/and cosine terms, we can only produce a finite amount of these harmonic components.

Due to the geometry of our setup, we can produce frequencies of the Fourier components that range from 1/210 x 10^6 l/mm (or a period of 210 nm) to 1/8.26 x 10^3 l/mm (or a period of 8.26 μm). These frequencies are the upper limit given by the used wavelength of λ = 413 nm and the lower limit given by the apparent size of the mirror, see Fig. 3.4, for an incidence angle of 1.43°, respectively. For growing incidence angle ψ on the mirror, the apparent surface of the mirror is shrinking and so does the illuminated surface on the sample. The lower limit corresponds to an illuminated area on the sample of arbitrary chosen 5 mm width, the mirror size being 200mm x 200mm. In other words, the range of periods the setup can produce goes from a little more then half the laser's wavelength $\lambda/2$, in our case about 210nm (corresponding to an incidence angle Θ of 80°) to a few μm depending on the area of the needed structured surface. On the other side, we can generate any phase of every Fourier component that lies in that range.

Therefore, by truncating the Fourier components that lies outside of the usable frequency range of our setup, we obtain an approximation of the desired profile. How good this approximated profile will become depends strongly on the shape of the desired function. Generally, functions with a continuous profile can be approximated very well since the amplitude of the higher harmonics decreases quickly.

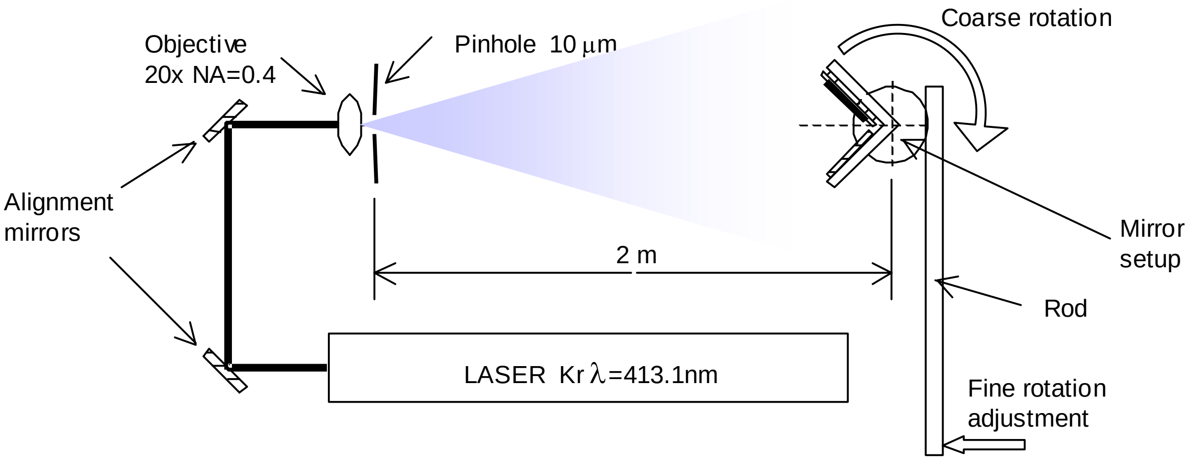

Figure 3.5. Schematic of the illumination system and the optical setup. It consists in a single spherical wave issued from a microscope objective and spatial filter. Steering mirrors are used to align the Kr laser. Note that to increase the precision, a fine rotation stage is coupled to the coarse 360° rotation table. The rod (approximately 1.2 m in the experiment) serves for the fine rotation adjustment by de-magnifying a linear actuator.

The incoming illumination, as shown in Fig. 3.5 consists in a spherical wave coming from a focused and filtered beam. The spatial filter, a pinhole in this case, is placed far enough, about 2 meters, from the setup, so that the spherical wave can be considered plane (the radius of curvature being about 2m) for samples of a few square centimeters.

To summarize, the component's frequency is obtained by changing the incidence angle of the beams (which is done by the rotation stage), and the phase is adjusted by changing the sample's relative position with respect to the interference pattern.

3.2.2. Adjusting the harmonic's number

If the various harmonics are not exactly integer multiples, the structure profile changes with the lateral distance. In other words, the structure profile distorts more and more with each period. Thus, it is very important that the harmonics (which are integers) are accurate to obtain a structure with the desired periodicity along the sample. The size of the obtained structured areas depends on the absolute accuracy, which the rotation stage can provide. To increase the accuracy, two rotation stages are mounted together, one for the coarse movements (0 to 90°, with a precision of 10^{-3} degrees), and the other for the fine adjustment (10^{-4} to 10^{-6} degrees), as can be seen on the schematic of Fig. 3.5 and on the pictures of Fig. 3.6. The fine adjustment rotation table consists of a manual rotation table with an approximately 1.2 meters long rod mounted radial to it. The rod de-magnifies the movement of a linear actuator located at the other end of the rod, thus providing the necessary angular resolution (see coherence length of the structured area as defined in section 2.2.2). For example, for a linear displacement of 1μm, the relative angle changes by about 10^{-5} degrees. Standard optical rotation tables don't achieve such precisions. The experimental exposure system can be seen on the pictures of Fig. 3.6 (a) and (b).

To adjust the harmonics, a reference grating is mounted on the sample holder next to the sample, like represented schematically in Fig. 3.7 (a), or on the pictures of the experimental setup in Fig. 3.6 (a) and (b).

This ensures that the reference grating and the sample move together. Each incoming beam, the directly incident and the reflected, creates a set of beams after having been diffracted by the reference grating. The adjustment of the incidence angle is done by observing the interference fringes, which occur when both sets of diffracted beams superpose, as shown in Fig. 3.7 (b).

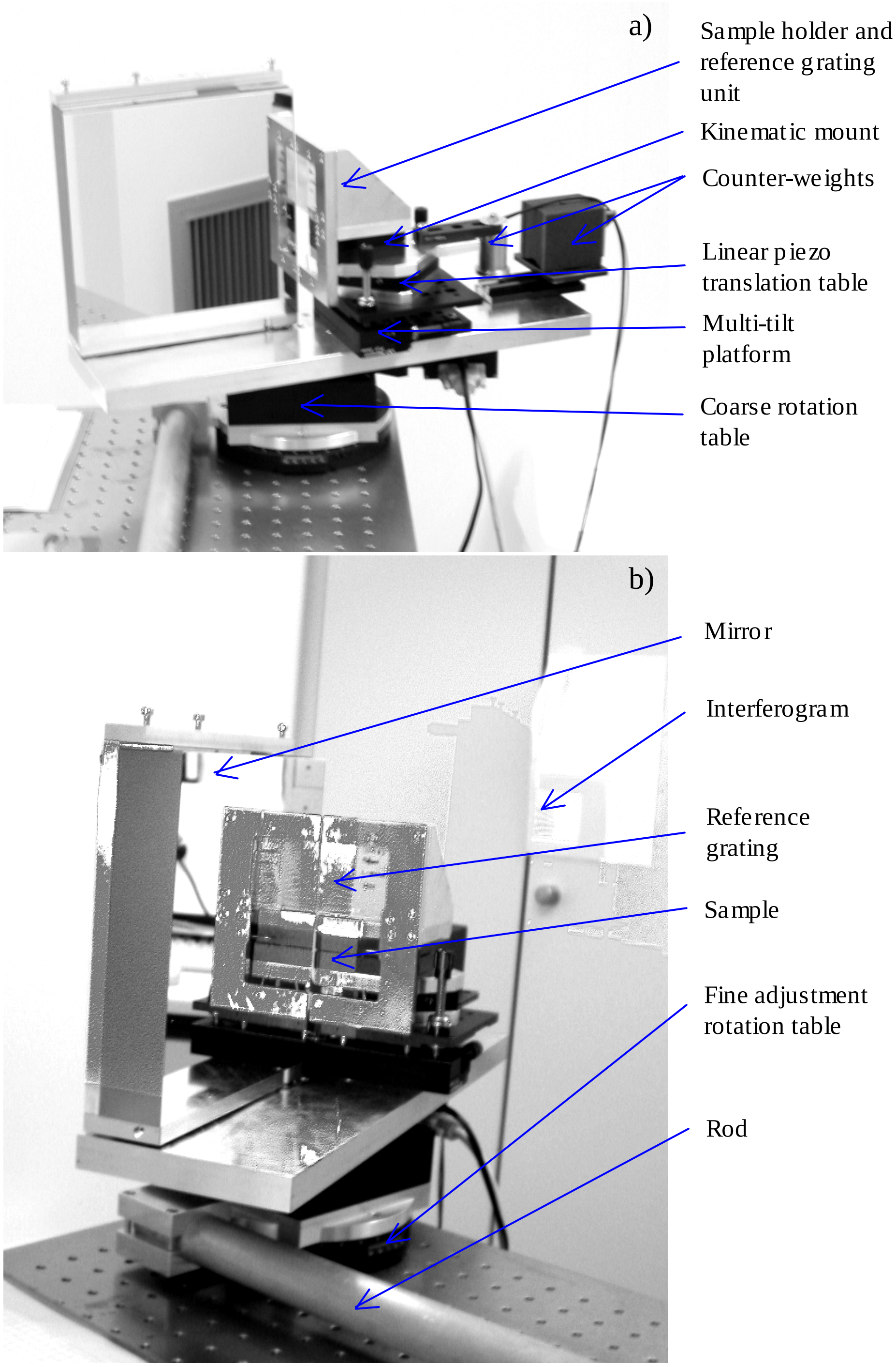

Figure 3.6. Experimental setup to superpose Fourier components. The setup uses a reference grating for the adjustment of the harmonic numbers. A linear piezo-stage allows to control the phaseshift of each Fourier component. The sample holder unit, which holds both a reference grating for the adjustment of the harmonic number and the sample to be exposed, is mounted on a multi-tilt platform to precisely

align the setup. A kinematic mount is used to mount or unmount the sample holder unit in order to install the sample. Counterweights are placed at different locations to adjust the various mass centers of the setup around the critical components like the piezo-table and the computer controlled rotation stage.

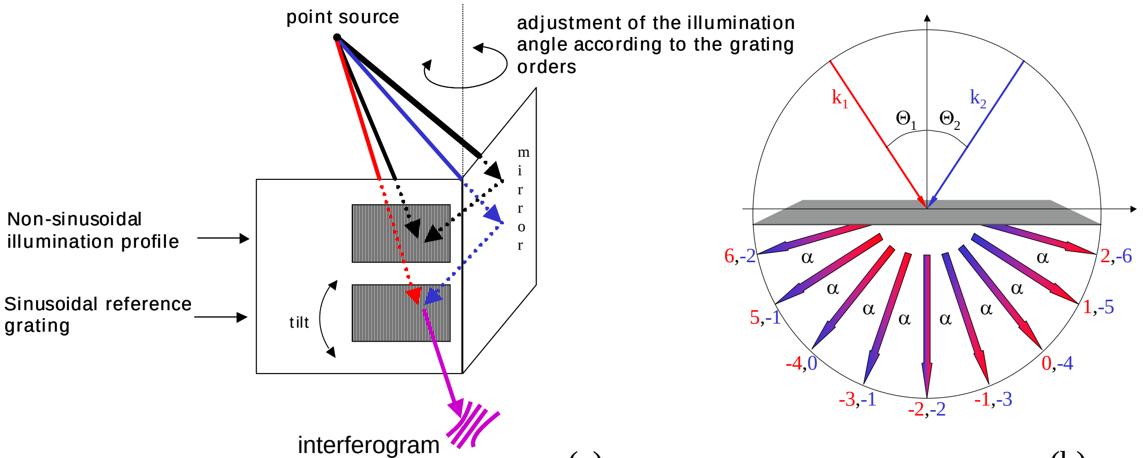

(a) (b)

Figure 3.7. (a) Geometry of the system with reference grating. The reference grating, which can be slightly tilted, is rigidly mounted with the sample to expose. The interferogram picture (schematically represented) corresponds to the 0,-4 orders superimposition as defined in (b).

(b) Schematic of the superimposition between the sets of diffracted orders coming from the directly incoming beam $\mathbf{k_1}$ and the reflected beam $\mathbf{k_2}$. The situation is represented for an angle of the system set to expose the 4th harmonic. The grooves of the reference grating are perpendicular to the plane of incidence therefore the plane constituted by the incident beams $\mathbf{k_1}$ and $\mathbf{k_2}$.

If the plane of incidence (that is constituted by the incoming beams) is perpendicular to the grooves of the grating, the resulting interference figure consists in straight fringes. The spacing between fringes goes towards infinity when the diffracted orders are perfectly aligned. For a positioning error of 0.001 degrees and 0.0001 the fringes size is approximately 2 cm and 20 cm, respectively.

The size of the interferogram picture corresponds to the area of the reference grating, i.e. typically a few square centimeters. Determining the optimal position of the setup becomes very difficult because the fringes become larger as the system reaches the optimal position. In other words, the fringes become much larger than the interferogram picture dimensions, and therefore the contrast of the picture, which is essential for detection, decreases. Moreover, if the system is looped on a photo-detector or a CCD device, for example, that analyses the interferogram, the size of the detector puts even more constraints on the fringes period, as the detection area is even smaller. Typically, such devices have an active area of a few square millimeters. An optical system should help to reduce the interference figure to fit on the detectors active area. However, in that case, the contrast over the interferogram determines the resolution of the detection.

To allow better fringe detection, the interferogram picture and therefore the geometry of the interfering beams has to be changed. By tilting the reference grating by an angle φ, a constant vertical component is induced along the y direction to the wavevectors of the diffracted orders, as shown in Fig. 3.8 (a) and (b). Consequently, the wave vector $\boldsymbol{\Delta k}$ of the interference pattern resulting from the mixing of the diffracted orders of the incoming beams $\boldsymbol{k}_{i1}$ and $\boldsymbol{k}_{i2}$ has itself a constant component along the y axis.

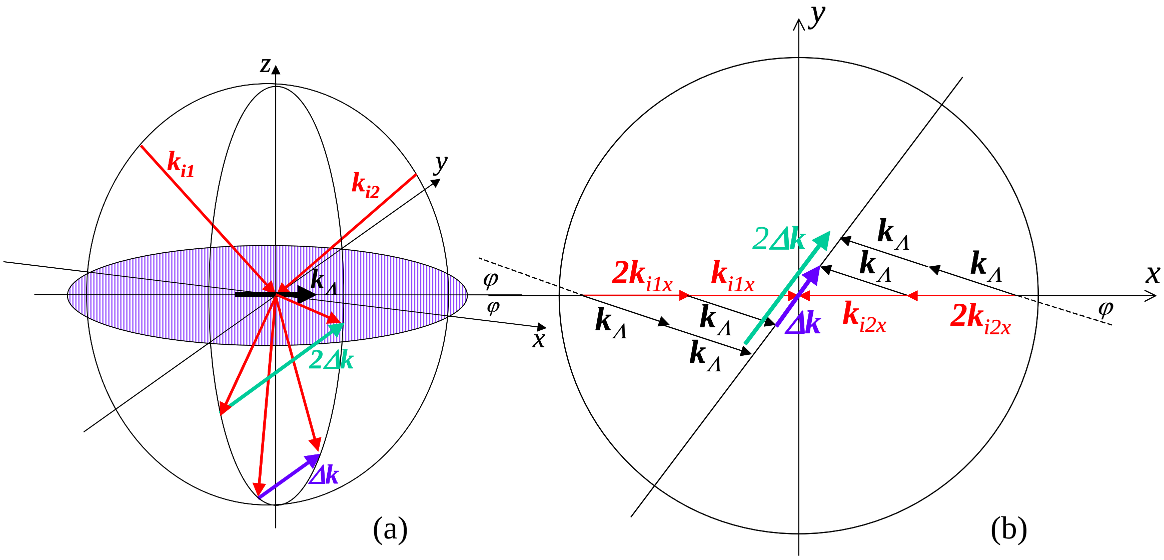

Figure 3.8. (a) Three-dimensional vector representation of the incoming and diffracted beams, as well as the resulting interferogram's wavevector. For sake of representation, we have chosen a symmetric case where the –1 and –2 orders of both incoming beam interfere. $\boldsymbol{k}_{i1}$ and $\boldsymbol{k}_{i2}$ are the incoming vectors. $\boldsymbol{\Delta k}$ and $2\boldsymbol{\Delta k}$ are the wavevectors of the interference pattern resulting from the vectorial difference of the 1st order, respectively 2nd order diffracted beams.

(b) Projection of the k-vectors on the x-y plane.

Now, the resulting interference pattern consists still of straight stripes, but its periodicity and orientation changes with the incidence angle of the incoming beams. When the positioning error is high, the stripes are almost vertical and very narrow; therefore $\boldsymbol{\Delta k}$ is almost parallel to x. As the system reaches the optimal position the interference fringes become more and more horizontal, and therefore $\boldsymbol{\Delta k}$ is almost parallel to y. Note that at the optimal position, the stripes are largest, and therefore $\boldsymbol{\Delta k}$ is smallest. The size of the stripes can be adjusted by setting the tilt angle of the grating. The stripes period decreases as the tilt angle augments.

The higher harmonics, 2, 3, ... , n , can then be adjusted by looking at the mixing of the order $-n$ of both incoming beams. When the angle of the system is precisely adjusted to expose a harmonic n, the projection on the x-y plane of the incoming beams $\boldsymbol{k_{i1x}}$ and $\boldsymbol{k_{i2x}}$ corresponds exactly to a multiple n of the main period, and thus the orientation of the interference stripes remains the same for all harmonics. In other words, the triangle defined by $\boldsymbol{k_{i1x}}$, $\boldsymbol{k_{\Lambda}}$ and the angle φ is expanded by n when the angle is set for a harmonic and thus the corresponding interferogram vectors $n\boldsymbol{\Delta k}$ are on a same line. Although the orientation remains identical, the vector length becomes $n\boldsymbol{\Delta k}$, and thus the period of the fringes is divided by n. For example, in Fig. 3.8 (b), the projection of the incoming vectors $\boldsymbol{k_{i1x}}$ and $\boldsymbol{k_{i2x}}$ and its multiple $2\boldsymbol{k_{i1x}}$ and $2\boldsymbol{k_{i2x}}$ correspond to the first, respectively to the second harmonic. As can be seen, the corresponding interferogram wavevectors $\boldsymbol{\Delta k}$ and $2\boldsymbol{\Delta k}$ are parallel but differs in length by a factor 2.

Note that the orientation of the fringes doesn’t have to be necessarily horizontal. However, once the orientation of the fringes has been set, this orientation has to remain the same for every harmonic to expose.

In our experiment, we used the interference patterns produced by the superimposition of the 0^{th} order of the directly incoming beam and the diffracted orders of the reflected beam. We look at the superimposition with the -1, -2, ...,$-n$ order for each corresponding Fourier component to expose. The basic idea is equivalent to that described in Fig. 3.8, but that configuration is more advantageous from a mechanical viewpoint mainly because the interferogram remains at the same location for each angular position. Therefore, the detector can be mounted rigidly at a fixed place. Although the principle remains exactly the same, the vector situation differs slightly. Figure 3.9 shows a schematic of the situation as it was used in the experiment, and the coordinate system for the numerical calculations. In the chosen coordinate system, the point source lies in a plane (defined by the x-z axis) perpendicular to the mirror and the reference grating. For the numerical calculations of the interferograms, we defined a reference-grating window whose upper edge lies in the x-z plane as defined before and whose side edge is merged with the rotation axis y of the setup. A tilt in the reference grating means that only the grating lines are tilted, the window remaining as defined.

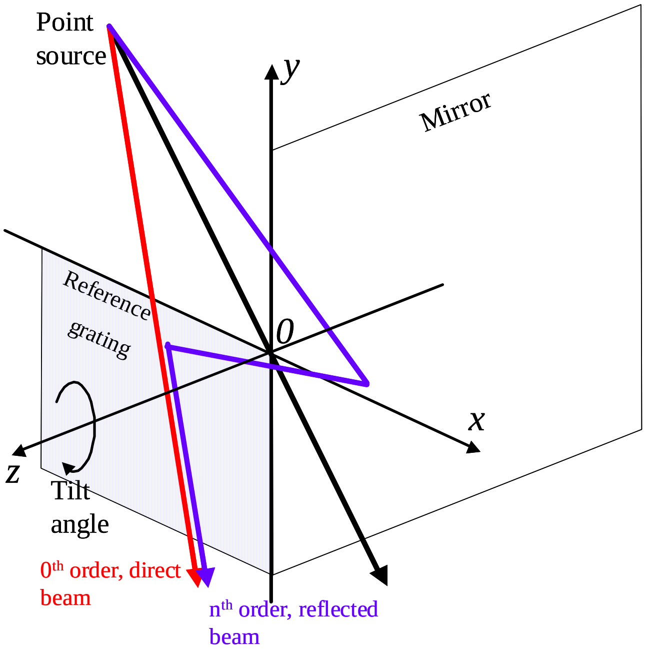

Figure 3.9. Schematic of the recording configuration. The interference patterns used to adjust the harmonic gratings result from the superimposition of the directly (in bright) and the diffracted *n*-th order (in dark) of the reflected part of the incoming spherical wave. The reference grating lines are tilted around the *z*-axis.

Equation (3.2), also called “grating equation”, was then used to determine locally the diffraction behavior of the incoming waves.

$$\sin(\Theta_{out}) = \sin(\Theta_{in}) + \frac{m}{\Lambda} \tag{3.2}$$

Figures 3.10 and 3.11, show simulations of interference patterns obtained in the cases where the diffracted orders 0 and 1, 0 and 2 and 0 and 6 respectively interfere together. The simulations are done for spherical waves with a radius of curvature of 2 meters corresponding to the distance between the pinhole of the illumination optics, see Fig. 3.5, and the reference grating. For sake of representation, the calculations are done with beams misaligned by 0.002°.

Two cases are considered. In the first case, we assume an ideal grating (IG), where the grating lines are perfectly straight and uniform. In the second case, the calculations are done for a self-originated grating (SOG), as it was the case in the experiment. Self-originated means that the reference grating is produced by the same waves than those used to generate the interferograms. More explicitly, in the calculations, we take into account the slight change in the local period and orientation of the lines of a reference SOG.

In Fig. 3.10, we look also at the influence of the tilt angle of the reference grating on the interferograms. First, a bending of the interference fringes is observed. Due to the chosen viewing window, the bending, practically non-existent at positions near the origin (because the incoming beams are almost symmetric) increases in curvature when getting away of the origin. Furthermore, the bending becomes stronger for higher order mixing. Two effects can be observed:

-The angles of incidence are larger with increasing order number and therefore the waves hit the grating more obliquely.

- Furthermore, the *OPD* between both beams augments, and therefore the radius of curvature difference between both incoming waves increases.

This behavior is less pronounced for SOG than for IG, because the curvatures of the incoming waves are partly compensated by the grating's locally changing grating vector. The grating acts as a replayed hologram.

With a tilt on the reference grating, the bending effect is less pronounced, in particular with the self-originated gratings (SOG), as can be seen in Fig. 3.11. If we consider the first two millimeters along both axis of the interferogram (a square window located at the origin), the fringes can be considered straight, in particular in the case where the reference grating is tilted. This area is sufficient for an electronic device to analyze the orientation of the stripes. At the time being, the adjustment of the fringes where done using a sheet of crosshatched paper. In that case, the error on the rotation angle was approximately 0.001°, and we were therefore able to fabricate structures with constant profile over 1-2 mm for a structure period of about 2 μm.

Using a twin photodiode device to determine the orientation of the interference fringes seems a promising solution to enhance the precision on the rotation angle. One has then just to measure the values given by each of the photodiodes. When they match exactly the fringes are parallel. As the distance between photodiodes is only a few microns, the needed interferogram size is very small, a few tenth of microns, ensuring that the fringes are near perfectly straight over the detection area. Note that these improvements have not been investigated at the time being.

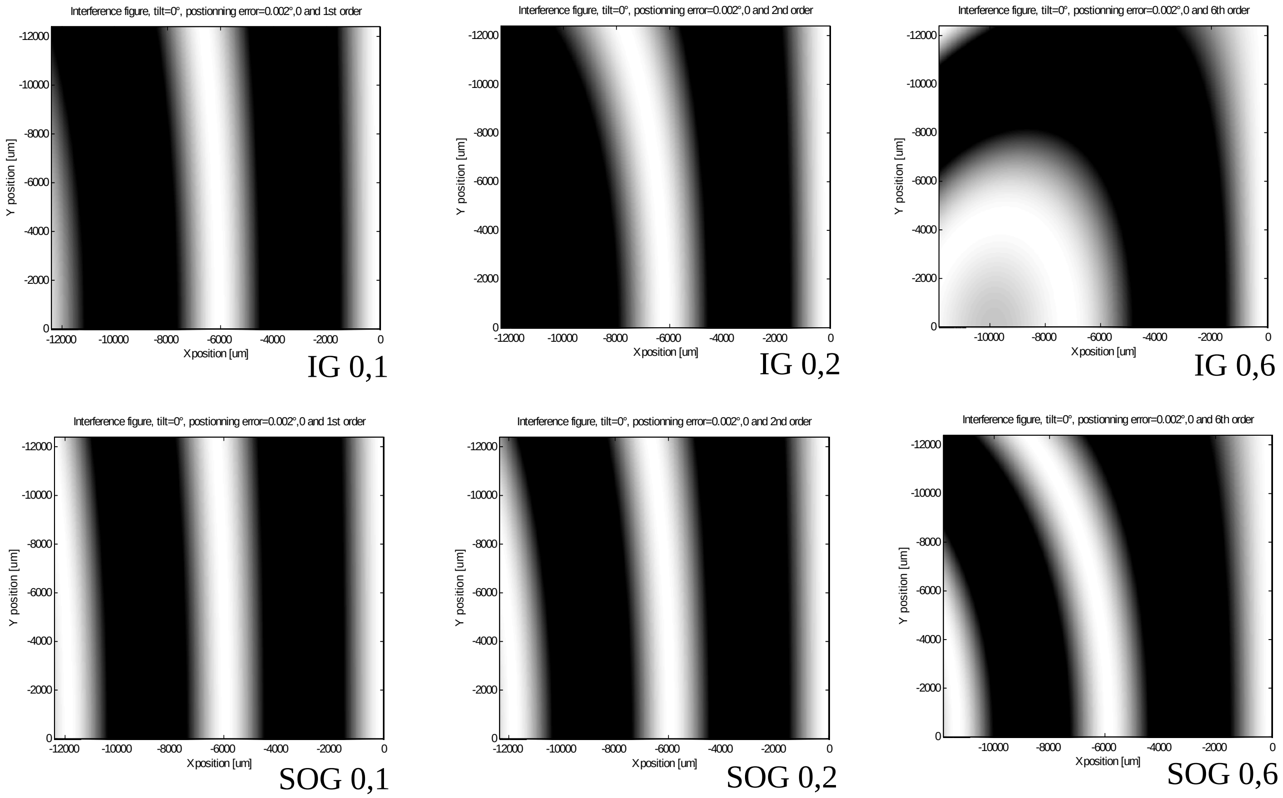

IG 0,1 IG 0,2 IG 0,6

SOG 0,1 SOG 0,2 SOG 0,6

Figure 3.10. Calculated interference figures using a square reference window of 12 by 12 millimeters in the coordinate axis system defined in Fig. 3.9. The table is divided in columns showing intensity pictures for the superimposition of the direct incoming beam (0-th order) and respectively the 1^{st}, 2^{nd}, and 6^{th} diffracted order of the reflected beam from left to right. Calculations are done for an ideal reference grating (IG) and for a self-originated grating (SOG), in the upper and lower row, respectively.

As is expected, the spacing between fringes diminishes with higher order interference. To determine the optimal position, minimizing the fringe spacing could have been a detection algorithm too.

Figure 3.12 shows pictures of the interferogram produced by the experimental setup. The reference grating has a period of 2.2 μm, and a size of approximately 2 cm by 5 cm. The size of the grating and the interferogram is approximately identical. In the background, one can distinguish the sheet of paper with its crosshatching used to align the interferogram patterns of the harmonics. The tilt angle was adjusted in order to be easily distinguishable by the naked eye for the whole range of harmonics to be exposed.

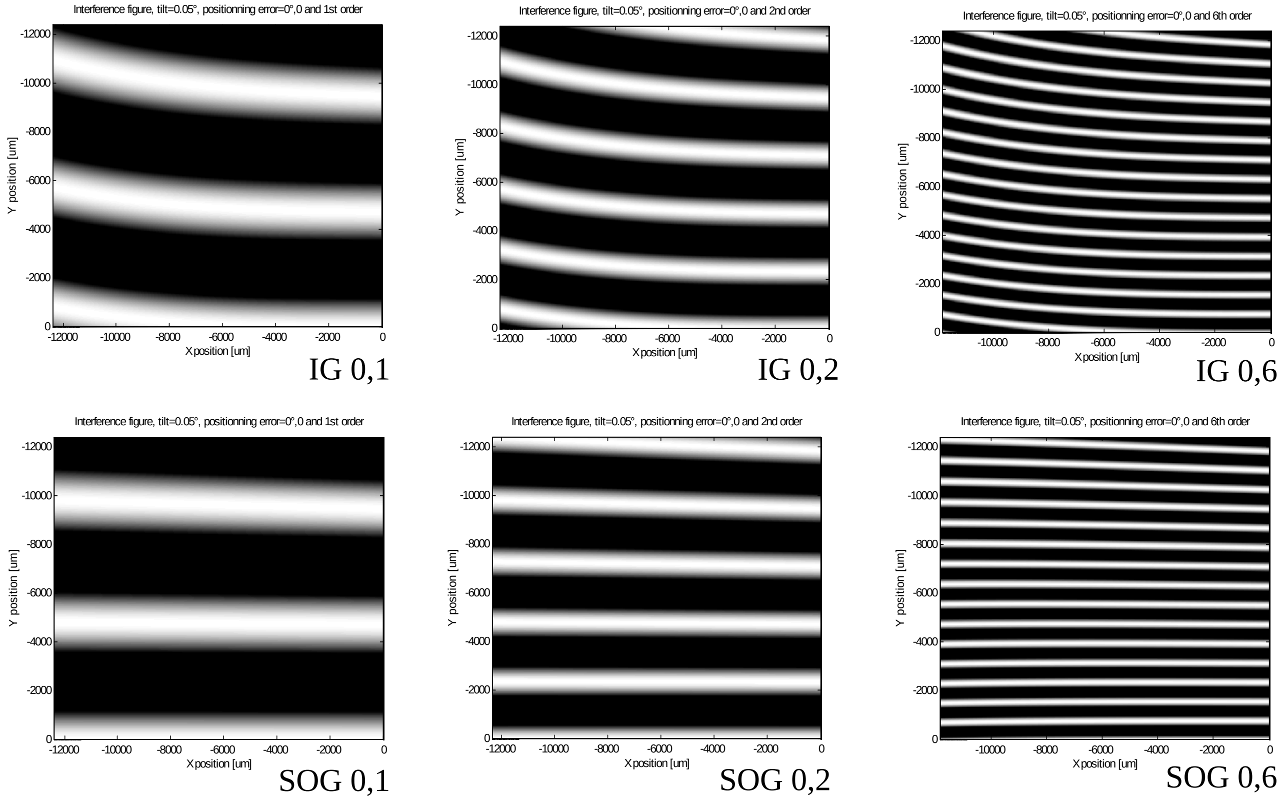

IG 0,1 IG 0,2 IG 0,6

SOG 0,1 SOG 0,2 SOG 0,6

Figure 3.11. Calculated interference figures using a square reference window of 12 by 12 millimeters in the coordinate axis system defined in Fig. 3.9. The table is divided in columns showing intensity pictures for the superimposition of the direct incoming beam (0-th order) and respectively the 1st, 2nd, and 6th diffracted order of the reflected beam from left to right. Calculations are done for an ideal reference grating (IG) and for a self-originated grating (SOG), in the upper and lower row, respectively. The calculation parameters are exactly identical as in Fig. 3.10, except that the reference gratings are tilted by 0.05°.

Typically, ten harmonics were exposed. The tilt angle, which could not be precisely measured in our setup, can be estimated between 0.01 to 0.05°. The interference figures and calculation show good agreement, as can be seen by comparing Fig. 3.11 with Fig. 3.12. One can observe how the fringe spacing linearly diminishes with higher order superimposition as well as the bending of the fringes predicted by the numerical calculations.

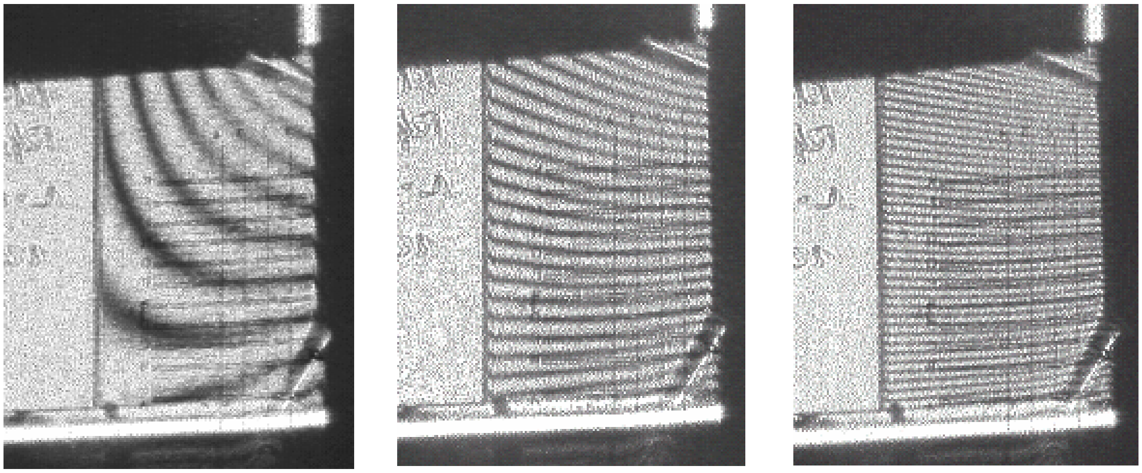

0,1 orders superimposition 0,2 orders superimposition 0,3 orders superimposition

Figure 3.12. Pictures of the interferograms used to synchronize the various harmonics in the experiment. From left to right the mixing of the direct incoming beam with the 1^{st}, 2^{nd}, and 3^{rd} diffracted order of the reflected wave are shown. The reference grating is a self-originated grating in resist with a period of 2.2µm. The edge at the right side corresponds to the mirror-sample intersection, or the *y*-axis, and the bottom edge at the *x*-axis, as defined in Fig. 3.9.

3.3. Prism setup

A way to reduce the grating period $\Lambda = \lambda /2n_{med}\cdot\sin\Theta_i$ is to increase the refractive index n_{med} of the incident medium. Θ_i is the angle of incidence, and λ is the recording light wavelength. Therefore, we let the interferences occur in a right-angled glass prism mounted in the configuration shown in Fig. 3.13. Literature about interference recording in dense media is extensive [Nassenstein 1969, Bryngdahl 1969, Stetson 1967, Sainov 2000]. The refractive index increases from 1 (air) to 1.528 (BK7 glass at λ = 413 nm) and the minimum feature size is reduced in proportion. In air the theoretical limit for the grating period, therefore Θ_i = 90°, is $\lambda/2$ = 206.5 nm for a wavelength of λ = 413 nm. With the prism, the theoretical limit goes down to $\lambda/2n_{BK7}$ = 135.1nm.

One of the short sides of the prism is coated with aluminum and acts therefore as a mirror, the other short side being kept uncoated. The hypotenuse is coated with an antireflection coating for the 413nm wavelength. The sample, coated with a layer of photoresist, is index-matched by its bare side on the uncoated side of the prism, as can be seen on the enlarged view in the bottom of Fig. 3.13. The whole ensemble, prism and sample, is mounted on a rotation stage.

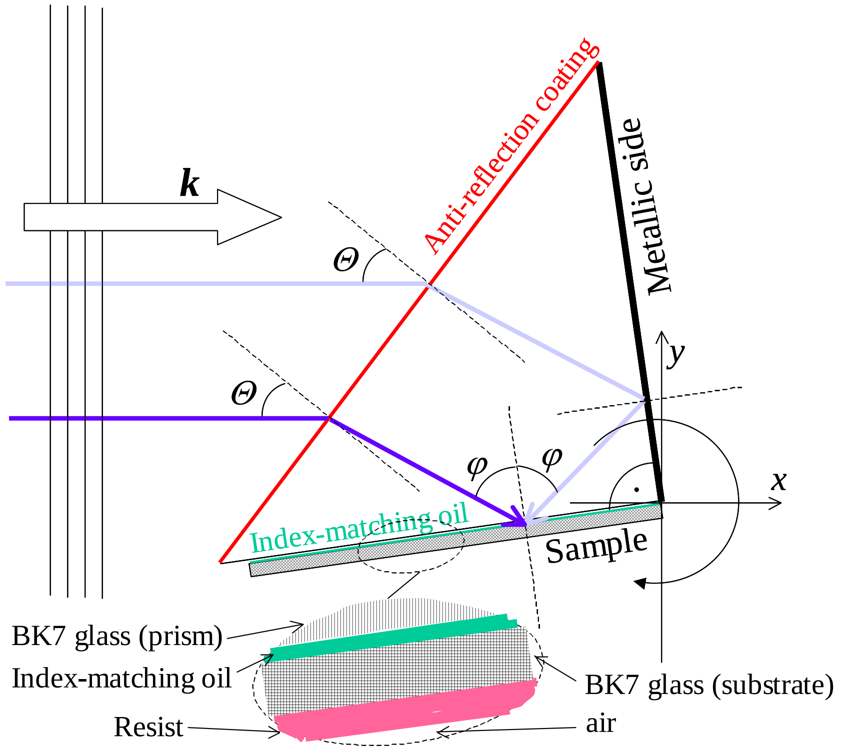

Figure 3.13. Schematic of the prism setup recording geometry. The right-angled prism has one of its short sides (the thick black line) coated with aluminum to act as a mirror. The hypotenuse is coated with an anti-reflection layer at λ = 413 nm to suppress back reflections coming from inside the prism. The prism can rotate around its right-angle corner.

The rotation point is centered on the right-angle corner of the prism. In this configuration, the incident light, which consists of a plane wave of laser light, hits the hypotenuse of the prism and after being refracted at the air-glass interface, is split in two parts. The first part hits the sample directly, and the second part hits the sample after being reflected on the mirror side of the prism. Since the prism is right-angled, both parts hit the sample symmetrically.

The refractive index difference between oil n_{oil} = 1.51 and glass n_{BK7} = 1.528 is approximately 0.02. Reflections at that interface are low ($R<10^{-6}$). Thus they can be neglected. Note that the prism and the sample are made of the same glass.

Due to the setup configuration, the interferences between both parts of the plane wave in the photoresist layer occur under total internal reflection (TIR) condition (the incident medium being more dense), as far as the incidence angle is larger than the critical angle, in that case φ_c=36.5°. That means that the incident beams are entirely reflected at the interface. As a consequence, the resulting interference pattern is much more complicated than the interference of two laser beams. The interference pattern is produced by the two incoming plane waves and their reflection at the resist-air interface. The diagram, in Fig. 3.14, shows the situation of the wave vectors interfering in the photoresist layer.

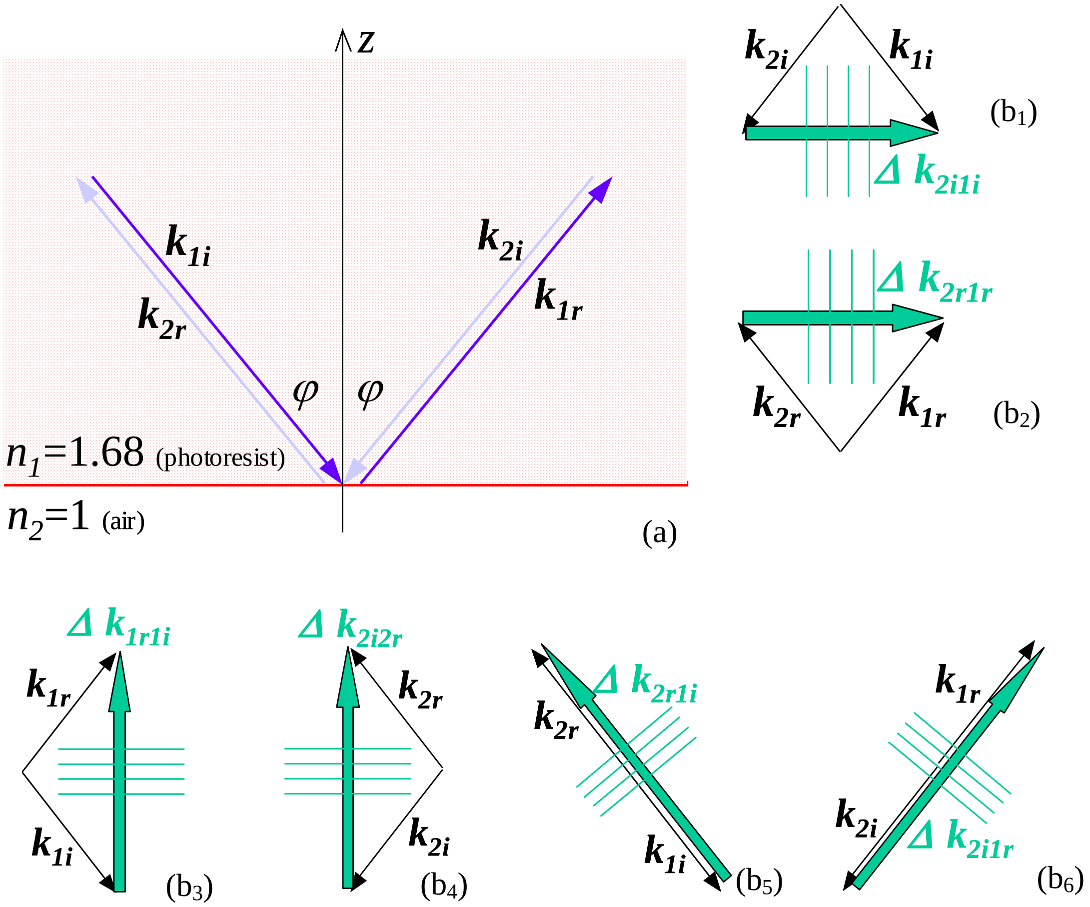

Figure 3.14. Situation of the interfering beams in the photoresist layer. As can be seen in (a), four beams of light interfere together producing a complex interference pattern. The small diagrams (b$_1$) to (b$_6$) show separately the various gratings produced by the four interfering beams. The resulting interference pattern consists of the superposition of all interference gratings.

The interference pattern in the photoresist layer can be decomposed in the superposition of six gratings produced by the mutual interference of the four beams, as represented in Fig. 3.14. (b$_1$) to (b$_6$). Thanks to the symmetry of the configuration, both incident beams $\boldsymbol{k}_{1i}$ and $\boldsymbol{k}_{2i}$ hit the sample under the same angle. Their reflections $\boldsymbol{k}_{1r}$ and $\boldsymbol{k}_{2r}$ are both symmetric as well. The total internal reflection condition implies that the reflected beams undergo a different phase change for each polarization in relation with the incident beams and that the amplitude of the reflected beams remains the same as the incoming ones.

The situations shown in Fig. 3.14 (b$_1$) and (b$_2$) are equivalent, due to the symmetry, and its underlying gratings, related to $\boldsymbol{\Delta k_{2i1i}}$ and $\boldsymbol{\Delta k_{2r1r}}$, respectively, superpose in a constructive manner. The orientation of the gratings groove is perpendicular to the interface and its period diminishes as the incidence angle grows.

Situations (b$_3$) and (b$_4$), involve the incident beams $\boldsymbol{k_{1i}}$, $\boldsymbol{k_{2i}}$ and its respective reflections $\boldsymbol{k_{1r}}$, $\boldsymbol{k_{2r}}$. The gratings produced by those two situations, related to $\boldsymbol{\Delta k_{1r1i}}$ and $\boldsymbol{\Delta k_{2i2r}}$, respectively, superpose also constructively due to the symmetry of the configuration. The orientation of those gratings is parallel to the interface and results in the illumination of layers parallel to the interface. These layers will than be washed away during the development process, thus reducing the range of potential heights of the final structures to the distance of two of these layers in the most favorable case. As the spacing of these illuminated layers increases, the larger the incidence angle, the higher the final structures can be.

The last two situations, represented in Fig. 3.14 (b$_5$) and (b$_6$), involve $\boldsymbol{k_{1i}}$, $\boldsymbol{k_{2r}}$ and $\boldsymbol{k_{2i}}$, $\boldsymbol{k_{1r}}$ respectively. The orientation of those gratings, related to $\boldsymbol{\Delta k_{2r1i}}$ and $\boldsymbol{\Delta k_{2i1r}}$, change with the incidence angle. The larger the angle, the more parallel to the interface the vector will be. On the other hand, their periods remain equal. These gratings cross each other periodically, creating periodic nodes where both intensities add up to reach the maximum intensity. The potential height of the final structures will be limited to the distance in the z direction of two next nodes. The larger the incidence angle, the larger the spacing between two next nodes will be and the higher the final structures can be.

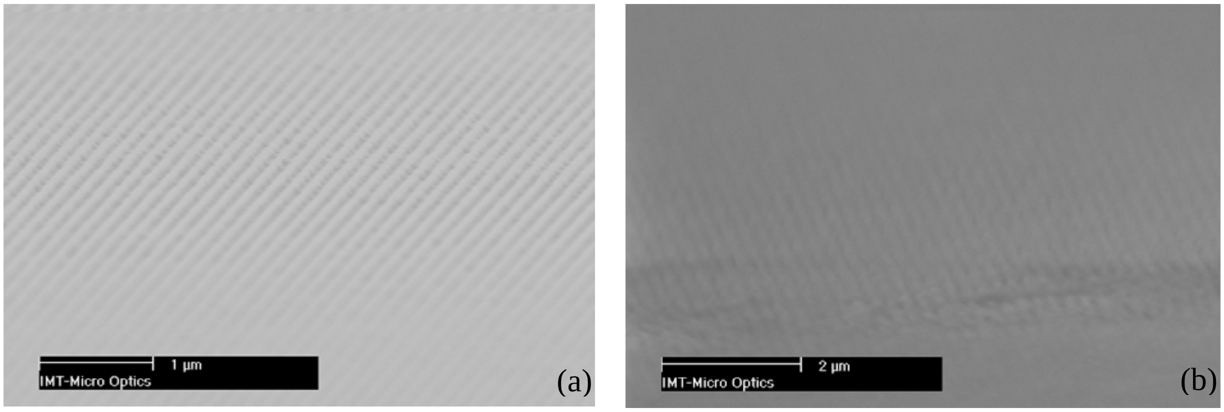

Figure 3.15. SEM pictures of photoresist gratings. The grating in (a) has a period of approximately 160nm and a depth of 20nm and the grating in (b) a period of approximately 170nm and a depth of 20nm.

As one can see, the illuminated pattern is very complex with multiple superposed gratings in many different directions. Therefore, the realization of periodic structures with this setup is very difficult and thus time consuming. Great care is needed, for the final structure not to be washed away by the development process. Therefore the exposure energy and development times have to be carefully adjusted.

Figure 3.15 (a) and (b) shows SEM pictures of two realization of periodic structures produced with that setup. The gratings have been produced with a tilt angle Θ, see Fig. 3.13 of approximately 22° for a period of 160 nm and approximately 13.5° for a period of 170 nm. The polarization of the incoming light was TE. The incoming illumination consisted of a spherical wave produced by a microscope objective and spatially filtered using a pinhole. The pinhole is placed at a distance, of 1.8m in that case. Therefore the spherical wave can be considered plane when it reaches the sample. The produced gratings are very shallow but can however be used in combination with other techniques to improve the depth of the final structures.

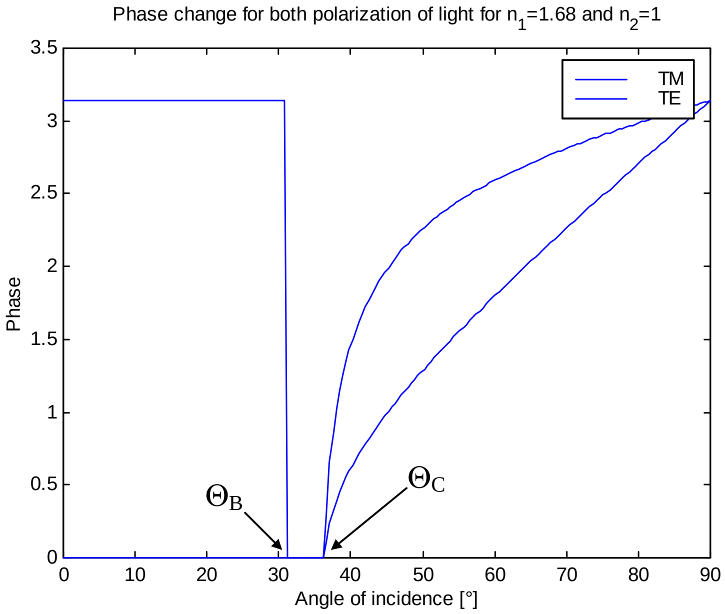

Figure 3.16. Illustration of the phase change for TE and TM light under TIR conditions with the incidence angle. As a result the polarization state of the reflected light is changed in relation with the incoming light. Note that at approximately Θ_B=32° incidence the TM light is entirely transmitted. It is called the Brewster angle. From approximately Θ_C = 36°, also called the critical angle, and upwards the light is reflected under TIR.

To increase the height of the structures in photoresist, the gratings described in Fig. 3.14 (b_3) to (b_6), have to be suppressed or at least their contrast has to be minimized with regard to the contrast of the gratings described in (b_1) and (b_2). That contrast can be reduced by using the fact that at the air-photoresist interface, the total internal reflection condition changes the polarization state of the reflected beam in relation with the incoming one as illustrated in Fig. 3.16.

A possible improvement should be to optimize the polarization state of the incoming illumination by calculations. The goal is to minimize the contrast of the gratings (b_3) to (b_6) which involve in all cases the directly incoming beam and its TIR beam. Remark that the gratings (b_1) and (b_2) are not influenced, (b_1) involving both incoming beams $\boldsymbol{k_{1i}}$ and $\boldsymbol{k_{2i}}$ and (b_2) involving both TIR beams $\boldsymbol{k_{1r}}$ and $\boldsymbol{k_{2r}}$. Note that due to the symmetry, $\boldsymbol{k_{1r}}$ and $\boldsymbol{k_{2r}}$ have the same state of polarization, and therefore have maximum contrast. At the time being, we did not investigate it any further.

3.4. Multiple beam interference setup

The interference of two laser beams results in a periodic intensity distribution with a sinusoidal profile. By combining several exposures with different interference patterns it is possible to obtain complex structures with a great degree of freedom. Thus it is possible to realize profile shapes other then sinusoidal ones [Leith 1984 and 1985, Cowan 1984, Hobbs 1999].

To enhance the complexity of the structures, we consider two cases. In the first case (section 3.2) the idea was to enhance the number of different exposures with sinusoidal intensity distribution. The focus with that setup was to obtain arbitrary one-dimensional periodic structures. A limited range of two-dimensional structures, as explained in section 3.2, was also feasible by rotating the square sample by 90°. In the second case, that is the object of this section, the idea is to enhance the number of interfering beams at once on the sample. Depending on the orientation of the beams and/or the number of exposures the structures can be one- as well as two-dimensional.

As shown in Fig. 3.17, the working principle of this setup is to use mirrors (up to four) in order to generate the light beams, which will interfere to produce various interference patterns. Each mirror can be tilted independently from the sample along a single axis, like described in Fig. 3.17 (a). This can be either parallel to the normal of the sample or parallel to the sample's edges. By changing the mechanical parts of the mirror holders, which are screwed on the setup's head, as shown in Fig. 3.18, it is possible to choose the orientation of the rotation axis of each mirror separately like described previously. A rotation stage allows the mirrors to rotate together along the horizontal axis defined in Fig. 3.17 (a). Moreover, the sample can be rotated around its normal axis, the horizontal rotation axis, independently of the mirrors. Furthermore, the whole setup can be rotated along the vertical rotation axis, like defined in the diagram of Fig. 3.17 (a), adding an extra degree of freedom to the system.

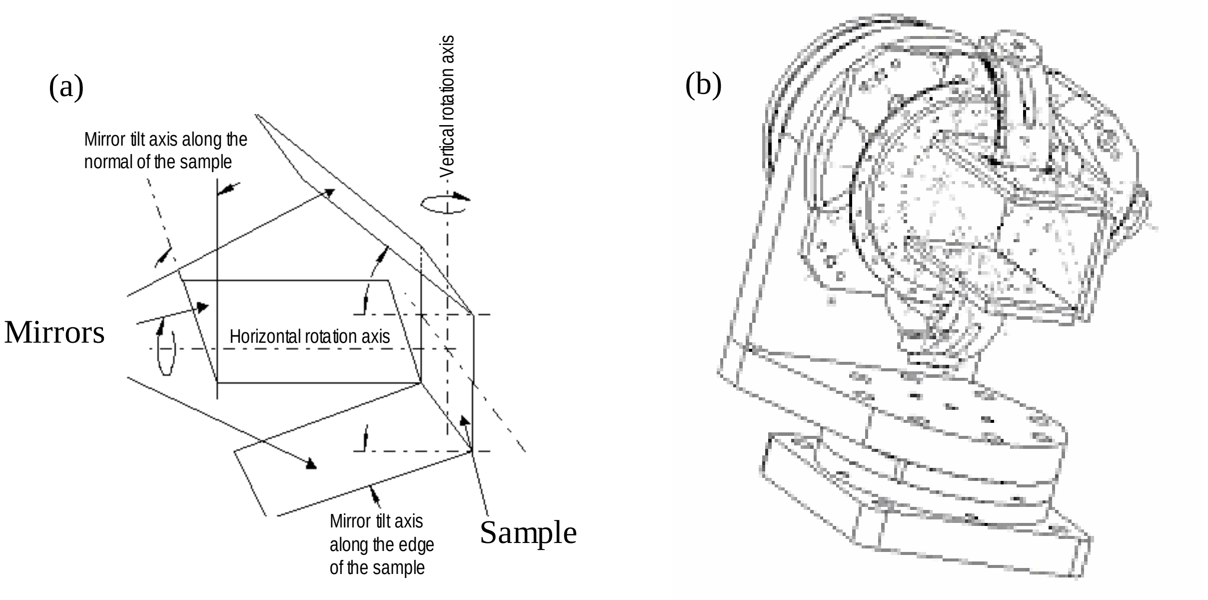

Figure 3.17. Multiple beam exposure setup. The represented configuration has two mirrors that can be tilted along the side edges (the top and bottom edge of the sample) and one mirror that can be tilted along an axis, which is normal to the recording plane (surface of the sample) and located on a corner of the sample.
(a) Block diagram of the freedom degrees.
(b) Technical drawing of the setup.

The incoming light consists of a spherical wave issued from a microscope objective and pinhole. Since the setup is far enough from the pinhole, the incoming wave can be considered sufficiently plane and homogenous over the area where the structures are recorded.

The light hitting the sample directly and its reflections on the mirrors produce altogether the interference pattern.

As we explained in section 2.2.2, if various exposures have to be synchronized, the precision of the period as well as orientation of patterns must be high enough to suppress beating effects. Note that the coherence length of a periodic structure is about 1.5 mm for an angular precision of 10^{-3} degrees. Thus, to realize arbitrary periodic structures, the various degrees of freedom of the system need to have angular precisions in the order of

10^{-3} degrees to obtain well-defined structured areas over 1.5 millimeters length or 2.25 square millimeters surface for two-dimensional structures.

Including this feature would have raised the mechanical complexity of the setup to an unacceptable level. For that reason, the setup has been used foremost to realize structures with moiré effects, as described in section 2.2.3, as well as hexagonal structures.

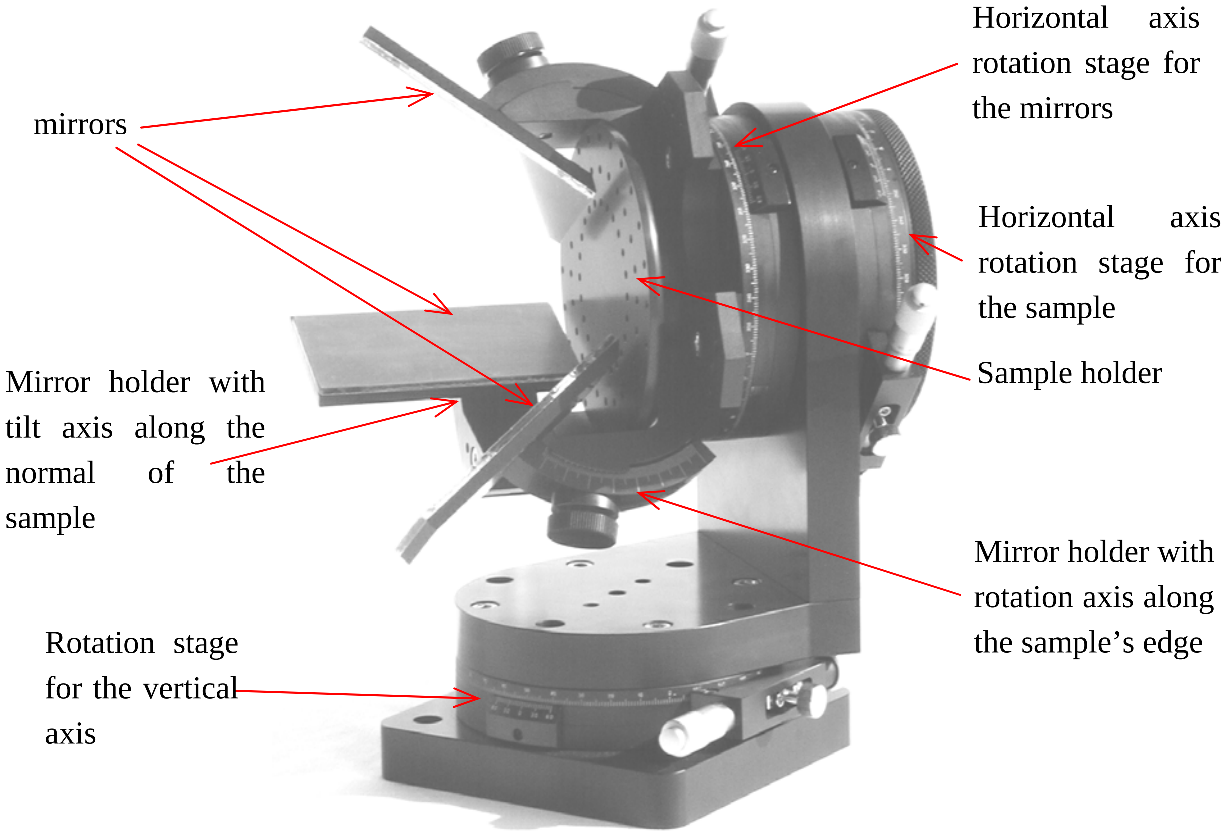

Figure 3.18. Picture of the multiple beam exposure setup. The system is in a configuration like shown in the diagram of Fig. 3.17 (a), for sake of comprehension. The different parts are described on the picture. Although conceived for square samples, the sample holder can support samples of any shape. The recording area is a square of 50 by 50 mm.

However, the concept of the setup has shown that the stability of the mechanical construction allows to obtain feature sizes of about 220nm, for a laser wavelength of 413nm, without any fringe locking device.

Figure 3.19 shows some examples of potential structures that can be realized with such a setup. The numerical simulations show only a few periods of the illuminated intensity pattern. The amplitude of all interfering beams is equal.

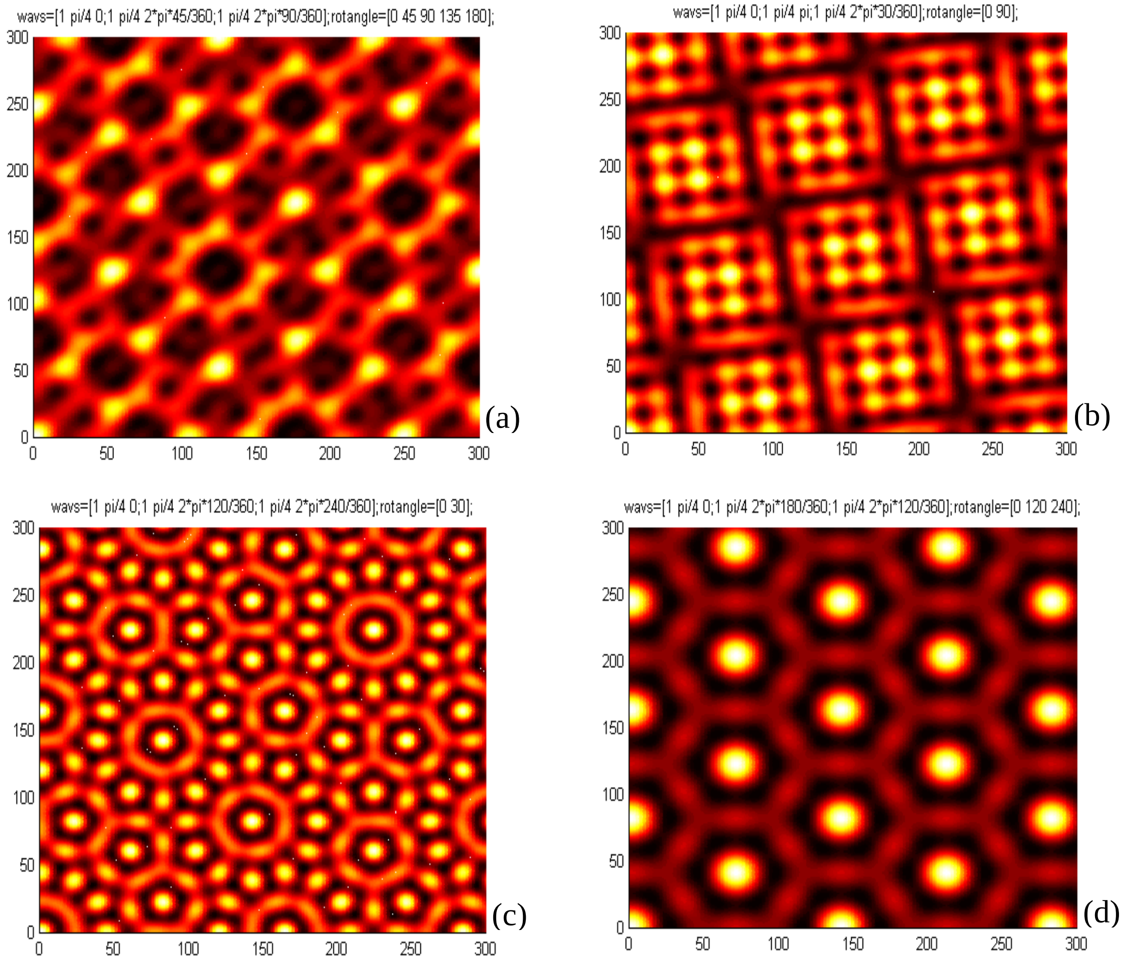

Figure 3.19. Numerical simulations of possible structures that could be potentially realized by the multiple-beam exposure setup.

The term *wavs* = [$beam_1$; ... ; $beam_i$] in the title of the various examples (a) to (d), contains the orientation of the *i* planar waves $beam_i$= [A_i, ϕ_i, θ_i] that interfere together at the same time. The planar waves are described by their amplitude *A*, their polar angle ϕ (angle with the vertical or normal to the sample surface) and their azimuthal angle θ (angle in the horizontal plane or surface of the sample). With that configuration, *j* superpositions with different azimuthal angles Θ_j (contained in *rotangle*=[Θ_1 ... Θ_j]) are made. The scales of the axis as well as the intensity are in arbitrary units, the darker areas being the bottom of the structures and the white spots being the tips.

Experimentally, the position of each beam would be given by the angular positions of the mirror holders and the horizontal axis rotation stage for the mirrors, as well as the vertical axis rotation stage.

Those positions being kept constant, the sample would be rotated independently along the horizontal axis between exposures. For example, (a) would involve three interfering beams, therefore two mirrors, and five different exposures at the angles 0, 45, 90, 135 and 180 degrees. The exposure time would be the same for all exposures.

3.5. Summary

In this chapter, we have presented optical setups for two-beam as well as multiple beam interference lithography. A simple and easy to set up configuration, like the two-point source configuration, as well as a more sophisticated configuration with controlled phaseshift were described. The last of these allows to realize structures with periodic arbitrary profiles using the Fourier synthesis, introduced in section 2.2. Some of the realized structures were originated using 10 Fourier components. Moreover, we have shown how to experimentally adjust the incidence angle of the beams with a precision of 10^{-3} degrees. With a little more investigations, this value could be further reduced and we have suggested a way to achieve that experimentally.

A setup for multiple beam interference has also been investigated. Although the concept has lots of potential, due to the mechanical difficulties being inhere in the steering of the beams, we focused on the realization of moiré-like structures, described in section 2.2.3.

Nevertheless, these advanced setups let us reach feature sizes down to about 110nm, which is near to the theoretical limit of 103.5nm, in air and for a 413nm laser wavelength.

To reduce the minimum feature size even more, we have presented an optical setup that is based on a right-angled prism. As we let the interferences occur in optically dense media, with a refractive index of 1.528, the theoretical limit is 69nm feature size at 413nm wavelength. Gratings with 80nm feature size were realized using that setup.

CHAPTER 4

PHOTORESIST AS A RECORDING MATERIAL

Thin relief phase holograms offer certain advantages that have attracted the interest of the industry as well as of research labs. In the form of surface relief gratings in air, the refractive index difference is high, since air fills the voids [Moharam 1984, Bartolini 1974]. Therefore, they can be used as very efficient optical diffraction elements. Moreover, after being transferred into metal or some other convenient material, they are very well suited as masters for replication in mass production processes, like embossing [Gale 1997].

The preferred material for recording these holograms is a light sensitive organic material called photoresist. The intensity pattern of the exposure is transferred in the thickness of the photoresist during the development process, by a change in dissolution rate of the more or less exposed areas and it results therefore a surface relief profile into the photoresist [Dill 1975, Narasimham 1977, Huang 1989, Mack 1987 and 1992]. There exist two types of them. The negative type photoresist, where the more exposed areas become less soluble, and the positive one, where the more exposed areas become more soluble. In that section, we will focus on the later type, and in particular the diazonapthochinone (DNQ) based photoresists. Indeed, due to their widespread use and sensitivity in the visible spectrum of light, we opted for that kind of photoresists for the realization of the structures.

Such resists are made up of three major components: a base resin (a novolack), giving the resist its structural properties, a photoactive compound (PAC), in our case the DNQ, and a solvent. Although, a prebake step intended to dry of solvents is done before exposure, thermal studies [Koyler 1979, Shaw 1977] have shown that there can remain up to 10% solvent in the resist layer.

The final obtained surface-relief profiles resulting from interference lithography are not a linear response of the illuminated intensity pattern. It depends on many parameters such as the used laser wavelength, exposed intensity pattern, developer, as well as the different priming steps, like spinning or baking, before exposure. In the following subsections we will review the different steps involved in the processing of the resist, and the most critical one in particular, the development.

4.1 Preparation of the samples

In this subsection, we will describe further the different steps in the processing of the resist before exposure.

The substrate should be in materials that have very low absorption at 413nm, so that there is practically no thermal dilation during exposure. Moreover, the refractive index of those materials should be very close to the refractive index of the resist (n=1.68-1.72), so that no parasitic back-reflections occur at the resist-substrate interface. For our purposes, we have chosen substrates of glass or quartz, in square or circular shape. With a refractive index of about 1.5 and very low absorption coefficient, they are well suited for our applications.

First, the substrates lie in a convection oven at 200°C for at least 2 hours to completely dehydrate the substrate. Note that the following steps must be done rapidly so that the substrate does not have time to re-absorb humidity in the meanwhile. After cooling down to room temperature, they are then treated with silane gas for better adhesion of the resist coating.

The resist, which comes in liquid form, can then be deposited onto the substrate, by spraying, pouring, or spinning. The spinning method, where a drop of resist is poured on the spinning substrate, is the most suited for our applications as it ensures that the coating is homogenous and perfectly plane. Moreover, the height of the coating can easily be controlled by the rotation speed of the spinning stage. The attained resist thickness represents the equilibrium between centrifugal force and solvent evaporation (both increasing with spin speed). Depending on the chemical composition of the resist, notably the contained quantity of solvents, it can be more or less viscous. Note that great care has to be taken with the handling of the bottles of resist. The atmospheric conditions, temperature and humidity affect the properties of the resist. The bottles have to remain closed whenever it is possible so that the incorporated solvent evaporates as less as possible. With little viscous resists and high spinning rates (up to 6000 rnd/min), resist layers of less than 300nm can easily be deposited with, for example, AZ1518 with a solvent to resist ratio of 2:1 and spinning rate of 3500 rnd/min. However, great care has to be taken in the priming steps to allow perfect and homogenous adhesion of the resist layer. On the other hand, very viscous resists, and low rotation speeds (less than 3000 rnd/min) result in layers as thick as 150μm. The homogeneity and flatness of such layers is very critical. The spinning requires to be slowly ramped up to the final speed.

The plates rest 15 to 30 minutes on a plane surface, depending on the resist height, so that the tensions and inhomogeneities in the resist layer disappear.

For our applications, we used S1818 from Shipley, AZ1518 and AZ4562 from Clariant in combination with the developer AZ351B from Clariant, an NaOH based standard developer for positive resists. The resists were more or less diluted with a standard diluter depending on the final resist layer thickness that is needed by the application.

4.2 Baking and exposure

After deposition, the resist layer must be dried off of its solvents. But baking can also cause numerous unintended outcomes, like for example the decomposition of the light sensitive component. All aspects of baking can probably affect the dissolution properties of the resist. It remains one of the most complicated and less understood steps in the lithographic process.

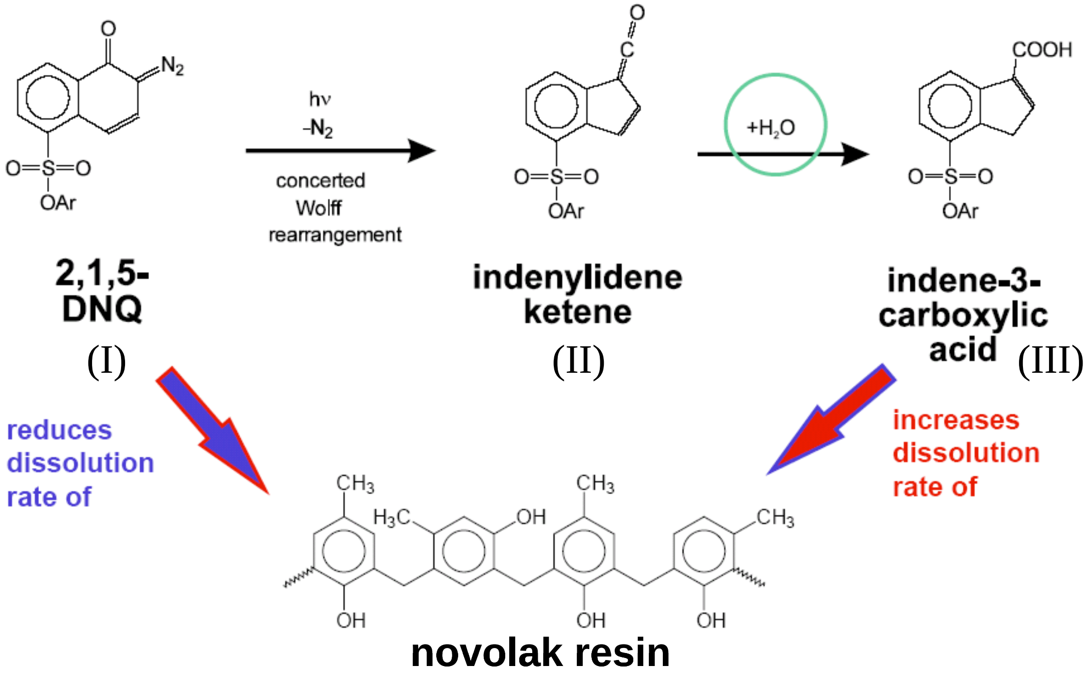

Figure 4.1. Schematic of the chemical reactions into a DNQ resist under radiation. The photoactive compound DNQ sulfonate (I) separates a N_2 molecule (II), and converts into indene carboxylic acid requiring an H_2O molecule. Picture taken from "*Trends in Thick Resist for Solder Bumping –Negative and Positive Resists Compared*", Clariant AZ Electronic Materials.

When heated to temperatures above 70°C, the photoactive compound (PAC) of a diazo-type positive resist begins to decompose to a non-photosensitive product. Figure 4.1

shows a schematic of the different chemical reactions occurring in the resist under UV radiation. The initial reaction mechanism is thought to be identical to that of the PAC reaction during UV exposure [Dill 1977, Shaw 1977, Koyler 1979, Johnson 1984], resulting in the formation of carboxylic acid (see Fig. 4.1 (III)), which is very soluble in developer. The dissolution rate in a developer of carboxylic acid is several orders of magnitude higher compared to unexposed DNQ-sulfonate. As a consequence, the overall development rate increases. Note that this chemical reaction needs water. A second chemical reaction, which occurs without the need of water, is the estherification of the ketene within the resist, as shown in Fig.4.1 (II). The ester, on the other hand, is very difficult to dissolve in aqueous solutions and thus retards the dissolution process.

It results in a change in the chemical makeup of the resist. The most important of the affected parameters are, the optical parameters (like the absorption coefficient), the diffusion parameters, and last the development parameters such as the dissolution rates of non-exposed resist and totally exposed resist.

The main reasons to perform a prebake, or softbake, are to prevent popping or foaming of the resist by the N_2 produced during exposure and improve adhesion of the resist on the substrate. It avoids also mask contamination and/or sticking with the mask in contact-mask lithography. The bake parameters such as time and temperature as well as bake method (hotplate or convection oven) are a compromise between maximized solvent reduction and minimized PAC loss. Note that the layer thickness after spinning shrinks more or less, usually by 25%, depending on the bake parameters.

For interferometric lithography with thin resist layers (less than 5μm), bake parameters of 50 minutes at 50°C in a convection oven, for example, work very well for total exposure doses of about 150 mJ/cm^2 with AZ1518 or S1818. As the PAC loss is minimal, the resist is kept very sensitive, and on the other hands adhesion as well as foaming problems are minimal or non-existent.

For thicker layers (between 5μm and 10μm), bake parameters ramped up in three levels of 40°C, 50°C, and 60°C during 1 hour each work well for total exposure doses of 250 mJ/cm^2 with AZ4562.

As can be seen in Fig. 4.1, the resist needs water in order that the chemical reactions involved in the exposure process occur. Thus, the samples have to rest long enough at room temperature and humidity so that the resist layer completely rehydrates before exposure. For films in the range of 1μm thickness a few minutes suffice, but for thicker films of about 20μm, one to two hours are necessary. The concentration of water in the resist determines the efficiency of the chemical reaction DNQ-sulfonate to carboxylic acid, and thus the sensitivity of the resist to exposure dose.

The kinetics of the exposure of resist is principally tied to the phenomenon of adsorption. On a macroscopic level, the chemical reactions, described in Fig. 4.1 and explained higher, modify the local dissolution rate of the resist depending on the local exposure dose. Because radiation modifies the chemical composition of the resist, the absorption coefficient changes during the illumination. The layer becomes more and more transparent to light with increasing exposure dose. This so-called bleaching of the resist reinforce the UV exposure as the exposed resist acts as light channels in mask lithography, or as self-illuminated hologram in interference lithography. In that last case, the sequence, if several exposures are made, may have an importance as the gratings exposed previously diffract the light and can lead to unexpected structures once developed. The optimal order of the sequence, each grating having a different period and exposure dose, depends on the desired structure. But in general, it is recommended to begin with the grating that requires the weakest exposure energy and to end with the strongest exposure energy to minimize light channeling effects into the exposed resist.

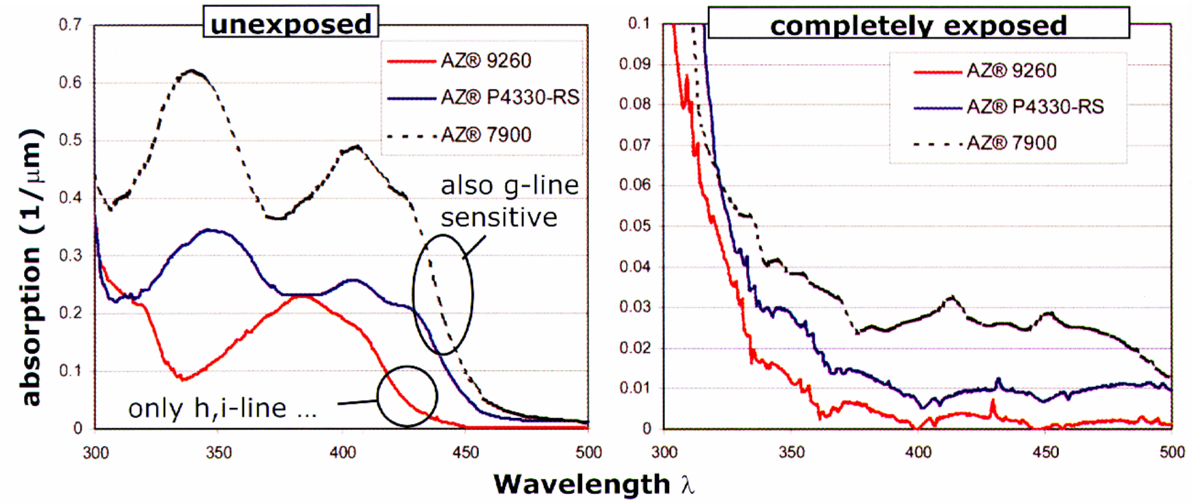

Figure 4.2. Bleaching of three different resists. The absorption coefficient decreases dramatically when the resist layer is fully exposed. Note that the absorption coefficient of AZ9260 decreases almost to zero once exposed. Therefore, high contrasts, in other words final structures with high aspect ratios (period to structure height), can be expected with such a resist. The pictures are taken from "*Lithography Processes*", MicroChemicals Gmbh.

Figure 4.2 shows how the absorption is affected by the light exposure for different resists. Note that the N_2 molecules produced by the photolysis can aggregate to gas bubbles in the resist layer, or at the resist glass interface, and can cause a peeling of the coating during development. Increasing the delay (by storing the plates during some hours) before development might help, in order for the N_2 molecules to diffuse out of the resist layer.

Two other kinds of baking can furthermore be performed. The first of these, called post exposure bake, is done before illumination of the resist layer. It helps to reduce mechanical stress, increase adhesion, and promote the diffusion of the carboxylic acid, resulting in a softening of the final structures.

The other bake, called hardbake, can be performed once the samples have been developed to increase the mechanical stability of the final resist structures. Depending on the bake temperature there are different chemical reaction occurring in the PAC. Above the softening point, the structures can even begin to flow, resulting in a rounding of the tips.

For our applications, the obtained structures in resist after development were sufficiently stable mechanically so that we did not need any post exposure- neither hard-bake.

4.3 Development

From a microscopic point of view, when the carboxylic acid, produced by the photolysis of the DNQ-sulfonate, enters in contact with the developer, which is an aqueous alkaline solution, it moves from the hydrophobic to the hydrophilic side of the cresol resin (the novolack), as shown in Fig. 4.3.

As a side effect, the developer reacts also with the PGMEA solvent that remains in the resist layer to produce acetic acid. Note that the development rates of both exposed and non-exposed resist increases, resulting in higher dark erosion. The so-called dark erosion comes from the fact that even non-exposed resin does dissolve in the developing process.

The whole process of developing can be described macroscopically in terms of dissolution rate, see Fig. 4.4. The rate depends on many parameters such as, for example, the chemical composition of the more or less exposed resist, as well as the developing parameters.

Developer dilution in water and developing time are very sensitive parameters and play therefore a very important role in the developing process. High dilution ratios results in lower dark erosion effects, but must be compensated by longer developing times to reach the final depth.

In order to minimize the sensitivity of the process to these parameters, the resist can be developed until all the exposed resist is washed away in the developing process [Wittig 2003]. In other words, it only remains the unexposed or bulk part of the resist after development. The dilution ratio of water to developer has to be high enough so that dark erosion effects are minimized. As the developer makes its way through the exposed resist, the tips of the structures are much longer in contact with the developer than the valleys. If the dark erosion is too high the tips, or the finest features of the profile, will be eaten up in the process. As a drawback, the developing times are very long, and the final structures in resist have more noise, that is, the surface roughness increases. In the framework of our applications, we used AZ351B developer with a dilution to water of 8:1 (water : developer), and developing times of 7 minutes for S1818 resist with exposure doses of 110 mJ/cm^2, and 25 minutes for AZ4562 with exposure doses of 120 mJ/cm^2.

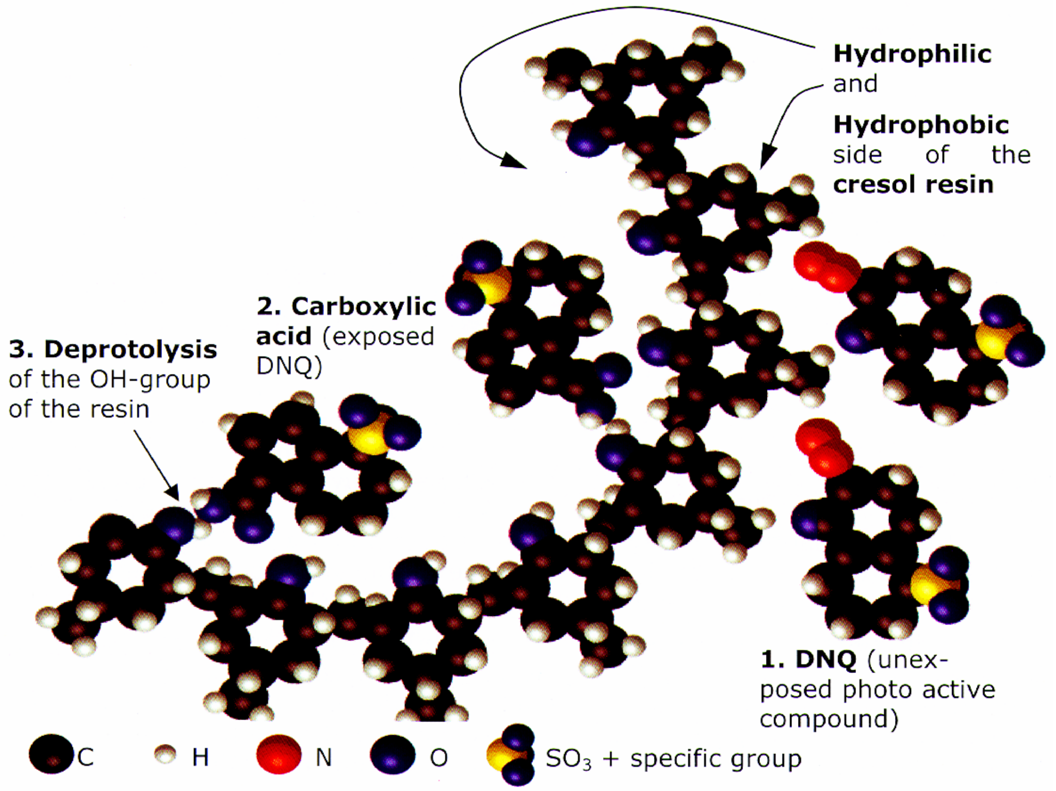

Figure 4.3. Chemical reactions in the resist induced by the alkaline developer aqueous solution. The exposed DNQ moves from the hydrophobic to the hydrophilic side of the epoxy cresol novolac (ECN) resin. Picture taken from "*Lithography Processes*", MicroChemicals Gmbh.

Figure 4.5 shows a curve of resist depth as a function of the developing time for AZ4562. A plate coated with an 8µm resist layer was exposed with 236 mJ/cm^2 at 413nm wavelength. The depth was then measured from the glass-resist interface to the top of the resist layer with an Alphastep 500 profilometer. For the initial height measurement, the plate was first immersed in pure water. Consequently, the layer was completely hydrated. For the next measurements, the plate was immersed in AZ351B developer with a 8:1 (water : developer) dilution ratio and rinsed in pure water before being immediately measured with the profilometer. The same plate is then further developed in the same developer bath. Note that the plate is gently moved back and forth in the liquid with a teeter stage. Several plates were measured and the results were reproducible.

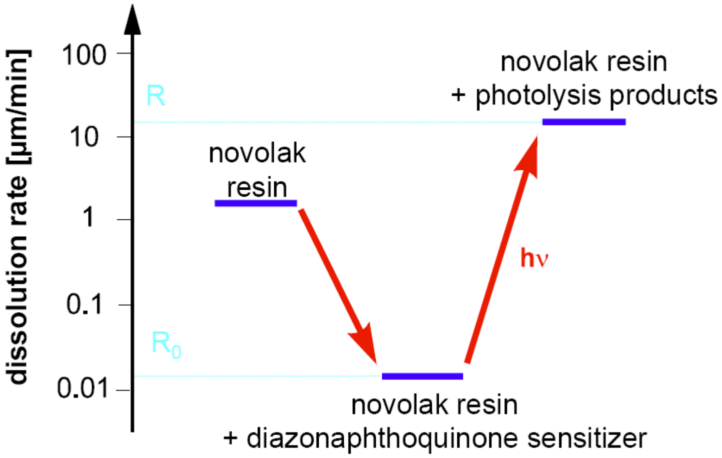

Figure 4.4. Schematic of the various dissolution rates states depending on the chemical composition of the resist. As can be seen, the DNQ acts as a dissolution inhibitor of the novolack resin. However, once the DNQ is fully exposed, the solubility R of the couple novolack-photolysis products is higher than R_0, that of sole novolack.

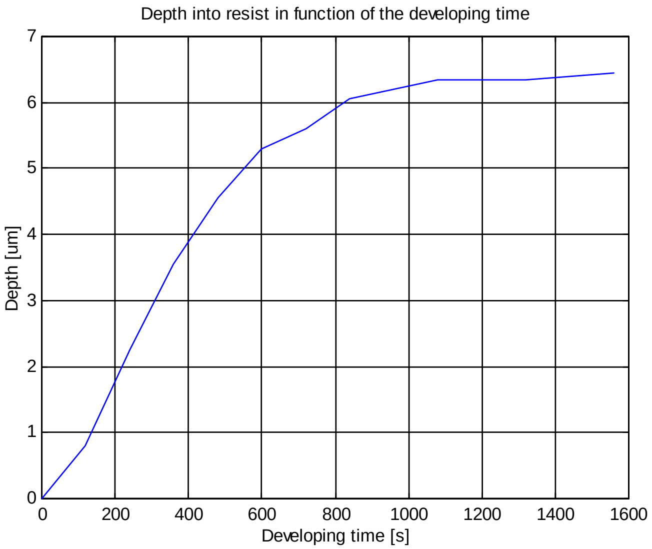

Figure 4.5. Graph showing measurements of the depth in an AZ4562 resist layer with the developing time.

At about 18 minutes, the curve flattens and almost no resist is removed. From that point, it can be assumed that only unexposed or bulk resist remains. Note also that the dark erosion is very low due to the high dilution ratio we used. For structured areas, we have chosen to develop above this point (25 minutes) to ensure that the developer fully dissolves the exposed resist at the bottom of the profiles. With such long developing times, we found the whole developing process to be less sensitive and therefore the resulting structures to be more reproducible.

Figure 4.6 and 4.7 show SEM pictures of gratings resulting from a sinusoidal intensity distribution of 112 mJ/cm^2 peak-to-peak energy dose and different doses of constant energies (also called pre-exposures).

The grating periods are 1µm and 3µm for Fig. 4.6 and 4.7, respectively. The sinusoidal intensity distribution was produced by two-beam interference lithography. The whole resist coated plate was exposed first with the sine grating, and then divided in stripes exposed separately by a single plane wave with different exposure times and therefore different exposure doses.

The effect of increasing the pre-exposure dose, as can be seen in the Fig. 4.6 and 4.7, is to augment the solubility of the structures. As the development process is isotrope, the resist is dissolved in all directions. As a consequence, the structures become deeper, as can be seen in Fig. 4.6 (a) and (b). Simultaneously, the grating tips become also thinner until they finally break and get washed away in the development process. This occurred between the images represented in Fig. 4.6 (b) and (c), or Fig. 4.7 (a) and (b). Above that pre-exposure dose, the structures become rounder and shallow, as can be seen in Fig. 4.6 (d) to (f), or Fig. 4.7 (c).

Although the gratings represented in Fig. 4.6 and 4.7 were exposed under exactly the same conditions, the grating period aside, which is 1µm and 3µm respectively. Thus, the obtained structure height as well as the profile shape differs. For instance, compare Fig. 4.6 (a) to Fig. 4.7 (a), which structure height is 2.4µm and 3µm, respectively. This illustrates the difficulty to predict accurately the final structure with regard to the exposed energy distribution.

Many models have been proposed, see [Bartolini 1972, Austin 1976, Tsang 1977, Mashev 1981, Mello 1995, Dill 1975] to predict the final profile structure, with more or less accuracy, notably when the grating period is less than 1µm [Zanke 1998]. Unfortunately, fundamental experimental evidence of the exact mechanism of resist development is lacking. The accurate simulation of the final profile has to take into account the bleaching of the resist during exposure, as well as the local change of the dissolution rate at the resist-developer solution interface that is continuously changing during the process.

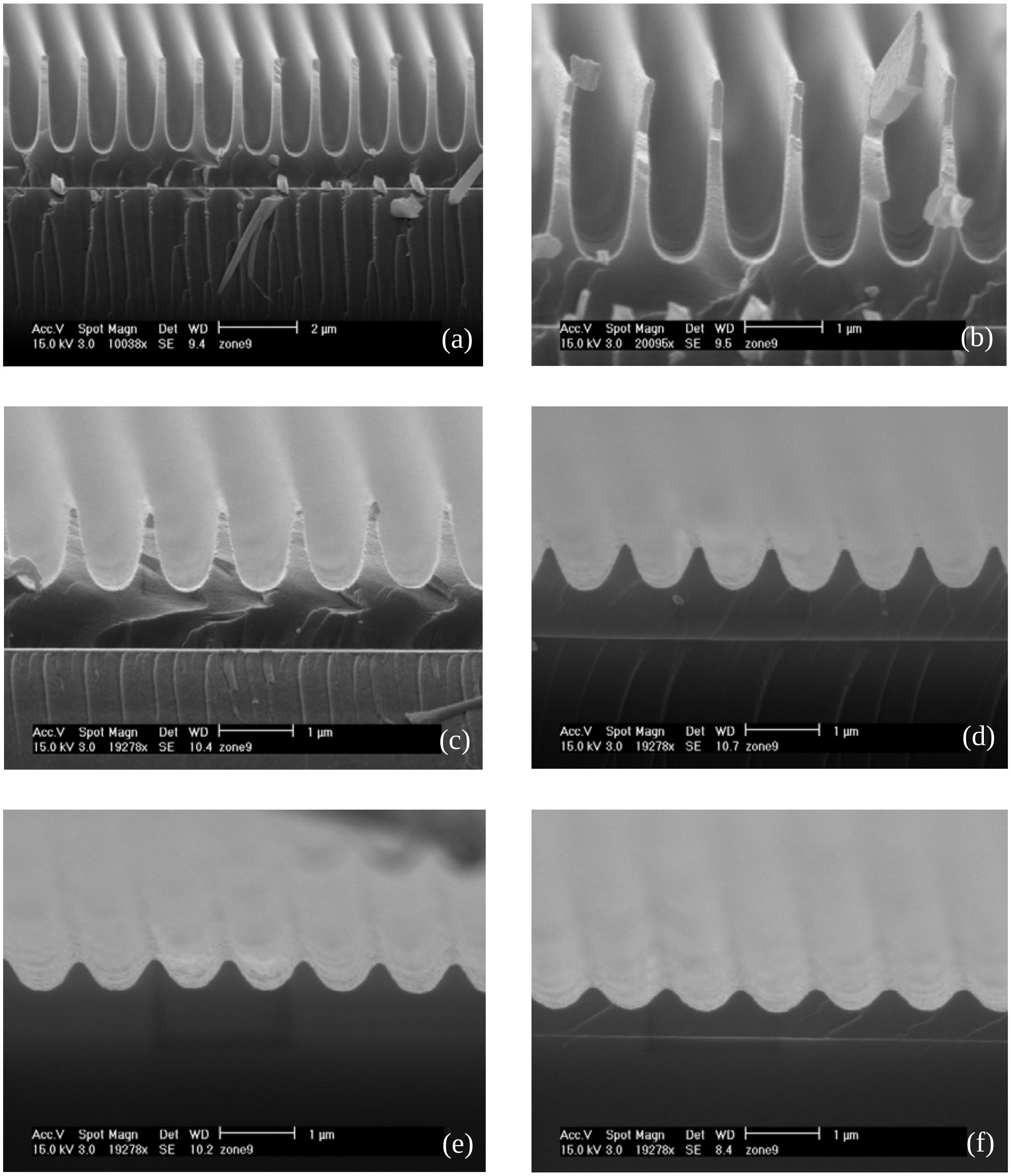

Figure 4.6. SEM pictures of resist gratings with 1μm period are shown. The gratings were exposed with a sinusoidal intensity distribution with 112mJ/cm^2 peak-to-peak energy, and pre-exposed energy doses of 0, 6.3, 12.6, 21.5, 30.3 and 41.7mJ/cm^2 for (a) to (f) respectively.

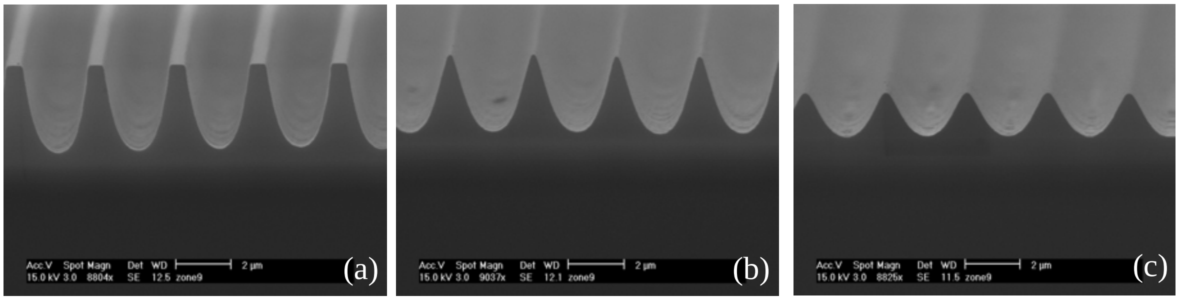

Figure 4.7. SEM pictures of resist gratings with 3µm period are shown. The gratings were exposed with a sinusoidal intensity distribution with 112mJ/cm^2 peak-to-peak energy, and pre-exposed energy doses of 0, 12.6, and 30.3mJ/cm^2 for (a) to (c) respectively.

4.4 Exposure profile adaptation

The whole chain of processing of the resist consists in many steps. The most critical step is the developing, which impacts very sensitively the response of the resist with regard to the exposed pattern. Many mechanisms occurring in the chemistry of resist are still not known. Thus an exact modeling is difficult in particular when the feature size of the structures is below 500nm.

Even though the modeling of the resist response is not accurate for such small structures, the realization of arbitrary profiles is nonetheless possible with good results. The principle, as shown in Fig. 4.8, is to start with an approximation of the final profile and then correct the illumination iteratively until the final structure profile reaches the needed precision.

For the initial try, the profile of the illumination corresponds to the desired target profile. The depth of the profile, which corresponds to the maximal energy dose, should fit in the layer of resist and approximately be at the level of the final desired profile. As the top of the profile is longer in contact with the developer than the bottom, it is more eroded and its tips can even get broken in the development process depending on the shape of the target profile. It might well be that the initially realized structures do not have the right height at the beginning. As a consequence, throughout the iterations and the successive corrections brought to the illuminated energy distribution, the top of the structure will constantly move. On the other hand, the depth of the profile can also be affected, but significantly less then the top, depending on the developer flow in the valleys of the structure. In other words, the shape as well as the height of the realized profile is affected by the illumination function parameters, such as distribution and energy dose. That complex process is not well determined and depends also on the target structure function profile.

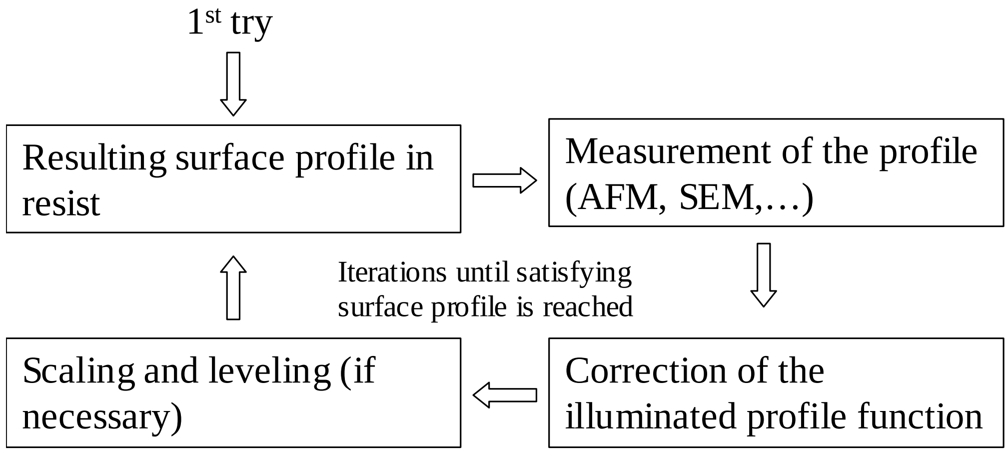

Figure 4.8. Block diagram of the exposure profile adaptation.

The question is, which energy level (the minimum, the maximum, or the mean) is best to choose to fit the parameters of the corrected illumination with respect to the measured resulting profile between two iterations? As the development process less affects the bottom of the structure, the maximum exposure dose of the energy distribution, which corresponds to the desired depth of the target profile in the resist, will be chosen for reference to correct the shape of the illumination. In other words, to fit the corrected illumination distribution, the maximum energy level is kept equal before and after the correction. By looking at the difference between the obtained profile and the desired profile into the resist the adaptation of the illumination can then be done. In our case, the adaptation consisted in adding the difference between the realized profile and the target profile in resist in the same proportions to the illumination distribution. Note that between iterations, the maximum energy dose may have to be adapted in order for the depth to be at the desired level.

In each iteration loop, the realized profile is compared to the target profile and the difference is added proportionally to the current iteration’s illumination function, which is also the illumination distribution of the following iteration). Figure 4.9 and 4.10 show an example for the realization of micro-prisms.

Although, we had good results, other adaptation rules might be applied, such as taking half of the difference, for example.

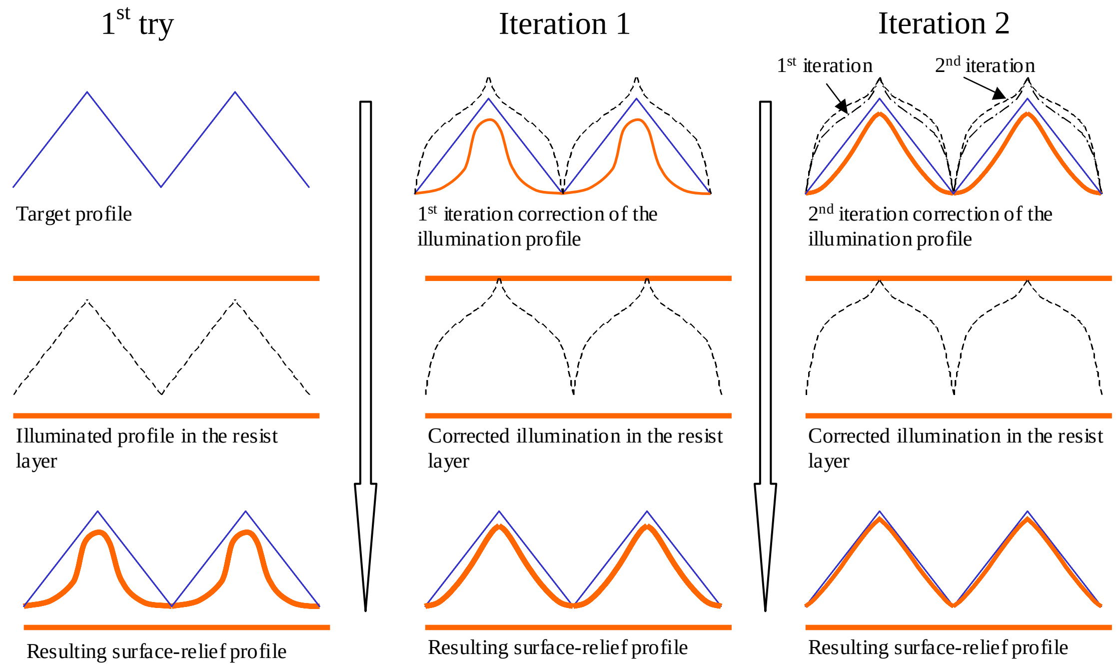

Figure 4.9. Schematic of the exposure profile adaptation for micro-prisms and two iterations. The realized structure converges to the target profile through the iterations.

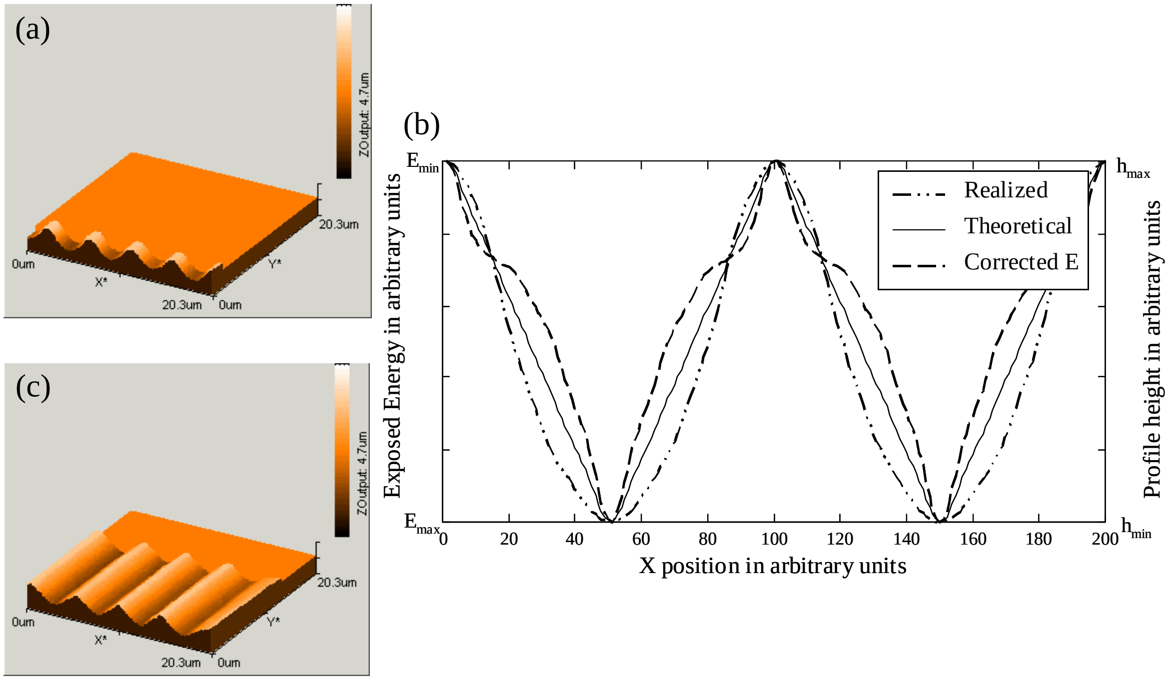

Figure 4.10. Exposure profile adaptation for the realization of periodic micro-prisms. The measured profile of the realized structure in (a) and (b) corresponds to the theoretical exposure profile shown in (b), while the measured profile in (c) corresponds to the corrected exposure profile shown in (b). The graph in (c) illustrates the matching of the levels for the exposed energy and measured height profile.

4.5 Summary

In that chapter, we explained briefly the various chemical reactions and mechanisms occurring in positive DNQ-based photoresist through all the processing. The photoresist is sensitive to many parameters and therefore its response is difficult to predict accurately. The development process in particular is critical. That step is still not well known and a precise modeling for features less than 500nm in lateral size is lacking. However, we achieved to realize profiles with features less than 500nm by adapting the illumination conditions. The illuminated profile was iteratively adjusted until the realized structure’s profile corresponds to the target profile in a satisfying way.

CHAPTER 5

MICROSTRUCTURES FABRICATED BY FOURIER SYNTHESIS

The Fourier Synthesis (FS) technology that we introduced through chapter 2 (section 2.2) and 3 (section 3.2) is a powerful tool to realize arbitrary periodic profile. By means of three examples, we will demonstrate the potential of FS to realize designs for Diffractive Optical Elements (DOEs). These examples represent only a selection of a few interesting DOEs among others.

In our first example, we look at blazed gratings which have saw-tooth profiles. Blazed profiles have been investigated since long time ago [Wood 1910], and many technologies and ideas have been developed to produce them. Depending on the used technology such as direct laser writing [Gale 1994], gray-tone lithography [O'Shea 1995], E-beam writing [Eckberg 1994] or diamond turning [Blough 1995], saw-tooth profiles of various lateral dimensions have been produced with good to very good results, that is, with 70 to 98% of the maximum possible first order diffraction efficiency. Note that this maximum efficiency depends on the ratio of structure period to design wavelength. The novelty of the FS technology developed within this thesis lies in the dimensions and performances of the fabricated elements. The period of the saw-tooth profile is in the order of a few wavelengths in the visible spectrum range. Thus, diffractive lenses with very high numerical aperture could be achieved. Indeed large structured areas (in the order of several square centimeters) with fine-pitched structures (down to 700nm) can be realized by FS, thus allowing large deviation angles and therefore high numerical apertures.

In our second example, we investigate periodic micro-prisms that find their application as linear retro-reflectors. These structures are intended to reflect light back to the source for any incident angle and for the whole visible spectrum. The profile consists of periodic and symmetrical right-angled prisms, where the hypotenuse is the bottom of the profile. Typically the periodic structures of such devices have dimensions between a few tenths to hundreds of micrometers in lateral size and their height is the half of the period; therefore the light is redirected in the refractive regime. The fabricated periodic micro-prisms that we show here are less then ten microns in size. As a consequence, the period of the structure is in the order of a few wavelengths of the incoming light, that is the visible spectrum in our case, and thus the retro reflector structure cannot be considered anymore as purely refractive. We will investigate the effect of the light diffraction on the retro reflector function. Reducing the lateral size reduces also the profile height of the retro-reflector. With a height less than ten microns, they can easily be replicated in a thin foil of metal as it is used in mass production processes such as roll embossing [Gale 1997].

In our last example, we propose a novel design for highly efficient fan-outs with high angles of deflection. A fan-out is an optical device that divides an incoming beam of light in several beams of equal intensity.

5.1 Blazed structures

Our first example is a blazed grating with the well-known saw-tooth profile. The grooves are so shaped that at each point in the aperture a phase lag is introduced that compensates for that introduced by the redirection of the wavefront. For cases in which scalar approximations and in particular the Fourier approximation [Goodman 1996] are valid, the ideal profile is often a triangular saw-tooth profile.

The blazed grating can be described by the function $I(x) = a \cdot x$ over one period Λ of the grating, i.e. for $0<x<\Lambda$, a being a constant determining the slope of the blazed grating profile. Note that for $x = m \cdot \Lambda$, m being an integer, $I(x)$ is discontinuous. The Fourier expansion of such a function can be written as:

$$I(x) = I_0 + I_1 \cdot \sum_{n=1}^{+\infty} \frac{1}{n} \cdot \left(1 + \cos\left(n \cdot k \cdot x + \pi/2\right)\right). \tag{5.1}$$

$k = 2\pi/\Lambda$ is the spatial frequency, and I_0, I_1 are constants used to adjust and scale the function. In Fig. 5.1 (a), one can observe how $I(x)$ behaves with limited numbers of Fourier components, and in particular the ringing near the discontinuity.

Since the realized gratings are produced by a finite number of sequential exposures, the oscillation around the theoretical profile can also be observed on the realized profile in Fig. 5.1 (b). One can clearly see the 7 components used to approximate the saw-tooth profile by looking at the tiny waves on the profile as well as the vertical stripes due to the fact that the picture was taken obliquely. Note that the features generated by FS, i.e. the typical ringing at the borders of each period, see Fig. 5.1 (a), have been dissolved during the development of the resist structures. Indeed, the processing of the resist softens the edges of the profile.

In Figure 5.2, numerical simulations for the first order diffraction efficiency are presented for different numbers of Fourier components used to approximate the saw-tooth profile. The calculations were done for structure periods ranging from 1 to 10 design wavelengths and slopes a (as defined in $I(x) = a \cdot x$) ranging from 0 to 1 (corresponding to a blaze angle ranging from 0° to 45°), applying rigorous diffraction theory at normal incidence. We considered an air to resist (n_{resist}=1.68) interface.

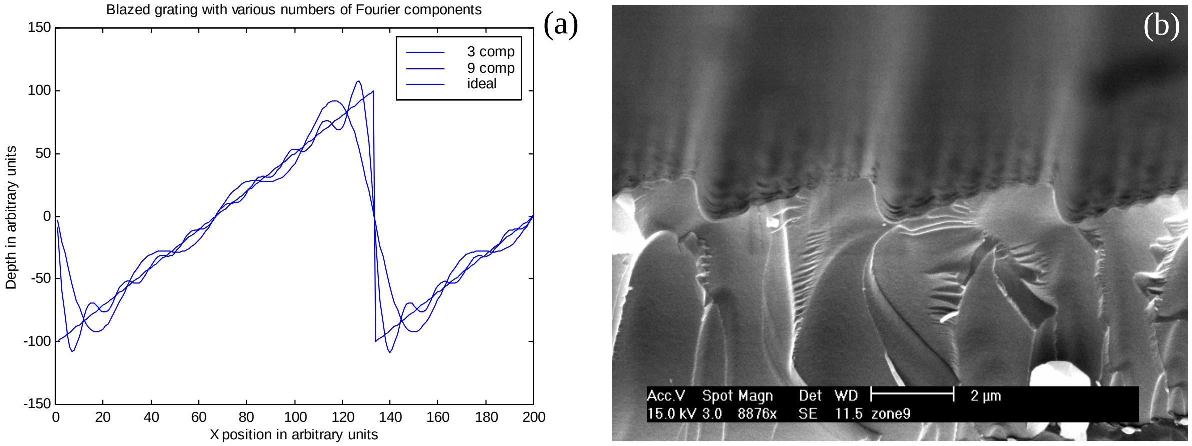

Figure 5.1. Illustration of the saw-tooth profile for blazed gratings.
In (a), the numerical calculations show the saw-tooth profile approximated with different numbers of Fourier components.
In (b), SEM picture of a realized profile in resist with 7 components. The period is approximately 4.4µm and the height 1.1µm.

The maximum possible first order diffraction efficiency η_1 depends on the ratio of the structure period to design wavelength ($\Lambda_{structure}/\lambda_{light}$) and the number of used Fourier components to approximate the profile. It increases with the number of used Fourier components that is, η_1 = 0.59, 0.71, 0.77 and 0.84, for 2, 3, 5 and 10 Fourier components, respectively.

For a low number of Fourier components, the maximum efficiency occurs towards the small period to wavelength ratios. With 2 or 3 components, the maximum efficiency is obtained at about 2 period to wavelength ($\Lambda_{structure}/\lambda_{light} \cong 2$) and a slope a of 0.6 (corresponding to a blaze angle of 31°), see Fig. 5.2 (a) and (b). On the other hand, for a greater number of Fourier components, the maximum efficiency occurs at higher period to wavelength ratios, e.g. approximately 8-10 and a slope of 0.2 for 10 Fourier components, as can be seen in Fig. 5.2 (d).

Indeed, each harmonic used to generate the profile contribute to the diffraction figure of the structures. The contribution of the superior harmonics, the first harmonic being the base period of the structure $\Lambda_{structure}$, depends mainly on the number of propagating orders, which is less or equal to the $\Lambda_{structure}/\lambda_{light}$ ratio. The contribution of the harmonics that have a number superior to $\Lambda_{structure}/\lambda_{light}$ is minor in comparison to that of the lower harmonics. That explains why the number of useful harmonics to approximate the structure is about equal to the $\Lambda_{structure}/\lambda_{light}$ ratio to obtain maximum diffraction.

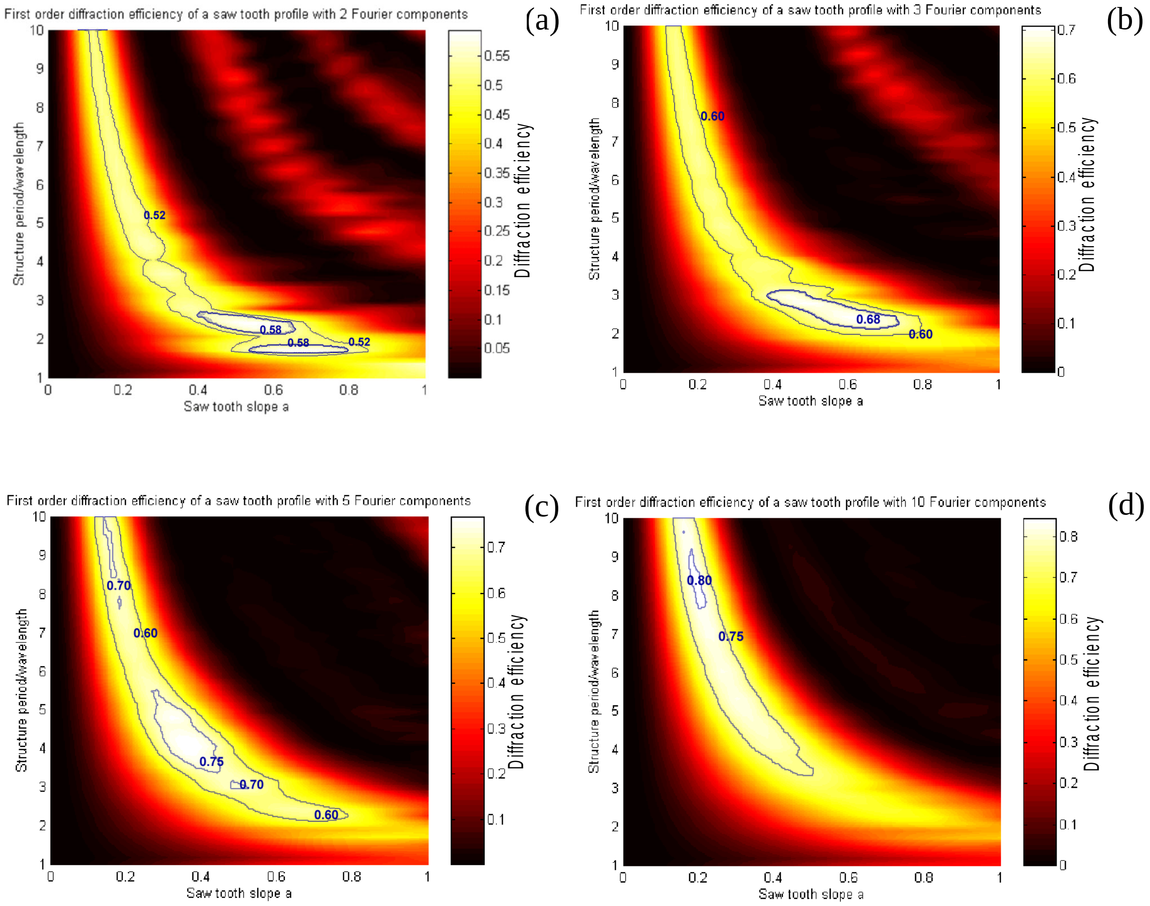

Figure 5.2. First order diffraction efficiency of a saw-tooth profile approximated by different numbers of Fourier components. In (a) to (d), the structure is approximated by 2, 3, 5 and 10 components, respectively.

Nonetheless the absolute diffraction efficiency is higher with a larger number of Fourier components in any case, that is, for any period to wavelength ratio or slope. However, increasing the number of Fourier components from 5 to 10, does not improve significantly the efficiency (Δ=0.07%). Thus, depending on the needs of the application, one might expose lesser Fourier components to improve the yield.

Figure 5.3 shows some results of a realized saw-tooth profile using FS. The structure height was optimized to have maximum 1^{st} order diffraction for a normally incident red HeNe beam at 633nm. The dimensions of the laser spot were approximately 0.5 mm. To generate the blazed grating, as represented in Fig. 5.3 (a), we exposed the photoresist with an intensity distribution $I(x)$, as shown earlier in Eq.(5.1), by using 9 components and a preexposure, resulting in a total of 10 exposures.

For the exposure, we used the Fourier Synthesis (FS) method, see section 2.2, and the optical setup described in section 3.2. The period of the blazed grating is 2.2µm, and its depth is about 900nm. The light deflection is therefore 16.7°. Figure 5.3 (b) shows the diffracted order efficiencies at 633nm of the structure represented in Fig. 5.3 (a).

The measurements agree well with the numerical calculations. The first order diffraction of the realized structure is $\eta_{meas} = 0.585$ while the calculated value, corresponding to the measured profile in Fig. 5.3 (a), is $\eta_{calc} = 0.63$ and $\eta_{ideal} = 0.62$ for an ideal saw-tooth profile with optimal height. Therefore, the realized structure reaches 93% of the theoretical maximum. The realized profile has a higher theoretical efficiency than an ideal saw-tooth profile at that period to wavelength ratio (i.e. $\Lambda_{structure}/\lambda_{light} \cong 3.5$). The saw-tooth profile function has been determined to be the ideal profile for very large structure periods $\Lambda_{structure}/\lambda_{light} >> 10$. For smaller periods, as is our case, the ideal profile might have to be calculated.

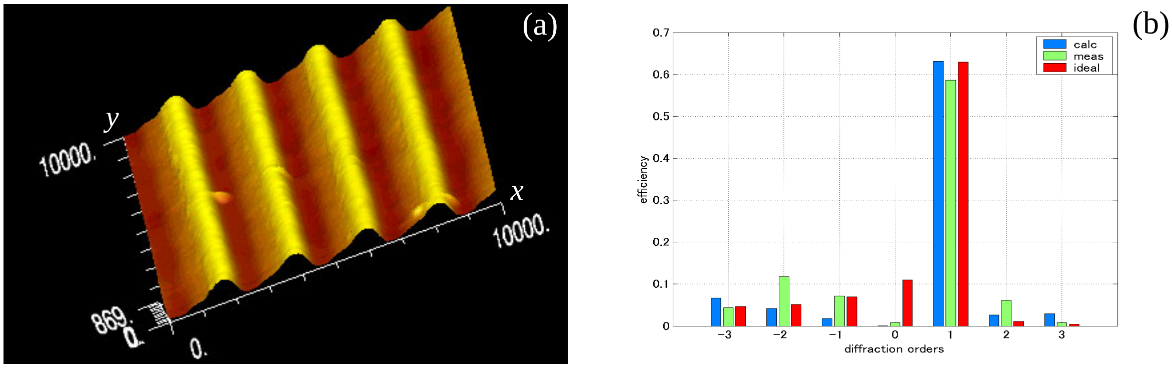

Figure 5.3. Realized saw-tooth profile with 9 Fourier components.

In (a), an AFM measurement of the structure in resist is shown.

In (b) are shown in bright the measured diffracted efficiencies, in dark, the numerical calculations of an ideal saw-tooth profile and in gray, numerical calculations of the measured profile from (a). The calculations for the ideal saw-tooth were done for a period of 2.2µm and for an optimized height to reach the highest possible first order efficiency.

The effect of the error on the component's period, as described in section 2.2.2, can be seen in Fig. 5.4. Three SEM pictures illustrate how the structure profile becomes more and more distorted with increasing distance due to the phase mismatch between exposed Fourier components. The phase mismatch increases from the left (where the phase error is minimum) to the right, the pictures being taken in a range of approximately 2mm lateral distance on the sample.

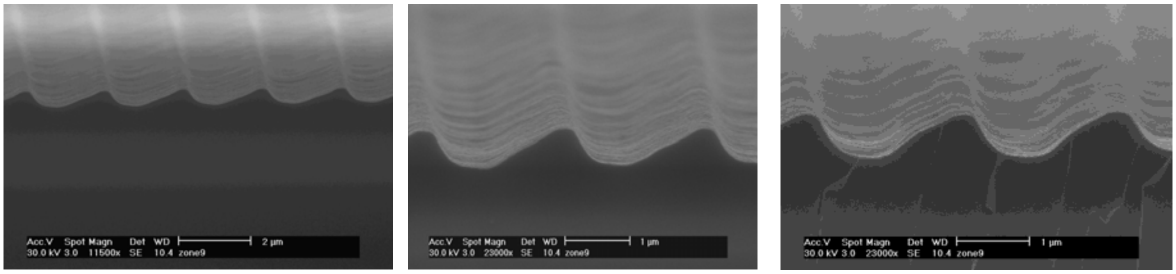

Figure 5.4. SEM pictures of a realized blazed grating with 8 Fourier components, at various positions along the *x*-axis as defined in Fig 5.3 (a). Note that one can observe how the development process rounds the edges. The sidewalls are less steep then expected and the bottom of the profile, in particular, is widened. For comparison, one can look at the theoretical illuminated profile represented in Fig. 5.1 (a).

5.2 Micro-prisms as retroreflectors

Prisms can be defined as solid figures whose bases or ends have the same size and shape and are parallel to one another, and each of whose sides is a parallelogram. In optics, they are usually a transparent body of this form, often of glass and usually with triangular ends, used for separating white light passed through it into a spectrum or for reflecting beams of light. Extensive research has been done in the fabrication of micro-prisms, see e.g. [Eisenberg 2005, Gimkiewicz 1999, Sinzinger 2003]. But prisms can also be used as retroreflectors.

A retroreflector is a device that sends light or other radiation back where it came from regardless of the angle of incidence, unlike a mirror, which does that only if the mirror is exactly perpendicular to the incident light beam. This effect can be commonly obtained with a set of three perpendicular mirrors, which form a corner (a corner reflector or corner cube).

To realize a planar retroreflector surface, it may then consist in many very small versions of this structure incorporated in a thin sheet or in paint. In the case of paint containing glass beads, the paint glues the beads to the surface where retroreflection is required, and the beads protrude, their diameter being about twice the thickness of the paint.

A second, much less common way of producing a retroreflector is to use the nonlinear optical phenomenon of phase conjugation [Tomita 1979, Diel 1984]. This technique is used in advanced optical systems such as high-power lasers and optical transmission lines.

In this section, we consider a one-dimensional array of metallic micro-prisms to realize a retroreflecting surface. Therefore the optical effect is obtained for a single plane of incidence of the incoming light that is perpendicular to the grooves of the periodic structure. Figure 5.5 represents a schematic of a linear array of isometric prisms used as metallic retroreflectors. The figure shows an incoming beam of light with various angles of incidence. This arrangement can also be considered as a periodic grating with a triangular profile, where the grating period Λ represents the length of the prism's base, and α is the apex angle of the isometric prism. Note that perfect retroreflection is achieved when the apex angle is at right angle.

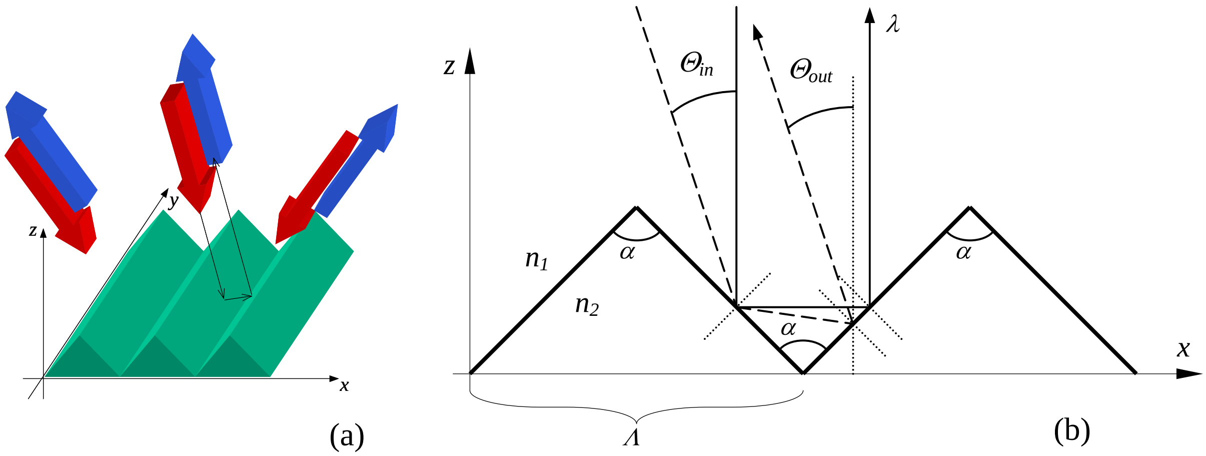

Figure 5.5. Schematic of the geometry of a linear array of metallic micro-prisms used in reflection. The incident beam of light is orthogonal to the grooves of the prisms. In (a), a three-dimensional representation of an incident beam of light is shown for 3 different angles of incidence. In (b), the optical path of a ray of light is shown for normal incidence (the solid line) and for oblique incidence (in dashed line).

For a grating period much larger than the wavelength of light ($\Lambda >> \lambda$), the incoming ray is reflected two times by the geometry of the profile according to Snell's law in reflection. In our case, the sides of the prisms consist of planar metallic mirrors. If the apex angle α is right-angled, the outgoing beam is redirected under the same angle Θ_{out} as the incoming one independently from the incidence angle Θ_{in}, see Fig. 5.5 (b). If the angle α is not exactly at right angle, the outgoing beam is redirected with an angle Θ_{out} =

Θ_{in} + Δ. Therefore, the outgoing angle is shifted by a constant $\Delta = \alpha - \pi / 2$. If the angle of incidence increases to a value above $\alpha/2$, the outgoing beam is reflected a single time on one of the sides of the prisms and therefore the outgoing angle is $\Theta_{out} = \pi - \alpha - \Theta_{in}$. Thus, the profile of the grating acts as a perfect retroreflector for a right-angled prism as long as the angle of incidence does not exceed $\pi/4$.

One can find a study of the theoretical diffraction behavior of periodic metallic (Au) micro-prisms used as retro-reflectors [Ichikawa 2004]. The calculations are done for a wavelength to structure period ratio ranging from 1 to 100.

The shape of a periodic function with isometric triangles or prisms can be described by the Fourier series of the Λ-periodic function $I(x)=|x|$, for $-\Lambda/2 < x \leq \Lambda/2$. The series can be written in the form:

$$I(x) = I_0 + I_1 \cdot \sum_{n=1}^{+\infty} \frac{1}{n^2}\left(1+\cos\left(n \cdot k \cdot x\right)\right) \tag{5.2}$$

for n integer and odd. $k = 2\pi/\Lambda$ is the spatial frequency of the profile. The function $I(x)$ represents the intensity that was exposed in a resist layer using the Fourier Synthesis (FS) method described in sections 2.2 and 3.2. The constants I_0 and I_1 allow to adjust and scale the final surface profile. They have to be tuned such that (a) the recording process works in the sensitive area of the photoresist's response, and (b) the desired structure height is correct. Note that to have an apex angle of 90°, the height of the structure has to be half of the grating period Λ. The shape of such a function is represented in Fig. 5.6 (a) for limited numbers of Fourier components. One can see that for 9 components, and therefore 5 exposures (indeed, only the odd components are non zero), the series approximate the target profile almost perfectly, although, at the tips, the approximated function does not follow the sharp edges. However, that was not a limiting factor for the realization. We found that the resist's response and its processing, in particular the development step, to be the limiting factor to obtain sharp and well defined edges.

The profile represented in the AFM measurement in Fig. 5.6 (b) and (c), has been generated using FS in combination with Exposure Profile adaptation (EPA) as described in section 4.4.

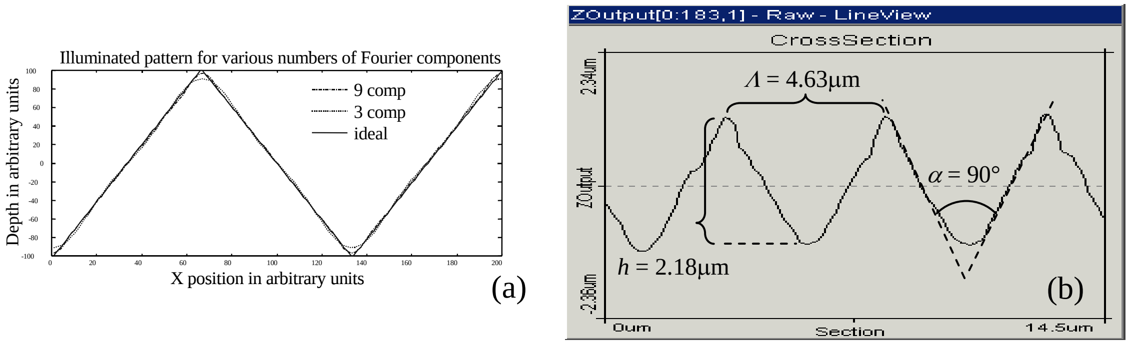

Figure 5.6. Prismatic profiles approximated by Fourier synthesis.

In (a), the mathematical profiles calculated according to Eq. (5.1) show how the truncated Fourier series approaches the desired function with increasing number of Fourier components.

In (b), AFM measurement, of the realized profile in resist are shown in 3 dimensional representation and in cross section, respectively. The period of the structure is 4.63µm and the height approximately 2.2µm, therefore the apex angle is about 90°.

The illumination profile was iteratively adjusted until the profile into resist gave satisfying results. The starting point for the adjustment of the illumination was the theoretical profile given by Eq. (5.2). To obtain the final structures in metal, the micro-prism grating originated in resist has than been transferred in Nickel by electroforming. Experimental results as well as numerical calculations for the diffraction efficiency of the structures in metal are presented in Figs. 5.7 to 5.9.

Since the structure is periodic, we can observe discrete diffraction orders. The figures show the distribution of the diffraction orders for different angles of incidence (0° being the normal to the sample). To simplify the comparison between the different wavelengths, the diffraction order efficiencies are represented in angular spectrum and are connected with solid lines.

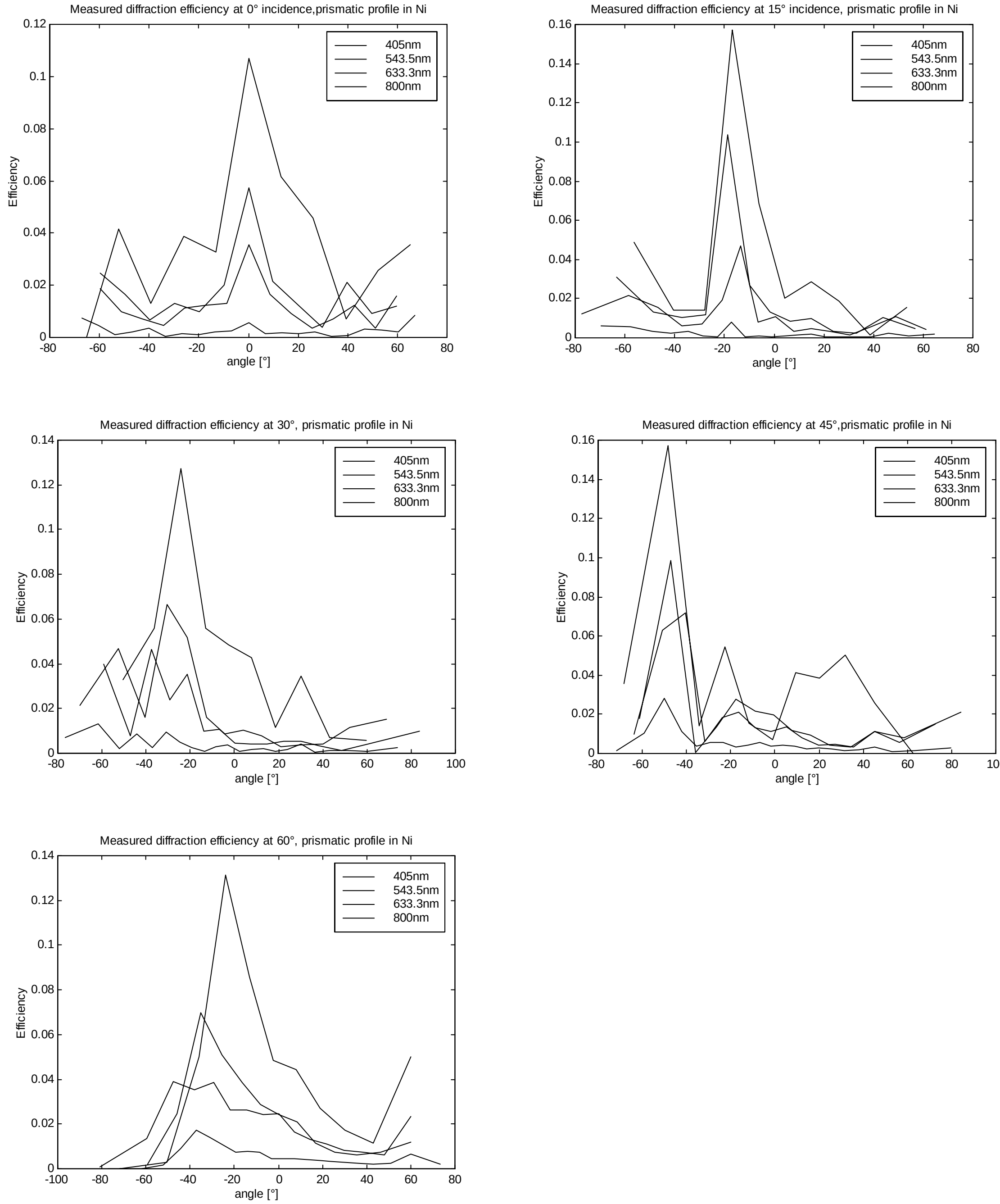

Figure 5.7. Measured diffraction efficiencies (absolute values) of the realized metallic micro-prisms in reflection. The graphs show the efficiency of the measured diffraction orders for different incidence angles (0°, 15°, 30°, 45° and 60°) and wavelengths (405nm, 543.5nm, 633.3nm and 800nm).

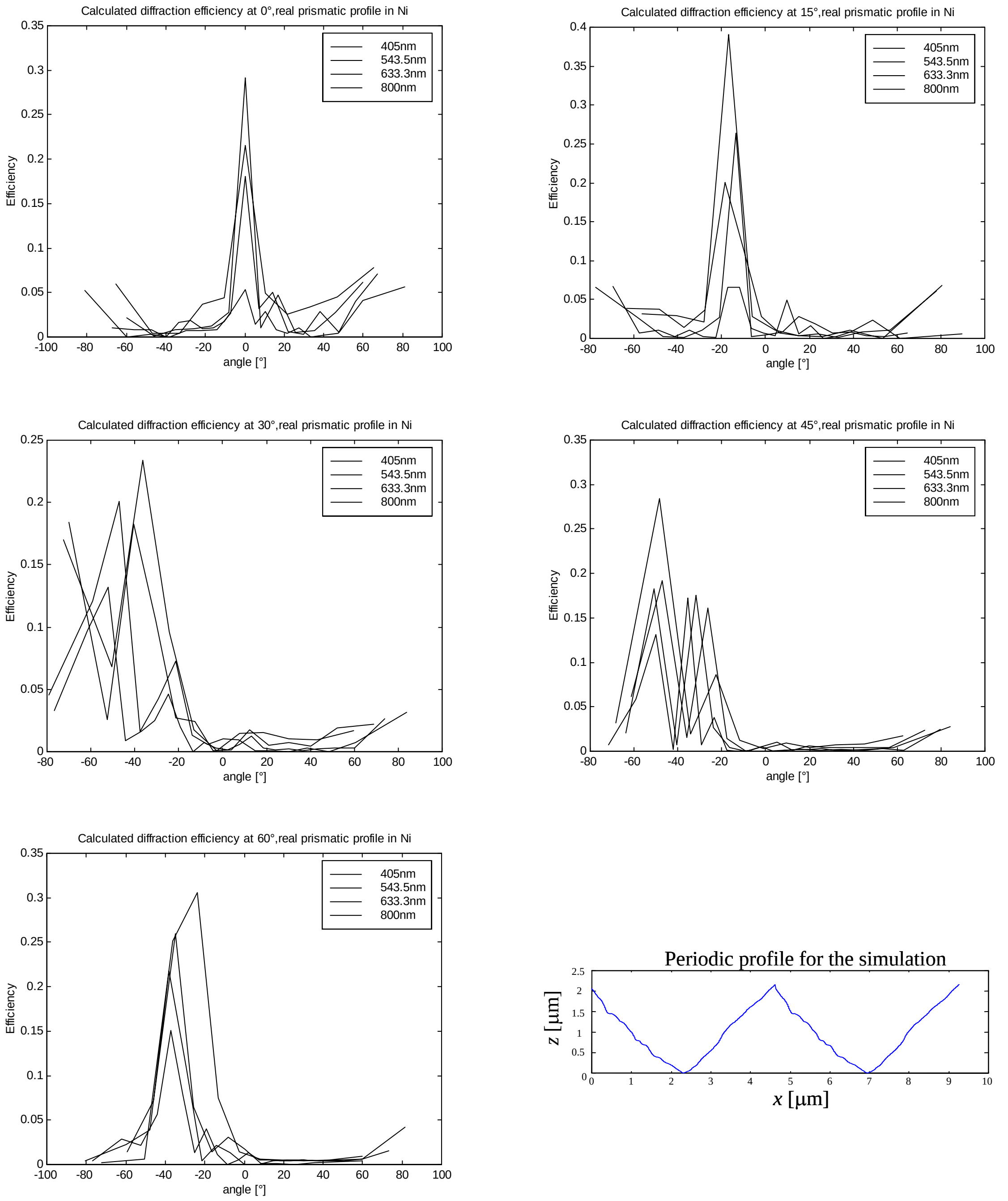

Figure 5.8. Calculated diffraction efficiencies (absolute values) in reflection of the periodic profile represented in the down right corner. The profile is a cross section of the AFM measurement of the realized metallic micro-prisms, see Fig. 5.6 (b). The graphs show the efficiency of the diffracted orders for different incidence angles (0°, 15°, 30°, 45° and 60°) and wavelengths (405nm, 543.5nm, 633.3nm and 800nm).

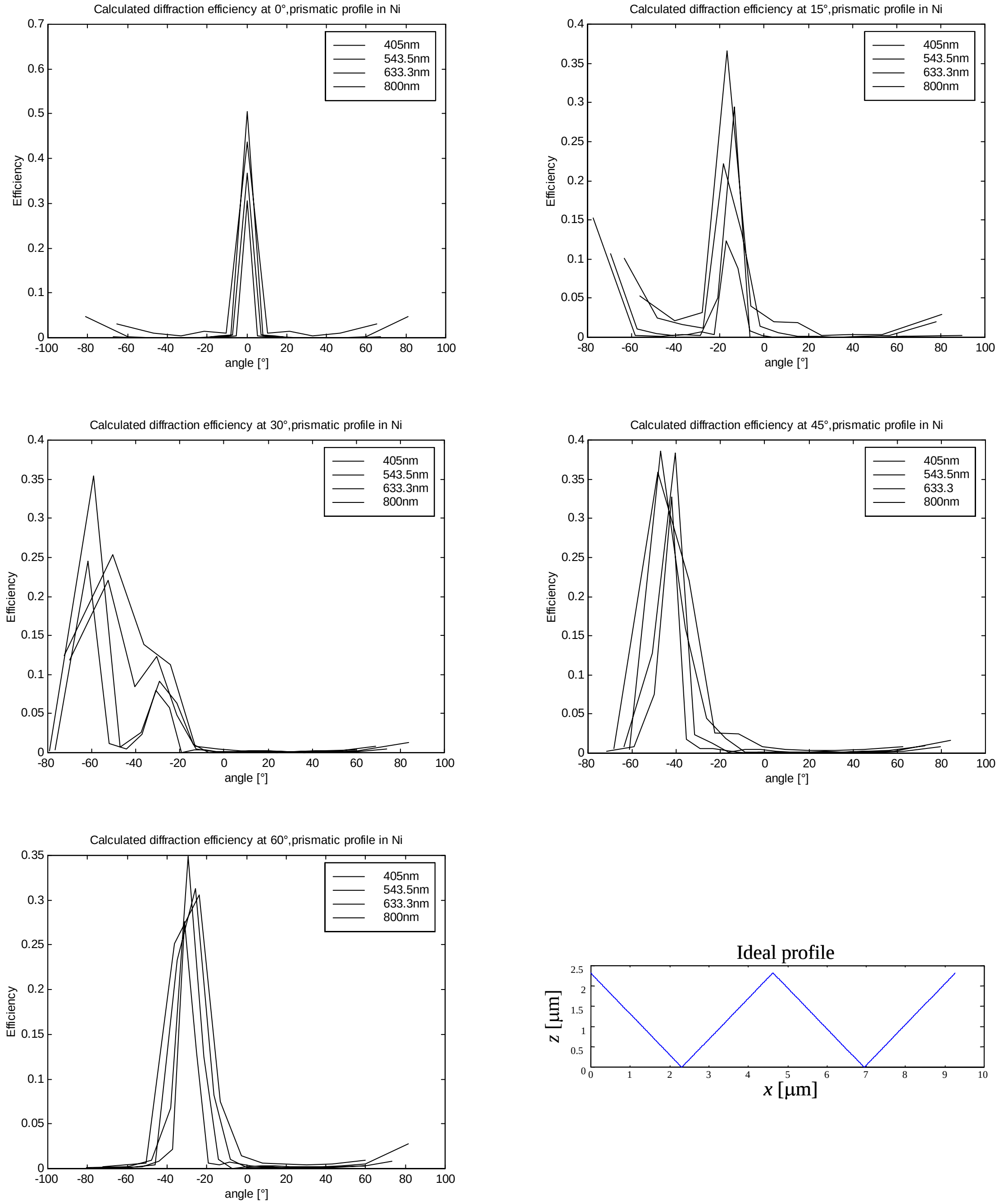

Figure 5.9. Calculated diffraction efficiencies (absolute values) in reflection of metallic micro-prisms with an ideal profile as shown in the down right corner. The graphs show the efficiency of the diffracted orders for different incidence angles (0°, 15°, 30°, 45° and 60°) and wavelengths (405nm, 543.5nm, 633.3nm and 800nm).

The experimental diffraction measurements were done for four different wavelength spread over the whole visible spectrum. The 405nm and 800nm light sources were laser diodes while the 543.5nm and 633.3nm light sources were standard HeNe gas lasers. All sources were stable within a few percent. The measurements were done with bear beams of light for the 405nm, 543.5nm and 633.3nm sources. The beam diameter of those sources was less than 0.8mm, and the beam divergence less then 1mrad. The 800nm laser diode had a 3 (in the horizontal plane) by 1μm (in the vertical plane) rectangular emitting junction. Therefore, the beam was elliptical and its divergence was 9° in the horizontal plane and 30° in the vertical plane. Due to the divergence, the beam had to be focused by a lens. The lateral spot size on the sample was approximately 1mm for all sources. At each wavelength, we illuminated the sample for 5 different incidence angles: ~0°, 15°, 30°, 45° and 60°. Note that the measurements being done in reflection, the angle for the normal incidence is slightly off of 0°, i.e. 0.2-0.5°, to avoid interferences between the detector and the incoming beam of light. The diffracted orders as well as the incoming beam were measured with a silicium photodector. The detection area was approximately 64mm^2.

The experimental data can be found in Fig. 5.7. From the measurements, one can see that the diffracted light have a maximum at the orders located near to the incidence angle (in absolute value) for all wavelengths. In other words, the light being diffracted (the light is redirected in discreet directions), the intensity peak is located at the order's angular direction that is the nearest to the incidence angle as defined in Fig. 5.6. For example, at 15° incidence, the diffracted light has a peak located at –17.06° while at 45° incidence the peak is at –42.34° for 405nm wavelength. One can clearly see that the light is reflected back to the source for incidence angles lower than 45°. Therefore, the retro-reflection effect has been achieved. Note that as expected, for incidence angles over 45°, there is no retro-reflection. For instance, at 60° incidence, the light intensity peak is located between approximately –38° and –25° depending on the wavelength.

For comparison, Fig. 5.8 shows numerical simulations of the diffracted efficiency for a profile according to the AFM measurements of the realized sample while Fig. 5.9 shows numerical simulations for an ideal prism with 90° apex angle. The calculations were done using rigorous theory for 5 different incidence angles corresponding to the experimental efficiency measurements, therefore 0°, 15°, 30°, 45° and 60°. Note that the refractive index of Ni depends on the wavelength. Therefore, we have taken $n_{Ni}=1.61+i\cdot 2.4$ at 405nm, $1.76+i\cdot 3.21$ at 543.5nm, $1.97+i\cdot 3.75$ at 633.3nm and $2.49+i\cdot 4.39$ at 800nm [Weaver 1997].

Note that the calculated efficiencies are much higher than the measured ones. Indeed, due to the divergence of the light beams as well as the stray light (induced by the surface roughness), the detector's sensible area was too small to gather all the diffracted light. In other words, due to the surface roughness resulting from the fabrication process and the beam divergence, the diffracted light orders result in a light cone. Although most of the light is concentrated in the center, a large part passes beside the useful detector area.

5.3 High efficiency fan-outs

Fan-out gratings are phase elements that divide an incoming beam into an array of light beams having equal intensity. These micro-optical elements can be found in devices like optical interconnects, parallel optical processing or multidetector systems, etc... Different types of fan-outs have been studied in the past. The design of the profile of these periodic gratings has been optimized for fabrication technologies such as multilevel microlithographic techniques [Mait 1990, Turunen 1990], or laser-beam writing [Herzig 1990, Prongué 1992, Gale 1995].

According to the specificities of the Fourier Synthesis (FS), that was developed during this thesis, see section 2.2.1 and section 3.2, we propose novel profiles for fan-outs with maximum possible efficiency and deviation angle. The key-points of FS, which is a holographic surface-relief origination technique, are: (a) the small period of the structures or small lateral size of a single feature (approximately the half of the recording wavelength), (b) the high accuracy in the periodicity, (c) the high depth to period ratios (the depth of field is practically infinite), and (d) the continuous smooth profiles that can be obtained.

If the period $\Lambda_{fan\text{-}out}$ of the fan-out structure profile is chosen as to use the propagating orders as fan-out beams, the higher orders are evanescent and therefore carry no energy. Thus, the theoretical efficiency of the device is as high as possible, all the incoming energy being distributed in the useful orders. Note moreover that the unwanted reflected orders can be minimized by proper design. As a consequence, the deviation angle is close to 90°.

In the field of optical interconnects or integrated optics, the potential of such elements seems tremendous. In stacked optics, for instance, they could lead to short and compact components, which total length would be in the mm range. With FS, the period of the fan-out can be close to the wavelength it is conceived for, e.g. a recording wavelength of 413nm and a design wavelength of 633nm. Therefore, the fan-out elements can be designed to have very high efficiencies and very high deflection angles.

For binary computer-generated holograms or Damman gratings, studies have been realized by Vasara [Vasara 1991 and 1992]. The gratings were designed for the resonance domain, i.e. when structure period and design wavelength are of same magnitude.

If we consider surface-relief DOE’s with large deflection angles, the profile have usually to be very deep. Therefore, the ratio between period and depth has to be high to diffract a large part of the incoming energy into the higher orders (Energy/*m*, in the case of a 1 by *m* fan-out). The light interferences occurring in the volume, the depth of field of Fourier synthesis is practically infinite. In other words, the light intensity is invariant with the depth and thus is not a limiting factor to realize very deep structures.

We have focused on profiles with smooth continuous functions, the Fourier synthesis being ideally suited to originate such profiles. For the time being, the setup could only originate linear gratings, and thus the proposed fan-out functions are one-dimensional arrays of beams.

For DOEs having periods of several orders of magnitude larger than the design wavelength, many methods to improve the phase function have been developed such as the Iterative Fourier Transform Algorithm (IFTA) [Gerchberg 1972, Wyrowski 1990, Eismann 1989] or the non-linear optimization by Simulated Annealing (SA) [Kirk 1992, Kirkpatrick 1983]. Such algorithms cannot be straightforwardly applied to our case. Indeed, scalar theories based on the Fourier transform are not valid if the period of the diffractive elements is in the order of the wavelength.

Therefore, rigorous diffraction theories were used to determine the efficiencies of the propagating orders in combination with a minimization algorithm optimizing iteratively the profile with respect to the desired optical function. The starting point of the optimization process is a periodic profile form with an arbitrary number of Fourier components. The minimization algorithm optimizes the amplitude of the Fourier components to adjust the calculated diffraction efficiencies to the desired efficiencies. In other words, the efficiencies of the diffracted orders by the profile (which parameters are the Fourier components) are iteratively adjusted until they correspond to the desired efficiencies within an arbitrarily chosen tolerance.

We considered a 1 to 5 fan-out DOE in resist ($n_{resist} = 1.68$) which works in transmission and for normal incidence. The design wavelength was $\lambda = 633$nm and the polarization was TE. To have five propagating orders, the period of the fan-out $\Lambda_{fan\text{-}out}$ has been set to 2.9λ, therefore 1835.7nm. This corresponds to a maximum light deflection of 43.6° measured from the normal axis. The efficiencies of the diffracted orders, that is, the parameters for the calculation, were set to 1/5 for the transmitted beams and to 0 for the reflected ones. The profile structure was optimized for a number of three Fourier components. Figure 5.10 shows two different calculated profiles for the transmission 1 to 5 fan-out.

The calculated diffraction efficiencies in case (a) are 0.1996, 0.201, 0.1910, 0.201 and 0.1996 for the transmitted orders –2 to 2, respectively. The theoretical efficiency of the profile is 0.9941 with a standard deviation of 0.004%.

In case (b), the calculated diffraction efficiencies are 0.194, 0.196, 0.2, 0.196 and 0.194 for the transmitted orders –2 to 2, respectively. The theoretical efficiency of the profile is

0.9813 with a standard deviation of 0.14%. For comparison, calculations for a binary 1 to 5 fan-out resonance grating reports an efficiency of 93.8% and standard deviation of 1.2%, for grating parameters $\Lambda_{fan\text{-}out} / \lambda = 2.73$, $H_{fan\text{-}out} / \lambda = 0.82$, and a refractive index of $n_{fan\text{-}out} = 1.5$, see [Vasara 1992].

Note that the diffracted orders in reflection have been optimized as well. At worst, the reflection coefficient does not exceed 0.9%, that is, the 0th reflected order of the structure in (b). Therefore, the structure profile acts as a 1 to 5 fan-out and as an antireflection coating as well. Figure 5.11 (a) shows the distribution of the electric field for TE polarized light at normal incidence and for 633nm wavelength.

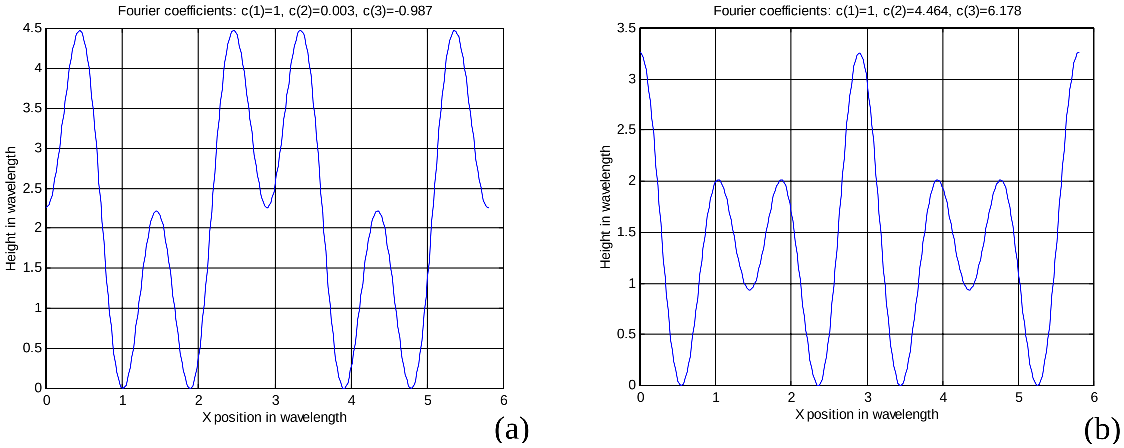

Figure 5.10. Optimized profiles for a transmission 1 to 5 fan-out synthesized with 3 Fourier components. The calculation have been done assuming normal incidence and a resist (n_{resist}=1.68) to air interface. In (a), the amplitude of the Fourier components are 1, 0.03 and –0.987 for c_1 through c_3, while in (b), they are 1, 4.464 and 6.178, respectively.

The incoming plane wave comes from the top of the graph, i.e. the resist side, and propagates downwards to the air. The black line represents the profile of the fan-out structure and therefore the interface between both mediums. As one can see, the field is literally guided through the tips of the profile and concentrated as the field propagates to the extremities. Thus, the field strength is maximum at the tips end. On the other hand, the reflected wave is very weak (almost zero). Therefore, the unwanted back reflections at the interface are almost suppressed.

In Fig. 5.11 (b), a SEM picture of a realized structure in resist is represented. Note that we used a standard commercial positive resist (AZ4562). The fabrication with this kind of resist turned out to be very difficult as can be observed on the SEM picture. The vertical dimensions of the features, in particular the different height levels of the tips, are far from the theoretical profile. For instance, the height of the highest tip should have had 2.06μm in theory, whereas the realized one has only approximately 700nm.

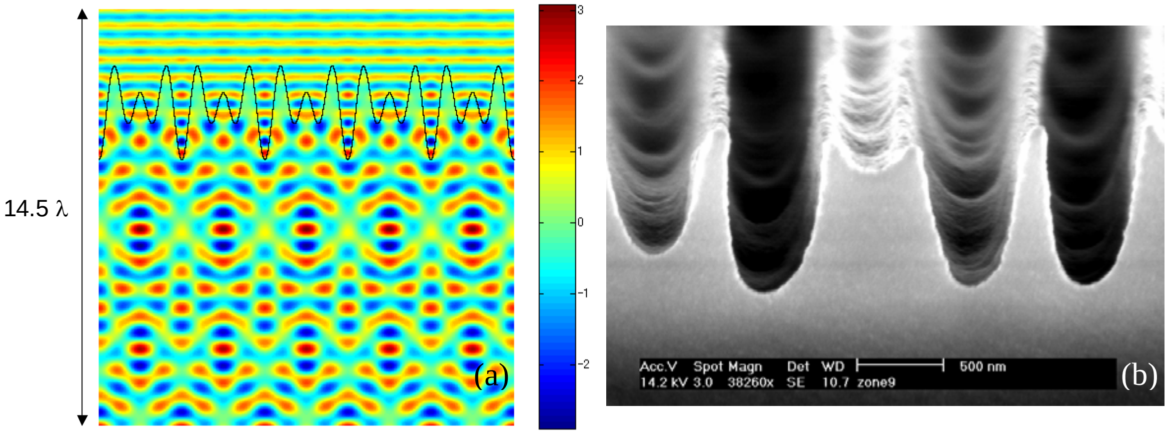

Figure 5.11. In (a), E-field distribution for TE polarized light and for five structure periods each 2.9λ wide. The calculations are done for a grating with a surface profile as shown in Fig. 5.10 (b). Note that the propagation of the wave is downwards and that the refractive index is 1.68 (resist) above and 1 (air) below the interface.
In (b), SEM picture of a realized fan-out profile in resist.

By examining the effects of fabrication errors on the theoretical profile, it turns out that a variation of 5% on the total height (~1.9μm instead of the optimum 2.06μm) results in a 3.26% drop in efficiency (0.951 efficiency instead of the optimum 0.982). In the case of a 10% error rate, the efficiency drop is 11.36% (0.854 efficiency instead of 0.982).
Indeed, this kind of resist type does not meet the requirements for the fabrication of such a very demanding profile. The lateral resolutions as well as the aspect ratios that can be achieved with positive resists are to low for features less than a micron. Negative resists may be better adapted to realize such profile shapes.
Noponen and Vasara [Noponen 1992] realized a binary resonance 1 to 7 reflection fan-out grating. The measured uniformity was approximately 11% for grating parameters $\Lambda_{fan\text{-}out}$ = 36.6μm (with a smallest feature size of 6.1μm), $H_{fan\text{-}out}$ = 2.68μm and a design wavelength of λ = 10.6μm.
As one can see, the fabrication of efficient and large deflection angle fan-out elements for the visible light remains a very challenging problem.

5.4 Summary

In this chapter, we presented nano-structures that can potentially be used as DOEs. These structures were originated by the FS technology introduced in section 2.2.2 and 3.2.

Blazed gratings with efficiencies as high as 58.5%, i.e. 93% of the theoretical efficiency, were realized in the form of saw-tooth profiles. The period of the structures was as small as 2.2µm. To approximate the ideal saw-tooth function, the profiles were synthesized by exposing 10 Fourier components which has never been done before. Therefore, we have realized saw-tooth profiles in a range of periods and accuracy in the profile form that had never been reached.

Linear arrays of retro-reflectors with periods in the range of 4µm were shown to be working for the entire visible spectrum. The shape of the periodic profile consists in prisms with an apex angle of 90° and were realized by exposing 10 Fourier components in addition with an iterative exposure adaptation technique, as described in section 4.4. Here again, we have realized well-known structures in a range of periods and accuracy in the profile form that had never been reached.

Finally, fan-out elements with very high efficiencies (theoretically as high as the maximum possible efficiency for fan-outs) and large deflection angles were investigated. We have proposed two types of profile forms to obtain a 1 to 5 fan-out DOE in transmission. Note that the profile has been designed to suppress back reflection at the same time. The realization of the profile has been shown to be very difficult with today's positive resists. The FS technology was not the limiting factor.

To summarize, we have shown three kinds of structures, of which dimensions and profile forms as well as the size of the structured areas (4-10mm^2) demonstrate the great potential of the FS technology developed during this thesis.

CHAPTER 6

MICROSTRUCTURES FOR VISUAL APPLICATIONS

In this chapter, we study diffractive micro-structures designed for optically variable devices (OVD) for visual document security against counterfeiting. Their applications can be found on valuable documents such as banknotes, creditcards or passports. The european (euro) or the swiss banknotes, for instance, include OVD's, aka Kinegram [Moser 1996, Moser 1998, Staub 2000], in the form of a metallic sticker where various shapes, numbers or images appear in different colors when changing the viewing angle. Their optical properties or visual effects are designed to be easily verified by the naked eye. As a consequence, the optical diffraction effect is optimized for the visible spectrum, i.e. within a wavelength range from 400 to 800 nm. In most cases, machine readability is also required or at least desirable. Furthermore, in addition to the nice visual appeal, a hidden or secret feature is an asset. Examples include light effects that appear or disappear to the naked eye with the use of an analyzer, like a polarizer or a quarter wavelength plate, for instance. In the following, we present different kinds of periodic surface-relief structures exploiting color-shifting, as in [Gale 1998], and polarization properties that depend on the profile and the period of the structure [Watts 1997a and 1997b]. We consider the coherent superposition of two and more gratings without phase relation. Two options can be distinguished: the gratings have nearly the same frequencies, or the gratings have very different frequencies ($\Lambda_1 > 5\text{-}10\ \Lambda_2$).

In the first section, we look at structures with continuously varying profile depth [Tompkin 1999, Staub 1999] using the superposition of gratings which frequencies are very close. We use the moiré phenomenon as described in section 2.2.3 to produce periodic structures in one as well as in two dimensions. These have been shown to be very resilient against standard holographic copy techniques, because those techniques lead to a loss of fidelity in profile form and depth. Moreover, the moiré phenomenon can also be useful to hamper machine reading under circumstances. In our case, if the structures integrated in the OVD's have features in the geometry or in the period that are slightly off of the period of an array of detectors used to copy the OVD (such as a photocopier), the superposition of both patterns produces moiré fringes. The resulting copies have an inhomogeneous contrast that can be immediately identified by the naked eye. These detector arrays have typically a period of a few hundreds of micrometers, which is optimally suited to our fabrication processes. Indeed, complex moiré patterns in one as well as two dimensions can be synthesized easily.

In the second section, we investigate the combination (or superposition) of a large grating and a fine grating. The period of the large grating (5-10µm) is several orders of magnitude larger than the visible range of light. On the other hand, the period of the fine grating is in the order of magnitude of the wavelength period of the visible light (300-800nm). The structures resulting from the combination of both gratings exhibit interesting polarization properties that can be used as secret features. For instance, elements of the OVD like a letter or a number that appear or disappear with the use of an analyzer, such as a polarizer or a quarter-wave plate.

6.1 Gratings with continuously varying profile depth

Usually the effectiveness of an OVD is increased by ensuring the uniformity of a grating over an entire design element. This is while each design element, e.g. an image, letter, line or area, appears brightest and sharpest when the profile form, depth and orientation are optimum throughout. Indeed, outstanding OVD's distinguish themselves by the uniformity of the gratings throughout a design element as well as by the sharpness of the transition from one design element to the juxtaposed elements. It is beyond contention that uniform gratings should be aimed for throughout a design element in standard OVD's, however, we have discovered that by varying the surface-relief profile locally in a predefined manner, it is possible to create novel optical effects which are resilient against imitation and easy to authenticate. We present two examples of such structures. The first is a linear subwavelength or zero-order grating with varying profile depth and the second, a two-dimensionally varying profile depth grating with a grating period sufficiently large to have propagation of the 1st diffraction order. In both cases, the structure profile is produced by the beatings of the grating's superposition; the gratings have very near frequency and/or orientation.

6.1.1 Linear subwavelength grating

A high-frequency, linear surface-relief grating of locally varying depth can result from the superposition of two linear gratings of uniform depth, where the periods of the basis gratings differ slightly. Figure 6.1 shows a SEM picture of such a grating realized in photoresist.

The resulting surface profile can exhibit a relatively large-period modulation in profile depth and, thus, in diffraction efficiency. This periodic variation in diffraction efficiency yields a typical moiré pattern (in our case stripes), which is seen altering as the interrogation conditions are varied. For high-frequency gratings this effect is seen in the zero-th diffraction order, while for larger period gratings, moiré patterns can be observed in both the higher as well as the zero-th diffraction orders.

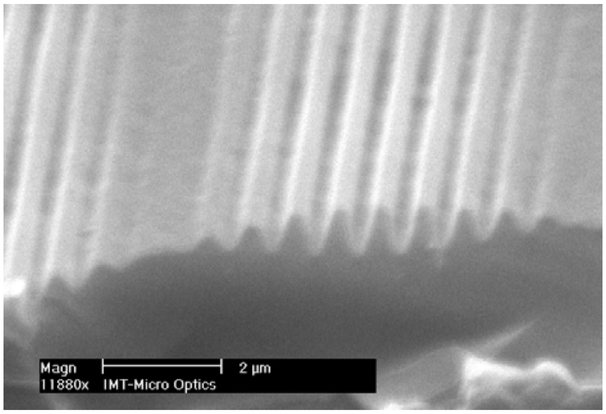

Figure 6.1. SEM picture of a fabricated structure in photoresist using two-beam interference lithography. The sub-grating has 800nm period and a modulation of about 8μm. Note that the structure seems not flat, but curved (in particular when looking at the left side). That is an effect of perspective due to the breaking of the sample which is not homogeneously flat.

Previous studies of first-order gratings of locally varying depth or profile form have demonstrated two principal benefits [Tompkin 1999, Staub 1999]. Firstly, such combinations of gratings are useful for the study of diffraction properties of a class of profiles. For example, a single sinusoidal grating of locally varying depth eliminates the need for the toilsome realization of a series of uniform sinusoidal gratings of various depths. Secondly, such combination gratings are interesting in their own right as potential visual security elements.

We have combined experimentally two high-frequency, zero-order sinusoidal gratings of approximately equal period and profile depth to form a grating in which the depth of the zero-order sinusoidal profile varies slowly with respect to the position on the structured surface. Note that we call zero-order gratings, gratings with periods that are much smaller than the period of the light. Therefore, all diffracted orders are evanescent and only the zero-th order propagates. As the gratings are intended for the visible range of light, the period of the zero-th order gratings has to be less or equal to 400nm in our case. The two zero-order gratings which have been combined can be described as $f_1(\boldsymbol{x}) = A\cdot\cos(\boldsymbol{k_1}\cdot \boldsymbol{x})$

and $f_2(\boldsymbol{x}) = A\cdot\cos(\boldsymbol{k_2}\cdot \boldsymbol{x})$, with $|\boldsymbol{k_1}| = 2\pi/\Lambda_1$ and $|\boldsymbol{k_2}| = 2\pi/\Lambda_2$. Λ_1 and Λ_2 are the grating periods and x is a displacement vector. Both gratings are parallel ($\boldsymbol{k_1} // \boldsymbol{k_2}$) and the superimposition can be written as:

$$f(\boldsymbol{x}) = f_1(\boldsymbol{x}) + f_2(\boldsymbol{x}) = 2A + 2A\cdot\cos\left(\frac{\boldsymbol{k_1}+\boldsymbol{k_2}}{2}\cdot\boldsymbol{x}\right)\cdot\cos\left(\frac{\boldsymbol{k_1}-\boldsymbol{k_2}}{2}\cdot\boldsymbol{x}\right) \tag{6.1}$$

Thus, the resulting grating described by $f(\boldsymbol{x})$ has a spatial period of $\Lambda = |\Lambda_1\Lambda_2 / \Lambda_1+\Lambda_2|$, which is related to the average $\frac{1}{2}(\boldsymbol{k_1}+\boldsymbol{k_2})$ of the spatial k vectors of the two basis profiles. The maximum profile depth of the combination grating is $h = 4A$ and the modulation in height can be characterized by the distance L_{mod}, which is half the beat period $\Lambda_{beat} = |\Lambda_1\Lambda_2 / \Lambda_1-\Lambda_2|$.

Figures 6.2 to 6.5 show some results for such a combination zero-order grating of which the profile height varies periodically. The resultant grating had a mean period Λ of ca 300 nm and the height was modulated with a period L_{mod} of 8 mm. Using an AFM and an scanning electron microscope, we measured the profile form as a function of position. Figure 6.2 shows a plot of the measured profile height as a function of position together with the envelope of heights as predicted by the equation for f.

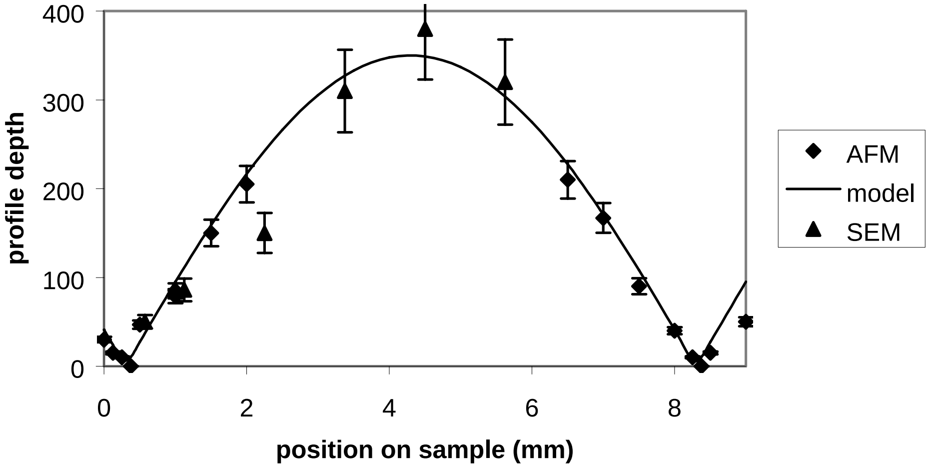

Figure 6.2. Profile depth as a function of position for the zero-order grating of locally varying depth. The triangles are the depths determined by measurements using the electron microscope while the diamonds are the measurements using the AFM. The solid line is a calculation for the depth.

Note that for the deepest profile depths, the AFM was unable to determine the accurate depth or form, owing to the finite angle (approximately 45°) of the tip of the AFM. From the measurements of the scanning electron microscope, we determined that the maximum profile depth $h = 4A$ is approximately 350nm. From the AFM measurements, the profile form was determined using a least-square fit.

In Fig. 6.3, the SEM pictures illustrate the change in shape of the grating profile for different positions along the grating. As one can see, the shape is sinusoidal when the profile height is small and become U-shaped for higher profile heights. Therefore the profile becomes steep and cannot be measured accurately by an AFM. Note that the diffraction behavior of a sinusoidal profile and the realized profile are very similar in that range of depths (about 300nm) and grating periods (about 300nm).

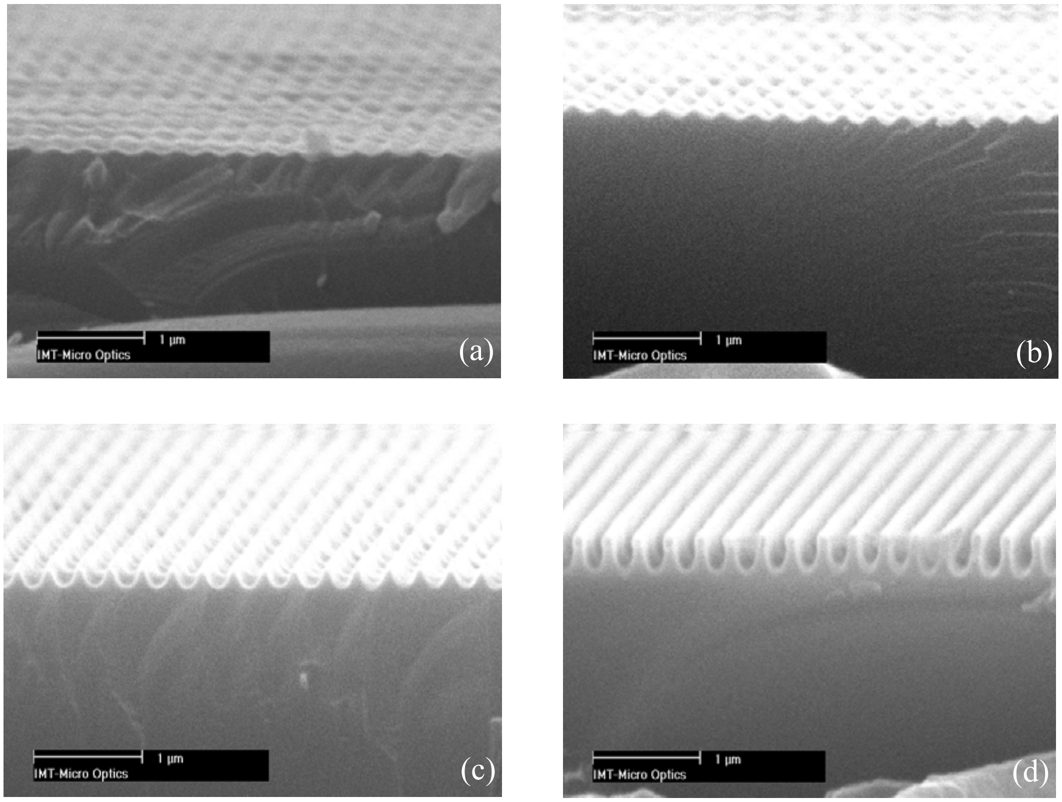

Figure 6.3. SEM pictures of a zero-order linear grating in resist with varying depth at different positions. The height of the profile is increasing from about 30nm to about 350nm, which corresponds to the maximum height, through (a) to (d) respectively. Although the illuminated profile is sinusoidal, the grating becomes U-shaped with increasing height profile due to the resist's response. Note that the profile as shown in resist is then transferred into a nickel shim by electroforming.

Figures 6.4 (a) and (b) show plots of the theoretical diffraction efficiency for a zero-order linear grating as a function of grating depth and wavelength. In the case of TE polarization, the efficiency remains almost constant for all depths and for the whole range of visible light while for TM, it is very sensitive to the grating depth.

This fundamental difference is born out by the experimental data and by the visual effects which the grating demonstrated, e.g. Fig. 6.5 (a) and (b). The realized high-frequency gratings were visually interesting, even when viewed under natural illumination, such as sunlight.

The moiré pattern is seen to alter as the sample is tilted. When the grating is viewed with a linear polarizer used as an analyzer, the stripes of the moiré pattern are seen to change markedly as the polarizer is rotated, as can be seen by comparing Fig. 6.5 (a) and (b). Indeed, the moiré pattern disappears when the linear polarizer is oriented for TE polarization, because its zeroth-order diffraction efficiency is essentially constant as a function of grating depth. Therefore the sample appears homogeneous with TE polarized light due to the constant diffraction efficiency throughout the wavelength range and profile depth.

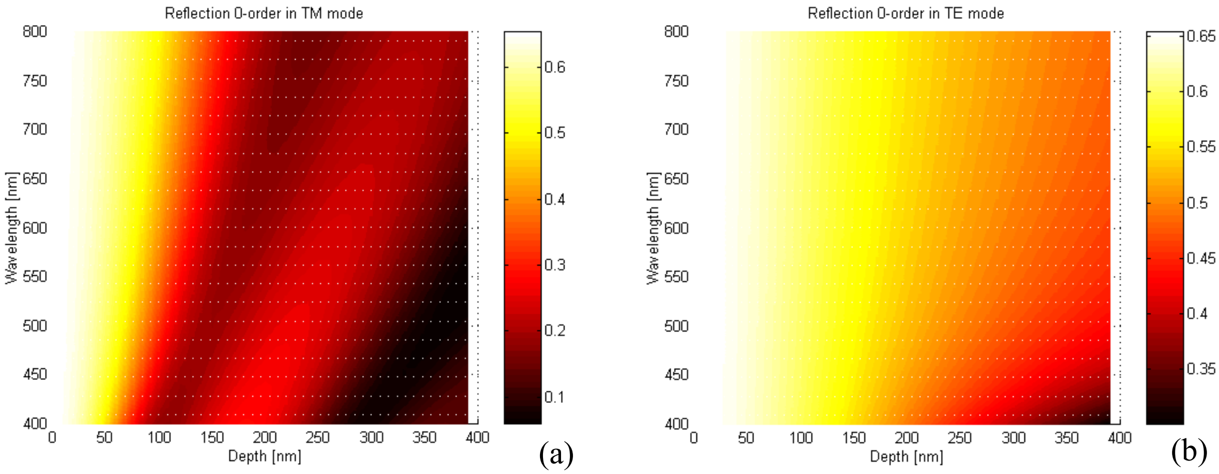

Figure 6.4. Calculated reflection of a zero-order metallic grating (nickel) as a function of depth and wavelength. The diffraction efficiencies for TM (a) and TE (b) were calculated assuming a normal incident beam, by the use of rigorous diffraction theory. Note that the diffraction efficiency scales are different; in (b) it begins at 0.3.

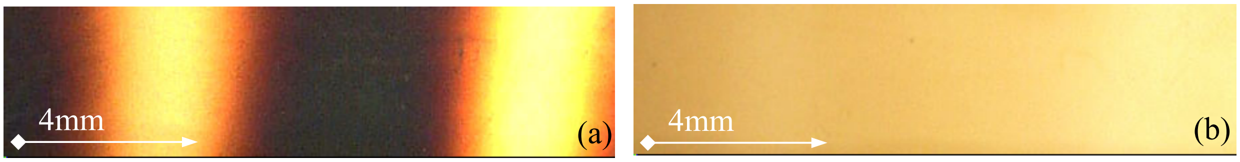

Figure 6.5. Photographs of a realized sample of a grating with varying profile depth in nickel observed under white light for illustration of the visual effect. In (a) and (b) the polarization of the light is TM and TE, respectively. The spacing between the moiré stripes is approximately 8mm.

6.1.2 Grating with beatings in two dimensions

In our second example, we combined three sinusoidal gratings, in an arrangement as shown in section 2.2.3, Fig. 2.9 (a). The superimposition of the three gratings produces a large periodic two-dimensional moiré pattern with nodes were the height of the profile is maximum and antinodes were the height is almost zero. The period and orientation of the gratings have been chosen as to obtain large hexagonal cells of about 2mm dimension for the moiré pattern. The resulting structure is a linear grating of about 1 micrometer period whose depth varies continuously in all directions over the sample from about 30nm at the borders of the cells, to 1.8-2 micrometers at the center of the cells.

Figure 6.6 shows rigorous calculations for the reflection of the 0-order and 1-st order diffraction of a linear metallic grating with 1µm period for different depths and wavelengths. The incident light is normal to the sample, and polarized in TM for (a) and (c) and TE for (b) and (d).

Looking at the simulations for the reflected 0th order in (a) and (b), one can observe that the reflection in TM polarized light is almost zero for a large range of the visible spectrum and grating depth while the reflection in TE is strongly affected by the grating depth. The diffraction figures for the 0th and 1st order are similar, but the efficiencies are much lower for the 1st order diffraction. The reflection coefficient is oscillating between zero and local peaks as the depth changes. Note that those efficiency peaks decrease as the grating becomes deeper and note also that they are not very sensitive to the wavelength. This fundamental difference between TM and TE diffraction can be observed in the pictures of the realized gratings shown in Fig. 6.7 (a) and (b).

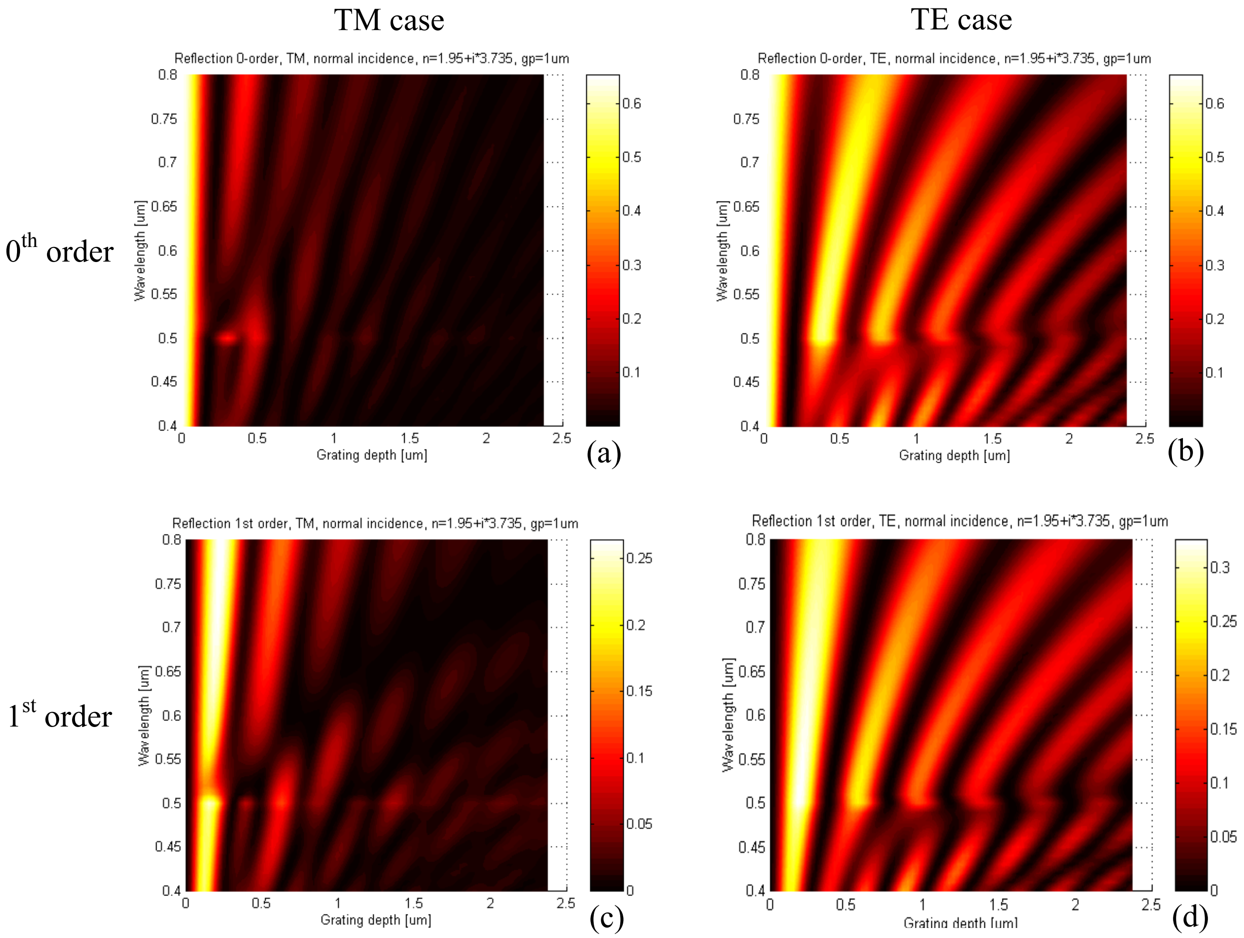

Figure 6.6. Numerical calculations of the diffracted 0^{th}, (a) and (b), and 1^{st}, (c) and (d), orders in reflection of a metallic (nickel) sinusoidal grating of 1 μm period for various wavelengths and depths. The incident light is normal to the grating. The polarization is TM for (a) and (c), and TE for (b) and (d). The calculations were done using rigorous diffraction methods.

The pictures were taken through a polarizer with natural white light illuminating the sample at normal incidence. The moiré pattern is clearly seen to alter as the polarization changes. In TM mode, the moiré pattern seems blurry, and therefore the contrast of the moiré pattern throughout the sample is weak. In TE mode, on the other hand, strong local variations in intensity can be observed in the form of an alternation of bright and dark ellipsoids around the center of the cells. Each ellipsoid corresponds to a lobe of local maximum diffraction efficiency as shown in Fig. 6.6 (b). The ellipsoid's contrast is highest at the borders (in dotted lines) and vanishes at the center of the cells. Indeed, the local diffraction maxima are higher for the shallow grating depth (at the borders of the cells) and diminish as the grating becomes deeper (at the center of the cells).

The color also alters with polarization, the moiré pattern appearing yellowish in TM and blueish in TE mode (pictures on the cover). Note that, as several diffracted orders propagate, the colors are not spectrally pure.

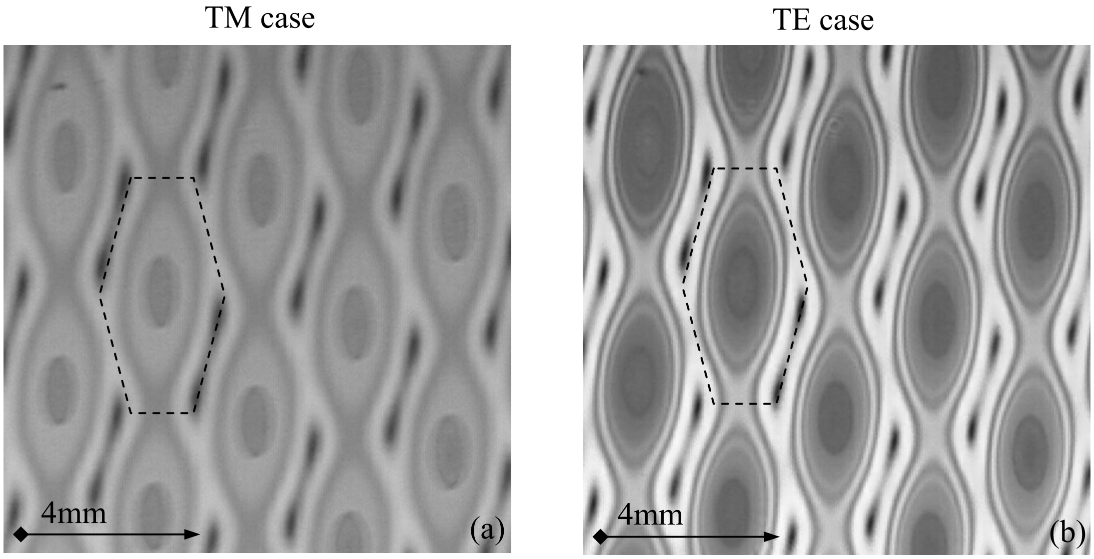

Figure 6.7. Pictures of a metallic grating realized with three sinusoidal gratings under TM (a) and TE (b) polarization. The 1μm period linear grating is slowly modulated from 30nm to 2μm depth by a hexagonal pattern (as suggested by the dotted lines) which cells are 2mm in dimension. The maximum depth is located at the center of the cells (dark circles), while the minimum depth is at the borders (darker lines). Note that due to fabrication errors (on the recording angles), the cells are not absolutely symmetric. Ideally, the black lines should be all over the cell, outlining a hexagon.

6.2 Combination gratings

In this subsection, we will consider the case where a singly-periodic zero-order diffraction grating is superposed to a singly-periodic, large-period diffraction grating that we will call a combination grating. For the case where the surface-relief gratings, described by the functions $f_1(x,y)$ and $f_2(x,y)$, are combined [Staub 1996 and 1998], the resultant surface-relief profile is described by $f_3(x,y)= f_1(x,y)+ f_2(x,y)$.

We consider the case where one basis grating $f_1(x)$ is a large-period linear grating of moderate depth. Such gratings, where the period is much greater than the wavelength of light and where the depth is much less than the wavelength of light, are typically polarization independent, that is, the diffraction efficiency is identical for all polarization states. To this large-period grating we combine a zero-order grating, described by $f_2(x,y)$. As we have seen in an example in section 6.1.1, Fig. 6.4, the diffraction characteristics of zero order gratings show a typical high dependence in relation to the polarization state of the incident light. The experiments we have performed have focused on determining the effect of the zero-order grating f_2 on the diffractive properties of the large-period grating f_1, through a study of the combination grating f_3.

Within scalar theory, the diffractive properties of superposed gratings can be determined by the convolution of the amplitude distribution of the individual gratings. In the case of crossed gratings, this reduces to a simple multiplication. The intensity in the (m,n) order is proportional to the multiplication of the intensity of the order m of grating f_1 and the intensity in the order n of grating f_2. The equivalence theorem holds that this rather simple approach can provide a reasonable description of the intensity distribution of superposed gratings, even when the simple scalar theory is not applicable [Goodman 1996]. Our experiments have actually demonstrated that the equivalence theorem cannot straightforwardly be applied to the case of a combination of a large-period grating with a zero-order grating. Indeed, the properties expected by naively applying the equivalence theorem, namely that the polarization properties of the zero-order grating can be straightforwardly multiplied with diffraction efficiency of the first-order grating, would be met for a very narrow range of depths. In the following, we will consider the case where the large grating is a rectangular or binary function and the case where it is a sinusoidal function, the fine grating being a sinusoidal function in both cases.

6.2.1 Combination of a rectangular and sinusoidal grating

In that subsection, we consider the superposition of a large-period Λ rectangular or binary grating f_1 having a depth smaller than the wavelength of incident light λ, that is, the period is much greater than λ and the depth is less than λ. This grating is a purely scalar grating. To this grating we combine a zero-order grating f_2 with a period of approximately 300nm and a depth of approximately $\lambda/(2n)$; such zero-order gratings have very different diffractive characteristics for TE polarized light (where the electric field vector is parallel to the grating grooves) and for TM polarized light (where the electric field is perpendicular to the grating grooves).

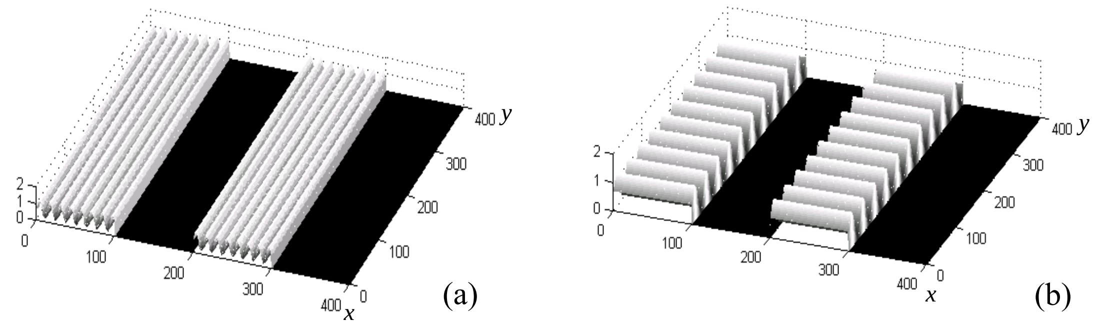

Figure 6.8. Schematic of the geometry of an ideal combination grating f_3 where f_1 is a large period rectangular grating and f_2 is a fine period sinusoidal grating. In (a), f_1 and f_2 are parallel and in (b), f_1 and f_2 are perpendicular. The scales are in arbitrary units.

Figure 6.8 shows a schematic of the combined gratings. Note that the bottoms or valleys of the combination grating are flat, therefore

$$f_3 = \begin{cases} f_1 + f_2, \text{for } x = 0 \ldots \Lambda/2 \\ 0, \text{for } x = \Lambda/2 \ldots \Lambda \end{cases}.$$

The precise depths of both the large-period rectangular and zero-order basis gratings were optimized as to achieve highest contrast between TE and TM. Rigorous diffraction calculations were applied to the case of the combination grating where the k-vectors of the two basis functions are parallel (that is, the grooves of f_1 and f_2 are parallel). Following the calculations, we have experimentally combined a large-period rectangular grating and a high-frequency, zero-order grating. Firstly, we combined the gratings for the case where the two basis gratings have parallel k-vectors. Secondly, we used the same basis gratings, yet rotating the zero-order grating by 90° with respect to the large-period grating. Therefore, we have combined the two gratings where the k-vectors are orthogonal, that is, the resulting grating is a crossed grating. Figure 6.9 shows AFM measurements of the realized structures in metal (nickel). The corresponding experimental diffraction efficiency measurements can be found in Fig. 6.10. The total height of the structure is about 320nm and the depth of the fine grating about 200nm. The periods of the large rectangular grating and the fine sinusoidal grating are about 5µm and 300nm, respectively.

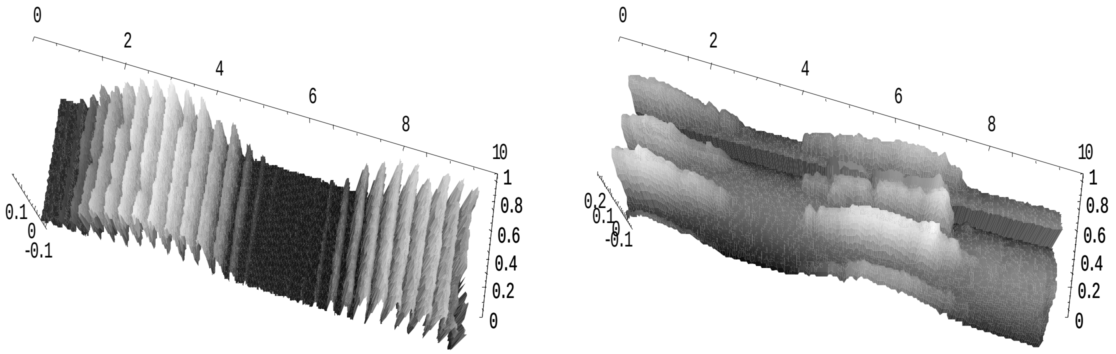

Figure 6.9. AFM measurement of a combination grating in metal of a large rectangular grating and a fine sinusoidal grating. Due to fabrication errors, in particular because of the mask-lithography process, a rounding at the edges of the binary structure can be observed. Therefore, the height of the fine sinusoidal grating is not homogenous at the borders of the binary features.

The fabrication of these structures was carried out in three steps. First, the binary grating was exposed in a layer of resist using mask-lithography as described in section 2.1. The fine grating has then been uniformly exposed over the sample by a two-beam interference setup described in section 3.1. After a development process, the structure's profile (that were still in resist) has been transferred into a nickel shim by electroforming.

Figure 6.10 (a) shows some typical measurements in reflection of the experimentally realized combination grating in metal. The measurements were made using a beam of helium-neon laser (632.8 nm), which was normally incident to the sample. Note that the incidence angle is not exactly normal, but at an angle of 0.5° to avoid that the detector crosses the incoming beam of light, the measurements being done in reflection. For comparison, theoretical calculations of the ideal structure are shown in Fig. 6.10 (b). Rigorous diffraction theory was applied for nickel at 633nm wavelength and normal incidence. Although the diffraction efficiency for the large-period rectangular grating are purely scalar, we can see in Fig. 6.10 that the combination grating cannot be described by scalar theory. The experiments show that by superposing a zero-order grating so that the k-vector is parallel to the large-period grating, the higher diffraction orders have a much greater efficiency for the TE polarization (that is, the TM polarized light is not diffracted by the grating). Similarly, when the zero-order grating is superposed so that its k-vector is perpendicular to the large-period grating, the higher diffraction orders have a much greater efficiency for the TM polarization (that is, the TE polarized light is not diffracted by the grating). Note that the diffracted light, in TE as well as TM mode, is concentrated in the orders 0 and 1, the light diffracted in the higher orders being almost zero. Therefore, the maximum observation angle for the visual effect corresponds to the first diffracted order, therefore an angle of 9.1°. Thus, we have experimentally demonstrated that it is possible to design a combination grating so that the orientation of the zero-order basis grating dominates the polarization properties of diffraction of the combination grating.

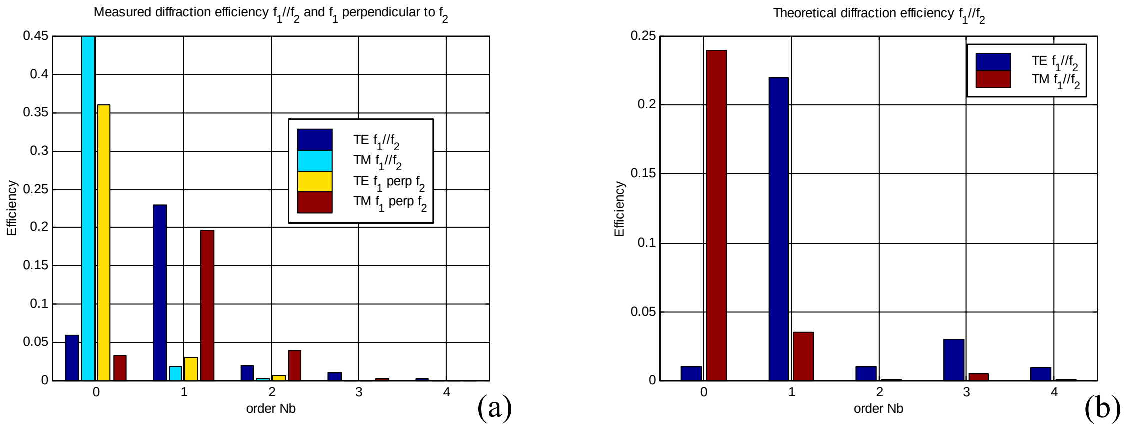

Figure 6.10. Efficiency in reflection of the diffracted orders of a large 5µm period rectangular grating combined with a 300nm zero-order grating in nickel. In (a), measurements of the diffraction efficiency of the realized structures as shown in Fig. 6.9, and in (b), numerical calculations of an ideal structure as shown in Fig. 6.8 and with the optimal height, assuming 633nm light at normal incidence.

6.2.2 Combination of two sinusoidal gratings

As a further example of the combination of a large-period grating with a zero-order grating, we consider the superposition of a large sinusoidal grating with a zero-order grating where the k-vectors of the two gratings are parallel. The depths of the two basis gratings were optimized by applying rigorous diffraction theory to the combination grating to maximize the polarization difference between TE and TM.

Based on the calculations, the gratings were realized with the optimum heights and periods, therefore 450nm and 4µm, respectively, for the large sinusoidal grating and 333nm and 185nm, respectively, for the zero-order grating. Using the same grating parameters, we also realized combination gratings where both sinusoidal gratings are crossed at right angle.

Figure 6.11 show AFM measurements and SEM pictures of the realized structures. The fabrication of the structures was done by exposing both gratings sequentially using two-beam interference lithography as described in section 2.2. After having been developed, the structure's profile was transferred into a nickel shim by electroforming.

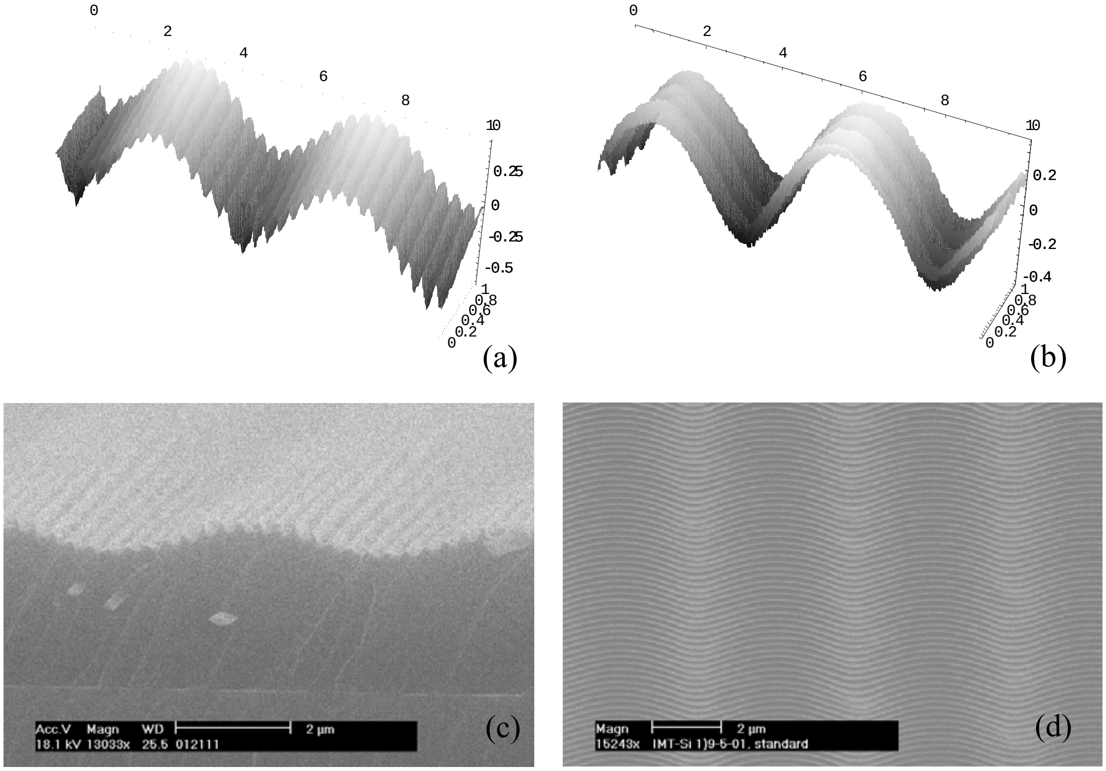

Figure 6.11. Realized combination gratings with a large sinusoidal grating and a zero-order sinusoidal grating. Both gratings are parallel in (a) and (c), and perpendicular in (b) and (d). (a) and (b) are AFM measurements while (c) and (d) are SEM pictures. Note that the picture in (d) was taken obliquely to the sample surface.

The diffraction efficiency measurements in reflection for the realized combination gratings in metal are shown in Fig. 6.12. The gratings were illuminated by a HeNe laser at near normal incidence. The large-period basis grating was polarization independent. By combining a zero-order grating to this grating, we have realized a combination grating where TE polarized light is diffracted with much greater efficiency than TM polarized light. Also shown in Fig. 6.12 (b) are the theoretical calculations, which were made using rigorous diffraction theory at 633nm and normal incidence, for an ideal combination grating where the basis gratings are parallel. Note that the theoretical and the experimental data agree very well. In the case where the gratings are perpendicular, the situation changes and the TM polarized light is diffracted with higher efficiency than TE. Note also that the diffraction efficiency of the light is distributed across all orders and is maximal for the 4^{th} order. Therefore, the visual effect can be seen by the naked eye for large observation angles too (approximately 52° from the normal of the sample if we consider order 5 as being the maximum visible order). Thus, we achieved to modify the polarization properties of a large period scalar grating by the superposition of a zero-order grating. The direction of this last one determines the polarization properties of the combination grating.

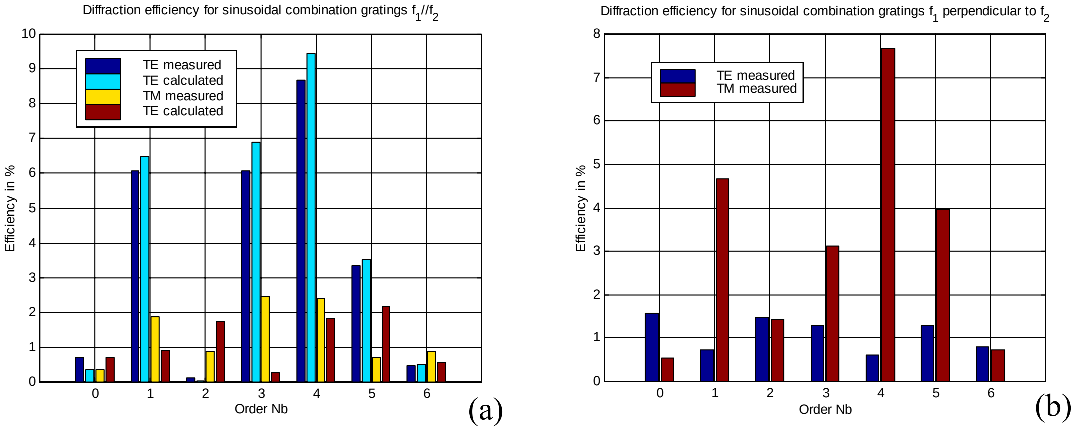

Figure 6.12. Efficiency measurements in reflection of the diffracted orders of a metallic combination grating. Two sinusoidal gratings of 4μm and 333nm period are superimposed to form the combination grating; they are parallel in (a) and orthogonal in (b). Furthermore, in the parallel case (a), numerical calculations of the ideal structure's diffraction efficiencies are presented for comparison.

6.3 Summary

In this chapter, we have presented nano-structures designed specifically for visual security applications. Periodic structures with continuously varying depth were shown as to have interesting color as well as polarization properties that vary with the viewing angle, resulting in spectacular visual effects. These structures exploit the moiré phenomenon to influence the local height of the grating profile and thus the local diffraction efficiency.

Combination gratings, therefore gratings that combine a large scalar grating ($\Lambda >> \lambda$) with a zero-order grating ($\Lambda \leq \lambda$) were shown to have polarization properties that are determined by the zero-order grating direction. With heights and periods properly optimized, the realized combination gratings diffract only TE light when both gratings are parallel and only TM light when the gratings are perpendicular. That polarization effect can be used to let appear or disappear elements of an OVD with the use of a specific analyzer. In our case, the analyzer is a polarizer. Thus, in addition to the nice eye-catching effects of a standard grating, the light diffraction properties of the structures include a secret feature in polarization.

CHAPTER 7

SUMMARY AND CONCLUSION

When it comes to get large areas of structured surfaces that have to be spatially coherent and moreover with structures, which lateral dimensions are in the range of a few microns to hundreds of nanometers, technologies using laser light interference can play all their assets. Generally, these technologies are regrouped under the name of interference or holographic lithography. The assets of interference lithography consist in the large structured surfaces that can be obtained, the wide period range (in our case ~220nm to ~10µm at 413nm recording wavelength) of the structures, the accurate periodicity and coherence of the structured surfaces, and the effectively infinite depth of field of the optical recording. Other technologies, like e-beam lithography or scanning focused laser beam lithography, can be used additionally to introduce lines of defects or singular features, for instance.

In the frame of the present thesis, the major part of the work has been concentrated on the interference lithography technologies as well as the nanostructures that it can produce.

Although a wide variety of structure profiles have already been realized and published in the literature, arbitrary profile shapes are difficult, and sometimes impossible, to realize with interference lithography. However, we presented a novel technology that allows to expose arbitrary profile shapes. We applied the so-called Fourier Synthesis (FS), which is based on the decomposition of periodic functions in Fourier series. The method is only limited by the number of Fourier components that the exposure system can produce and by the properties of the recording material. Fabrication errors and in particular the accuracy on the recording angle of the interfering beams limits the maximum area size of the useful realized grating structure. To describe the limitation, we introduced a spatial coherence length for the structures. This value gives an approximation for the effective structured area for which the structure profile can be considered invariant. For a structure period of 3µm, and an error on the incidence angle of 10^{-3} degrees, the coherence length is 1.5mm resulting in a useful square surface of 2.25mm^2.

The Fourier synthesis technique has already been investigated in the past, with more or less success due to technical difficulties. The literature reports structures realized with two Fourier components. During this thesis, a novel setup that allows the superposition of a large number of Fourier components has been developed. This setup is derived from a Loyd's mirror geometry and includes elements to precisely set the phases as well as adjust the harmonic numbers between the exposed Fourier components. The accuracy on the Fourier component's position is less than 10nm and its influence on the phase depends on the component's period. The precision on the Fourier number is related to the error on the angle of incidence of the interfering beams. We achieved 10^{-3} to 10^{-4} degrees, depending on the profile form and period of the profiles, which corresponds to useful structured areas of approximately 2 to $20mm^2$.

Three examples were presented to show the potential of FS. Blazed optics in the form of saw-tooth profiles with 2.2μm period and 58.5% efficiency, i.e. 93% of the theoretical efficiency for a 633.3nm wavelength, were realized by exposing 10 components. In our second example, we realized one-dimensional retro-reflectors with 4.4μm period by exposing 10 components. And in our last example, profiles for a 1 to 5 fan-out with very high efficiency and very large deviation angle were proposed. The design of these profiles exploits the fact that the fan-out orders are the propagating orders and at the same time suppresses the diffracted orders coming back from the resist to air interface. Therefore, these profiles have theoretically the maximum possible efficiency of 20% for each fan-out beam. However, the physical characteristics of the recording material hampered the realization of those demanding profiles.

A section has been devoted to the different aspects of the behavior of positive DNQ based resists. We gave a brief outline of the chemical reactions occurring in resist during each step of its processing. The development step showed up to be the most critical. To overcome the development effects, we developed an iterative method to adjust the illuminated spatial intensity profile with respect to the final structure, i.e. after development.

To improve the FS technology, two points come to the fore. First, the angular resolution of the exposure system should be increased. A precision of 10^{-5} degrees would result in a useful structured area of $150x150mm^2$. We made a proposition using a twin photodiode to adjust the angle of the system. Since the adjustment by the naked eye resulted in a 10^{-3} degrees resolution, the proposed solution seems promising to obtain angular resolutions 10 or 100 times better than at the time being. Furthermore, investigation in photosensitive materials should be done to exploit the unique specificities of that technology. These specificities are: (a) the smooth or in other words analog profiles that are obtained and (b) the high height to lateral size ratio features that could be achieved due to the infinite depth of field of interference lithography. Therefore, these materials should react sensitively to the illuminated intensity, that is have low contrast, and have physical properties that support high resolutions.

Nonetheless, we have shown the potential of this technology by exposing a large number of Fourier components never reached before. In addition to e-beam lithography or multiple chromium mask lithography, the FS technology could open new ways for the design of novel profiles in the nano-structuration of surfaces or in the design of DOEs.

To reduce further the period of the structures, we presented a setup based on a right-angled prism. The interferences occurring in glass ($n_{BK7} \cong 1.528$), the lateral period of the structures could be reduced to 160nm (the theoretical limit being 138nm) for a recording wavelength of 413nm. Linear gratings were successfully realized with that setup. However, due to reflections in the dense media, parasitic gratings are recorded at the same time as the main grating, reducing the potential height of the structure. An additional step, such as reactive ion etching, should be performed to increase the depth of the structures.

Optically variable devices (OVDs) for visual security against counterfeiting are applications where nano-structuring plays also an important role. The structured surfaces have to be large enough to be easily viewed with the naked eye. These devices have to be visually appealing and moreover have unique properties combining color effects, polarization effects and viewing angle to distinguish a genuine from a counterfeited OVD. Therefore, we investigated the moiré phenomenon to determine the different exposures necessary to create profiles which height vary spatially in a predefined manner. The resulting structured surfaces have one- or two-dimensionally locally varying diffraction properties with spectacular color and polarization effects. As a further application, we investigated the effect of a sub-wavelength grating ($\Lambda<\lambda$) superposed to a large grating ($\Lambda>>\lambda$). We achieved to realize gratings, which diffract light in a determined polarization state. Thus, in addition to the nice eye-catching effect of a standard grating, the diffraction properties include a secret feature appearing only with the use of a polarizer.

Looking at the recent trends in the industry and at the many applications that employ nano-structured surfaces, for instance, in next generation displays such as field emission flat panel displays [Chen 1996, Bozler 1994, Spallas 1995], or high density storage media [Ross 1999, Fernandez 1996], we think that the needs in nano-structures and nano-structuring tools will keep increasing in the future.

CHAPTER 8

REFERENCES

[Austin 1976] S. Austin and F. Stone, “Fabrication of thin periodic structures in photoresist: a model,” Appl. Opt., **15**, 1071-1075 (1976).

[Bartolini 1972] R. A. Bartolini, “Rapid Communications: Improved development for holograms recorded in photoresist,” Appl. Opt., **11**, ff:1275 (1972).

[Bartolini 1974] R. A. Bartolini, “Characteristics of Relief Phase Holograms Recorded in Photoresists,” Appl. Opt., **13**(1), 129-139 (1974).

[Beesely 1970] M. J. Beesely, J. G. Castledine, “The use of photoresist as a holographic medium,” Appl. Opt., **9**, 2720-2724 (1970).

[Blough 1995] C. G. Blough and G. M. Morris, “Diffractive / refractive lenses offer high performance at low cost,” Laser Focus World, **31,** (11), 67-74 (1995).

[Bozler 1994] C. O. Bozler, C. T. Harris, S. Rabe, D. D. Rathman, M.A. Hollis and H. I. Smith, “Arrays of gated field-emitter cones having 0.32 μm tip-to-tip spacing,” J. Vac. Sci. Technol., B**12**, 629 (1994).

[Breidne 1979] M. Breidne, S. Johansson, L-E. Nilsson and H. Ahlen, “Blazed holographic grating ,” Opt. Acta, **26** (11), 1427-1441 (1979).

[Bryngdahl 1969] O. Bryngdahl and al., “Longitudinally reversed shearing interferometry, ” J. Opt. Soc. Am., **59**, 142-146 (1969).

[Cathro 1981] K.J. Cathro, D.C. Constable, T. Solaga, , “Durability of porous silica antireflection coatings for solar collector cover plates,” Solar Energy, Vol. **27**, No.6, 491- 496 (1981).

[Cathro 1984] K.J. Cathro, D.C. Constable, T. Solaga, “Silica low-reflection coatings for collector covers, by a dip-coating process,” Solar Energy, Vol. **32**, No.5, 573-579 (1984).

[Cescato 1999] L. Cescato, and al., “Noise reduction in the recording of holographic masks in photoresist,” SPIE, Vol.**3879**, 214-222 (1999).

[Chamberlain 1979] John Chamberlain, “The principle of Interferometric Spectroscopy,” John Wiley&Sons, New-York (1979).

[Chen 1988] H. Chen, R. Hershey, and E. Leith, “Sawtooth profile fringes with a two-grating interferometer,” Appl. Opt., **27**, 1193- (1988).

[Chen 1996] X. Chen, S. H. Zaidi, S. R. J. Brueck and D. J. Devine, “Interferometric Lithography of Sub-Micrometer Sparse Hole Arrays for Field-Emission Display Applications,” Jour. Vac. Sci. Technol., B**14**, 3339-3349 (1996).

[Choi 1997] J.H. Choi et al., “Fabrication and characterisation of field-emitter arrays using TIR lithography,” SID International Symposium, Digest of Technical Papers, Vol. **28** (1997).

[Clube 1997] F. Clube et al., “Large-field, high-resolution photolithography,“ SPIE, Vol. **3099**, pp.36-45 (1997).

[Cowan 1984] J.J. Cowan, “The Recording and Large Scale Replication of Crossed Holographic Grating Arrays Using Multiple Beam Interferometry,“ Proc. SPIE, Vol. **503**, 120-129 (1984).

[Däschner 1996] W. Däschner, C. Wu, S.H. Lee, “General aspheric refractive micro-optics fabricated by optical lithography using a high energy beam sensitive glass gray-level mask,” J. Vac. Sci. Tech., B **14**, 135-138 (1996).

[Diel 1984] J. C. Diel, I. C. McMichael, H. V. Vanherzeele, “Degenetrate Four-Wave Mixing of Picosecond Pulses in the Saturable Amplification of a Dye Laser,” IEEE J. Quantum. Electron.**QE-20**, 630-636 (1984).

[Dill 1975] F. H. Dill, et al., “Characterization of Positive Resists,“ IEEE Trans. Electron Devices, Vol. ED-**22**, No. 7, 445-452 (1975).

[Dill 1977] F. H. Dill, J. M. Shaw, “Thermal Effects on the Photoresist AZ1350J,” IBM Jour. Res. Dev., Vol. **21**(3), 210-218 (1977).

[Ehbets 1995] P. Ehbets, H. P. Herzig, P. Nussbaum, P. Blattner, R. Dändliker, “Interferometric fabrication of modulated submicrometer gratings in photoresist,“ Appl. Opt., **34**, 2540-2547 (1995).

[Eisenberg 2005] N. P. Eisenberg, M. Manevich, A. Arsh, M. Klebanov , V. Lyubin, “MICRO-PRISM ARRAYS FOR INFRA-RED LIGHT BASED ON AS2S3-AS2SE3 PHOTORESISTS,” Chalcogenide Letters, Vol. **2**, (4), 35-37 (2005).

[Eismann 1989] M. T. Eismann, A. M. Tai, J. N. Cederquist, “Iterative design of a holographic beamformer,” Appl. Opt., **28**, 2641-2650 (1989).

[Ekberg 1994] M. Ekberg, F. Nikolajeff, M. Larsson, and S. Hård, “Proximity compensated blazed transmission grating manufacture with direct-writing, electron-beam lithography,” Appl. Opt., **33,** 103-107 (1994).

[Fernandez 1996] A. Fernandez, P. J. Bedrossian, S. L. Baker, S. P. Vernon, D. R. Kania, ”Magnetic force microscopy of single-domain cobalt dots patterned using interference lithography**,”** IEEE Trans. Magnetics, Vol. **32**(5), 4472-4474 (1996).

[Fleming 1997] M.B. Fleming and M.C. Hutley, “Blazed diffractive optics,” Appl. Opt., **36** (20), 4635-4643 (1997).

[Freijlich 1988] J. Freijlich and al., “Analysis of an active stabilization system for an holographic setup,” Appl. Optics., **27**, ff :1967 (1988).

[Freschi 2002] A.A. Freschi, F.J. dos Santos, E.L. Rigon and L. Cescato, “Phase-locking of superimposed diffractive gratings in photoresists,” Optics Communication, **208**, 41-49 (2002).

[Gale 1994] M. T. Gale, M. Rossi, J. Pedersen, and H. Schütz, “Fabrication of continuous-relief micro-optical elements by direct laser writing in photoresist,” Opt. Eng., **33,** 3556–3566 (1994).

[Gale 1997] M.T. Gale, “Replication,” Chapter 6 in Micro-Optics: Elements, Systems and Applications, H.P. Herzig, Ed., Taylor and Francis, London (1997).

[Gale 1998] M. T. Gale, “Zero-order grating microstructures,” Optical Document Security, R. L. van Renesse, ed., Artech House, London, 1998, Chapter 12.

[Gerchberg 1972] R. W. Gerchberg, W. O. Saxton, “A practical algorithm for the determination of phase from image and diffraction plane pictures,” Optik, **35**, 227-246 (1972).

[Gimkiewicz 1999] Ch. Gimkiewicz, D. Hagedorn, J. Jahns, E.-B. Kley, F. Thoma, “Fabrication of microprisms for planar optical interconnections by use of analog gray-scale lithography with high energy beam sensitive glass,” Appl. Optics, **38**, 2986-2990 (1999).

[Goodman 1996] J. W. Goodman, “ Introduction to Fourier Optics,” McGraw-Hill, 2nd Ed., 1996.

[Herzig 1990] H. P. Herzig, D. Prongué and R. Dändliker, “Design and fabrication of highly efficient fan-out element,” Jpn. J. Appl. Phys., **27**, L1307-L1309 (1990).

[Herzig 2001] H. P. Herzig, C. Weiteneder, A. Schilling, “Multiple beam recording of diffractive microstructures,” Univ. de Neuchâtel (Switzerland) [4440-27]

[Hobbs 1999] D. Hobbs and al., “Automated Interference Lithography Systems for Generation of Sub-Micron Feature Size Patterns,” SPIE, Vol. **3879**, 124-135 (1999).

[Huang 1989] J.-P. Huang, T. K. Kwei, A. Reiser, “On the Molecular Mechanism of Positive Novolac Resists,” Proc. Of the Soc. of Photoopt. Instrumen. Eng., Vol. **1086**, 74-84 (1989).

[Ichikawa 2004] H. Ichikawa, “Numerical analysis of microretroreflectors: transition from reflection to diffraction,” J. Opt. A, **6**, 121-127 (2004).

[Iemmi 1986] C.C. Iemmi, J.M. Simon and J.O. Ratto, ”Synthesis of asymetric profiles from a double grating interferometer,” Appl. Opt., **25** (16), 3171-3178 (1986).

[Isotalo 2004] P. Isotalo, D. Bednarowski, T. Nowak, “Reactive molding process modelling: structural analysis of thermoset insulated electrical components,” International Journal of Materials and Product Technology, Vol. **20**, No. 4, 239-253 (2004).

[Johansson 1976] S. Johansson, L.-E. Nilson, K. Bidermann and K. Leveby, “Holographic diffraction gratings with asymmetrical groove profiles,” in Applications of Holography and optical data processing, E. Marom, A.A. Friesem, and E. Wiener-Avnear (Ed.), Pergamon press, NY, 1976.

[Johnson 1984] D. W. Johnson, “Thermolysis of Positive Photoresists,” Adv. Resist Tech., SPIE, Vol. **469**, 72-79 (1984).

[Kirk 1992] A. G. Kirk, T. J. Hall, “Design of binary computer generated holograms by simulated annealing: coding density and reconstruction error,” Opt. Comm., **94**, 491-496 (1992).

[Kirkpatrick 1983] S. Kirkpatrick, C. D. Gelatt, M. P. Vechi Jr., “Optimization by simulated annealing,” Science, **220**, 671-680 (1983).

[Koyler 1979] J. M. Koyler, et al., “Thermal Properties of Positive Photoresist and their Relationship to VLSI Processing,” Kodak Microelectronics Seminar interface ’79, 150-165 (1979).

[Leith 1984] E. Leith, G. J. Swanson, S. Leon, “Construction of Diffractive Optical Elements in non-Coherent Light,” Proc. Soc. Photo-Opt. Instrum. Eng., **503**, ff :2 (1984).

[Leith 1985] E. Leith, R. Hershey, “Transfer Function and Spatial Filtering in Grating Interferometers,” Appl. Opt., **24**, ff :237 (1985).

[Mack 1987] C. A. Mack, “Development of Positive Photoresist,” Jour. Electrochemical Soc., Vol. **134**, No.1, 148-152 (1987).

[Mack 1992] C. A. Mack, “New Kinetic Model for Resist Dissolution,” Jour. Electrochemical Soc., Vol. **139**, No.4, L35-L37 (1992).

[Mait 1990] J. N. Mait, “Design of binary-phase and multiphase Fourier gratings for array generation,” J. Opt. Soc. Am. A, **7**, 1514-1528 (1990).

[Mashev 1981] L. Mashev and S. Tonchev, “Formation of holographic diffraction gratings in photoresist,” Appl. Phys. A: Solids Surf., Vol. A**26**, no.3, 143-149 (1981).

[Mello 1995] B. de A. Mello, I. da Costa, L. Cescato, and C. Lima, “Developed profile of holographically exposed photoresist gratings,” Appl. Opt., **34**, 597-604 (1995).

[Moharam 1984] M. G. Moharam, T. K. Gaylord, G. T. Sincerbox, H. Werlich, B. Yung, “Diffraction characteristics of photoresist surface-relief gratings,“ Appl. Opt., **23**, 3214-3220 (1984).

[Moser 1996] J.-F. Moser, R. Staub and W. R. Tompkin, “Perceptual information from OVD diffraction security devices,” Proc. SPIE, Vol. **2659**, 53-58 (1996).

[Moser 1998] J.-F. Moser, “Document protection by optically variable graphics (Kinegram) ,” Optical Document Security, R. L. van Renesse, ed., Artech House, London, 1998, Chapter 11.

[Naramsimham 1977] M. A. Naramsimham, J. B. Loundsbury, “Dissolution Characterization of Some Positive Resist Systems,” SPIE, Vol. **100**, 57-64 (1997).

[Nassenstein 1969] H. Nassenstein, “Interference, diffraction and holography with surface waves (‘Subwaves’),” Optik Part I, **29,** 597-608 (1969).

[Nishijima 1964] Y. Nishijima, G. Oster, “Moiré Patterns: Their Application to Refractive Index and Refractive Index Gradient Measurements,” J. Opt. Soc. Am., Vol. **54**, No. 1, 1-5 (1964).

[Noponen 1992] E. Noponen, A. Vasara, J. Turunen, J. M. Miller, and M. R. Taghizadeh, “Synthetic diffractive optics in the resonance domain,” J. Opt. Soc. Am. A, Vol. **9**, No. 7, 1206-1213 (1992).

[O’Shea 1995] D. C. O’Shea and W. S. Rockward, “Gray-scale masks for diffractive-optics fabrication: II. Spatially filtered halftone screens,” Appl. Opt., **34**, 7518-7526 (1995).

[Oster 1964] G. Oster, M. Waseerman, , C. Zwerling, “Theoretical Interpretation of Moiré Patterns,” J. .Opt. Soc. Am., Vol. **54** No. 2, 169-175 (1964).

[Prongué 1992] D. Prongué, H.-P. Herzig, R. Dändliker, M. T. Gale, “Optimized kinoform structures for highly efficient fan-out elements,” Appl. Opt., **31**, 5706-5711 (1992).

[Ross 1999] C. A. Ross, and al., “Fabrication of patterned media for high density magnetic storage,” J. Vac. Sci. Technol. B, **17**(6), 3168-3176 (1999).

[Sainov 1999] S. Sainov, R. Stoycheva-Topalova, “Total internal reflection holographic recording in very thin films,” Pure Appl. Opt., **2**, 117-120 (2000).

[Shaw 1977] J. M. Shaw, M. A. Frisch, F. H. Dill, “Thermal Analysis of Positive Photoresist Films by Mass Spectrometry,” IBM Jour. Res. Dev., Vol. **21**, 219-226 (1977).

[Sheridon 1968] N. K. Sheridon, “Production of blazed holograms,” Appl. Phys. Lett., **12**, 316-318 (1968).

[Sinzinger 2003] S. Sinzinger, J. Jahns, “Microoptics,” Wiley, 2nd Ed., 2003, chapter 5.

[Spallas 1995] J. P. Spallas, A. M. Hawryluk, and D. R. Kania, “Field emitter array mask patterning using laser interference lithography,” J. Vac. Sci. Techol. B, Vol. **13**, 1973-1978 (1995).

[Staub 1996] R. Staub, W. R. Tompkin and J.-F. Moser, “Combination Gratings,” Proc. SPIE, Vol. **2063**, 292-299 (1996).

[Staub 1998] R. Staub and W. R. Tompkin, “Non-standard diffraction structures for OVD’s,” Proc. SPIE, Vol. **3314**, 194-202 (1998).

[Staub 1999] R. Staub, W. R. Tompkin and A. Schilling, “Gratings of constantly varying depth for visual security purposes,” Opt. Eng., **38**, 89-98 (1999).

[Staub 2000] Rene Staub, Wayne R. Tompkin, “Self-referencing diffractive features for OVDs,” Proc. SPIE, Vol. 3973, 216-223 (2000).

[Stetson 1967] K. A. Stetson, “HOLOGRAPHY WITH TOTAL INTERNALLY REFLECTED LIGHT,” Appl. Phys. Lett., **11**, ff :225 (1967).

[Swanson 1989] G.J. Swanson, “Binary optics technology: The theory and design of multi-level diffractive optic elements,” Lab. Tech. Rep. 854, DTIC\#AD-213404, Technical report, MIT Lincoln Laboratory, Lexington, Mass. (1989).

[Tomita 1979] A. Tomita, “Phase conjugation using gain saturation of a Nd:YAG laser,” Appl. Phys. Lett., **34**, 463-464 (1979).

[Tompkin 1999] W. R. Tompkin, R. Staub, A. Schilling, and H-P Herzig, “Diffraction from metallic gratings with locally varying profile forms,” Opt. Lett., **24**, 71-73 (1999).

[Tsang 1974] W. T. Tsang, S. Wang, “Simultaneous exposure and development technique for making gratings in positive photoresist,” Appl. Phys. Lett., **24**, 196-199 (1974).

[Tsang 1977] W. T. Tsang, “Theoretical modeling of the simultaneous exposure and development (SED) process of a positive photoresist,” Appl. Opt., **16**, 1918-1931 (1977).

[Turunen 1990] J. Turunen, J. Fagerholm, A. Vasara, M. R. Taghizadeh, “Detour-phasekinoform interconnects: the concept and fabrication considerations,” J. Opt. Soc. Am. A, **7**, 1202-1208 (1990).

[Vasara 1991] A. Vasara, and al., “Rigorous diffraction analysis of Damman gratings,” Opt. Commun., **81**, 337-342 (1991).

[Vasara 1992] A. Vasara, M. R. Taghizadeh, J. Turunen, J. Westerholm, E. Noponen, H. Ichikawa, J. M. Miller, T. Jaakkola, and S. Kuisma, “Binary surface-relief gratings for array illumination in digital optics,” Appl. Opt., **31**, 3320-3336 (1992).

[Veldkamp 1983] W. B. Veldkamp, G.J. Swanson, “Developments in fabrication of binary optical elements,” Proc. SPIE, **437**, 54ff (1983).

[Watts 1997a] R. A. Watts and J. R. Sambles, “Polarisation conversion from blazed diffraction gratings,” Journal of Modern Optics, **44**, 1231-1241 (1997).

[Watts 1997b] R. A. Watts and J. R. Sambles, “Reflection gratings as polarisation convertors,” Optics Commun. , **140**, 179-183 (1997).

[Weaver 1997] J.H. Weaver and H.P.R. Frederikse, “Optical Properties of Metals and Semiconductors,” CRC Handbook of Chemistry and Physics, 74th Edition and subsequent printings (CRC Press, Boca Raton, Florida), 12-109 – 12-131 (1997).

[Wittig 2003] Wittig L.-C., T. Clausnitzer, E.-B. Kley, “Alternative method of gray tone lithography with potential for the fabrication combined continuous 3D surface profile and subwavelength structures,” SPIE, Vol. 5183, San Diego 2003.

[Wood 1910] R. W. Wood, “The echelette grating for the infra-red,” Philos. Mag., **20,** 770-778 (1910).

[Wyrowski 1990] F. Wyrowski, “Diffractive optical elements: iterative calculation of quantized blazed phase structures,” J. Opt. Soc. Am. A, **7**, 961-969 (1990).

[Yule 1967] J. A. C. Yule, “Principles of Color Reproduction,” Wiley, Chap. 13 (1967).

[Yu 2004] X. J. Yu and H. S. Kwok, SID04 Digest, Vol. **35**, 875-877 (2004).

[Zanke 1998] Ch. Zanke, A. Gombert, A. Erdmann, M. Weiss, “Fine-tuned profile simulation of holographically exposed photoresist gratings,” Opt. Comm., **154**, 109-118 (1998).